Microdroplet Impact onto Topographies of Commensurate Size

Khaled H. A. Al–Ghaithi

Submitted in accordance with the requirements for the degree of

Doctor of Philosophy

University of Leeds

EPSRC Centre for Doctoral Training in Fluid Dynamics

MARCH, 2021

Declaration

The candidate confirms that the work submitted is his own, except where work which has formed part of jointly authored publications has been included. The contribution of the candidate and the other authors to this work has been explicitly indicated below. The candidate confirms that appropriate credit has been given within the thesis where reference has been made to the work of others.

Chapters 4, 5 and 6 contain material from the following jointly authored publication: **Al–Ghaithi, K.H.A.**, Harlen, O.G., Kapur, N. & Wilson, M.C.T. Morphologies and dynamics of micro-droplet impact onto an idealised scratch. *Journal of Fluid Mechanics*. Accepted 13.07.21

The candidate developed the computational code and GPU implementation required for this work and conducted all the simulations and analysis of the results. He drafted and edited the paper. The co–authors are the PhD supervisors who provided guidance throughout the work and comments on the drafts.

To

Ghaliyah & Hamood Al-Ghaithi

Acknowledgements

I would like to thank Dr Mark CT Wilson, the lead supervisor in my PhD, for his continued support and being there especially in the most stressful of times. I would also like to thank Dr Oliver G Harlen for his continued support, insight and interesting discussion as well as Nik Kapur for his support with lab–related work.

I am also grateful to Andrew Bates and Dr Kieran Looney from Dupont Teijin Films (DTF) for their discussions and insight. I am also grateful to the Engineering and Physical Sciences Research Council (EPSRC) Centre for Doctoral Training in Fluid Dynamics, particularly Claire Savy, Peter Jimack, Emily Bryan–Kinns and my colleagues.

I am most grateful to my parents without whose support and sacrifice I could not have made it this far. I want to thank my brothers, sisters and grandmother for always being there for me in every way they could. My friends deserve my utmost gratitude for making my time enjoyable and the hardest times sufferable, I want to particularly thank Mohammed Hamed, Shadwa Hashish, Karrar AlDirawi, Foteini Zagklavara, Hafiz Salae, Aziz Alnori, and Ahmed AlSuleihi.

Abstract

As inkjet technology develops to produce smaller droplets, substrate features such as accidental scratches or manufacturing defects can potentially affect the outcome of printing, particularly for printed electronics where continuous tracks are required. Here, the deposition of micro–droplets onto an idealised scratch of commensurate size is studied using a GPU–accelerated 3D multiphase lattice Boltzmann model validated against published experiments and theoretical models. The scratch is considered as a groove of rectangular cross–section, with rectangular side ridges representing material displaced from the substrate, and seven equilibrium morphologies are identified as a result of inertial spreading, contact line pinning, imbibition into the scratch and capillary flow. A regime map is constructed in terms of scratch depth and width, and theoretical estimates of the regime boundaries are developed by adapting droplet spreading laws for flat surfaces to account for liquid entering the scratches. Good agreement with the numerical results is seen, and the influences of Reynolds number, Weber number and advancing and receding contact angles are explored. Negative and positive implications of the results for printing applications are discussed and illustrated via multiple–droplet simulations of printing across and along scratches.

Contents

List of Figures

List of Tables

Chapter 1 | Introduction

Contents

1.1 Printed Electronics

Printed electronics, also known as organic electronics (Chang et al., 1965), is a technology whereby electronics manufacturing and text/graphics printing techniques are combined to produce electronic products that are thin, flexible, wearable, light, cost–effective and environmentally friendly (Suganuma, 2014). Enabling this merger is the ability to deposit materials from solution (Lupo et al., 2013). This technology is increasingly exploited in numerous industries including lighting, organic/inorganic photovoltaics, displays, integrated smart systems and electronic components (Suganuma, 2014). The flexible, printed and organic electronics market size in 2020 was $41 billion and is estimated to grow to $73 billion by 2030 (Das et al., 2019). Printing methods used in printed electronics include offset, gravure, flexo, and screen printing (Lupo et al., 2013; Suganuma, 2014). Presently these are used in sheet–fed, low throughput, and batch processes; the desire to move to roll–to–roll, high throughput and continuous processes is driving the development of alternative printing technologies, particularly *inkjet printing*.

1.1.1 Inkjet Printing

Traditional printing methods, such as lithography, flexography, gravure and screen printing, have experienced consistent improvement for a couple of centuries and can now produce high quality and precision printed products over large areas (Huchings et al., 2016). These methods require liquid to transfer through direct contact with the substrate, a previously prepared master containing the pattern to be printed. To change the printed product, the process has to stop and the master pattern has to be physically changed (Huchings et al., 2016). On the other hand, inkjet printers, now ubiquitous in homes, offices and increasingly in manufacturing processes, use a non–contact droplet deposition mechanism. Patterns are made by precisely producing and placing small $(10 - 100)\mu$m liquid droplets on a substrate (Stringer

and Derby, 2012). Unlike conventional printing methods, a master pattern is not needed; patterns are defined digitally, stored electronically and can easily be changed (Huchings et al., 2016) so that each printed pattern can equally easily be different or the same as its immediate neighbours in a sequence (Hutchings and Martin, 2012).

There are two main methods to produce inkjet droplets: continuous inkjet (CIJ) and drop on demand (DOD). The former, as the name suggests, produces a continuous stream of droplets through the continuous breakup of a liquid jet of ink; the desired droplets for printing are selected electrostatically and the rest are recycled. CIJ was developed in the 1970s and 1980s for applications that require high speed and low printing resolution such as marking products, bar codes and addressing bulk mail (Hutchings and Martin, 2012). Drop on Demand, as the name also implies, produces a droplet only at the desired time and location. In DOD, a pressure pulse, conventionally produced by a piezoelectric element in the printhead, ejects a small volume of liquid at speed. DOD has been developing since the mid–1980s and is capable of much higher resolutions than those from CIJ, but at lower printing speeds, enabling the printing of text and images in the domestic and office environments (Hutchings and Martin, 2012). Typical droplet speeds are $5 - 8\,\mathrm{m\,s^{-1}}$ and $10 - 30\,\mathrm{m\,s^{-1}}$ for DOD and CIJ respectively, and typical inkjet droplet sizes are $(10 - 100)\,\mu\mathrm{m}$ in both methods. Newer methods can exceed these typical ranges; for example, electrohydrodynamic (EHD) inkjet printing which uses an electric field instead of a piezoelectric to produce droplets in DOD can produce relatively smaller droplets ($< 5\,\mu\mathrm{m}$) (Zheng et al., 2021), and another example is laser–induced droplets which can reach speeds of $50\,\mathrm{m\,s^{-1}}$ (Visser et al., 2012).

Inkjet printing has been increasingly adopted for manufacturing applications due to the following features:

1. Inkjet printing is a digital process that overcomes the need for a physical mask/frame as in conventional contact printing methods and gives great flexibility for changing the printed patterns on demand.

2. It is suitable for short print runs with high–profit margins and as reliability increases, inkjet printing will compete with traditional methods in large–area manufacturing in terms of cost–efficiency (Huchings et al., 2016).

3. The process is non–contact. This makes it ideal for flexible substrates (expected to be the majority for mass production and will eventually be applied in roll–to–roll (R2R) manufacturing processes (Suganuma, 2014)) fragile substrates, liquid baths, and powder beds.

4. The process is material–efficient, saving material wasted in conventional printing methods due to the need for masks/frames.

5. A wide range of materials can be inkjet printed, materials can be combined and printed, and inkjet can be combined with other processing steps. Metals, ceramics, polymers, living cells and tissue have been inkjet printed.

6. Inkjet printing works at speed and can work in parallel with different inkjet heads working on various areas of the product simultaneously. Multiple heads can be assembled and arranged in different ways. This makes inkjet suitable as an R2R process which is more time, cost and material efficient than conventional methods that work as sheet-fed processes.

Fluid properties of inks are restricted to a fairly narrow range of viscosities in inkjet printing. Typical viscosities are $\mu < 20$ mPa s, which limits the particle loading in these inks. Particle sizes need careful control to avoid blockages, which makes inks expensive to manufacture.

1.1.2 Substrates for Inkjet Printing of Electronics

Substrates for printed electronics have particular requirements including flexibility, excellent transparency, *surface smoothness*, thinness, lightness and more (Suganuma,

2014). Commonly used substrates include polyethylene terephthalate (PET), polyethylene naphthalate (PEN), polyimide (PI), glass, paper, transparent paper and steel. Glass substrates are commonly used in optical products such as displays, photovoltaics, and lighting due to their high transparency and low haze. Glass is, however, brittle, dense and expensive compared with plastic substrates. PET is the more popular of plastic substrates due to its relatively low cost and high transparency, but it has low heat resistance hence mandates the entire printing process occur at low temperatures. PEN and PI have better heat resistance but smaller transparency and higher cost. Refer to Suganuma (2014) for more details on substrates.

Besides challenges related to substrate characteristics such as transparency, heat resistance, cost and rigidity, small imperfections in the substrate surface can affect the printing quality. These arise through small variations during manufacturing or as a result of unintended damage, such as scratching during transportation and/or handling of the substrate, especially in plastic substrates. These can pose a challenge for printing continuous tracks to form electrical circuits (Chilton, 2012), particularly as the droplet sizes are progressively decreasing in the quest for higher resolution. Topographical features, of commensurate size to substrate defects, can also be added to substrates to control the flow of the droplets as in (Seemann et al., 2005; Kant et al., 2017). The focus of this thesis is to study the interaction of single and multiple droplets with surface defects/features of commensurate size to inkjet printing droplets across the relevant printing parameter space.

1.2 Project Aims and Objectives

The aims of the project can be summarised in two main points:

- To understand the effect of the surface defects on printing by studying droplet–

surface interactions.

- To conduct a parametric study of the variables that affect the spreading of droplets on surfaces and establish operability diagrams that can be used to inform the film production and subsequent printing processes.

To achieve the aims of the project, the following objectives must be achieved:

1. Develop a reliable simulation tool for real surfaces and fluids. This includes choosing the right multiphase models with the right extensions to control surface tension as a parameter and reach sufficiently high–density ratios (greater than 500) while keeping the simulation stable. This also requires capturing surface topographies in the simulations with various contact angles.
2. Validate the model against experiments in the literature.
3. Simulate single droplet printing onto an idealised 2D scratch and characterise the possible resulting morphologies and how they vary within the printing parameter space.
4. Simulate printing lines of droplets onto these 2D scratch–like features to assess the potential influence of these features on inkjet–printed electronics.

1.3 Thesis Overview

The previous works in the literature on single and multiple micro–droplet impact on a flat substrate and printing on substrate surfaces with topographies are presented in chapter 2. The chapter also presents the main methods to simulate such a system and concludes with choosing the lattice Boltzmann (LBM) method for the thesis.

Chapter 3 then presents the LBM method, overviews the multiphase derivatives of the method, and presents the pseudo–potential model chosen for this thesis.

In its original form, however, the pseudo–potential approach cannot replicate inkjet printing conditions, particularly in terms of density ratio between phases and surface tension.

Chapter 4 then investigates the various methods to mitigate the issues of the pseudo–potential model and chooses appropriate modifications from the literature to improve the model. The approach is then validated and its implementation accelerated using GPUs.

Having developed an appropriate approach and validated it, chapter 5 simulates the impact of a single droplet impacting a substrate surface with an idealised scratch topography. The resulting morphologies are named and analytical models to expect when they will occur are developed. The effects of fluid, flow and substrate on the formation of the morphologies are also investigated. The implications of the identified morphologies for printing applications of lines are discussed in chapter 6. The thesis is finally concluded in chapter 7.

Chapter 2 | Literature Review

Contents

2.1 Droplet Impact onto a Flat Surface

2.1.1 Single Droplet Impact

A significant amount of experimental, computational, and theoretical work has focused on the impact of single and multiple droplets onto smooth or nominally flat rough substrates. This makes these parts of the problem relatively well studied; for reviews on the topic refer to Yarin (2006), Josserand and Thoroddsen (2016), and Khojasteh et al. (2016). When a droplet impacts a dry surface it will spread and stick, rebound or splash depending on the fluid and surface properties as well as the droplet speed.

The dynamics of a droplet that spreads and sticks on a solid smooth surface can be classified into three stages. In the first stage, the droplet spreads due to inertia on an air layer which prevents direct contact with the substrate. This air layer is either expelled or trapped in the droplet as a bubble when the droplet eventually makes contact with the substrate. In the second stage, surface tension causes the droplet to oscillate or relax depending on the degree of viscous dissipation. In the final stage, the droplet spreads under capillary forces reaching an equilibrium that minimises free energy. The three stages were labelled by Rioboo et al. (2002) as kinematic and spreading, relaxation, and wetting/equilibrium respectively.

Droplet impact conditions are typically described in terms of the Reynolds number and Weber number, defined respectively as

$$Re = \frac{uD_0}{\nu} \quad \text{and} \quad We = \frac{\rho u^2 D_0}{\gamma}, \tag{2.1}$$

where u is the impact velocity, D_0 is the in–flight droplet diameter, ν is the kinematic viscosity, ρ the density, and γ the surface tension. To set the current work in context, figure 2.1 presents a Re–We map of key previous studies of droplet impact onto solid

surfaces compiled by the author from studies in the literature. By necessity, inkjet printing systems operate under non–splashing conditions and the typical range of Re and We is indicated by the dashed rectangle. Interestingly, micro–droplets (i.e. droplets with diameter below about 100 µm) have been shown not to splash, even at conditions well above the splashing threshold (Visser et al., 2012). Hence, micro–droplets do not necessarily behave in the same way as much larger droplets despite dynamic similitude. The classic splashing threshold found in (Josserand and Thoroddsen, 2016) is also plotted in figure 2.1. Micro–droplet studies are indicated by red–filled symbols in figure 2.1. There are many studies of droplet spreading, resulting in a wide collection of models for important characteristics such as the equilibrium and maximum spreading diameters discussed in the following sections.

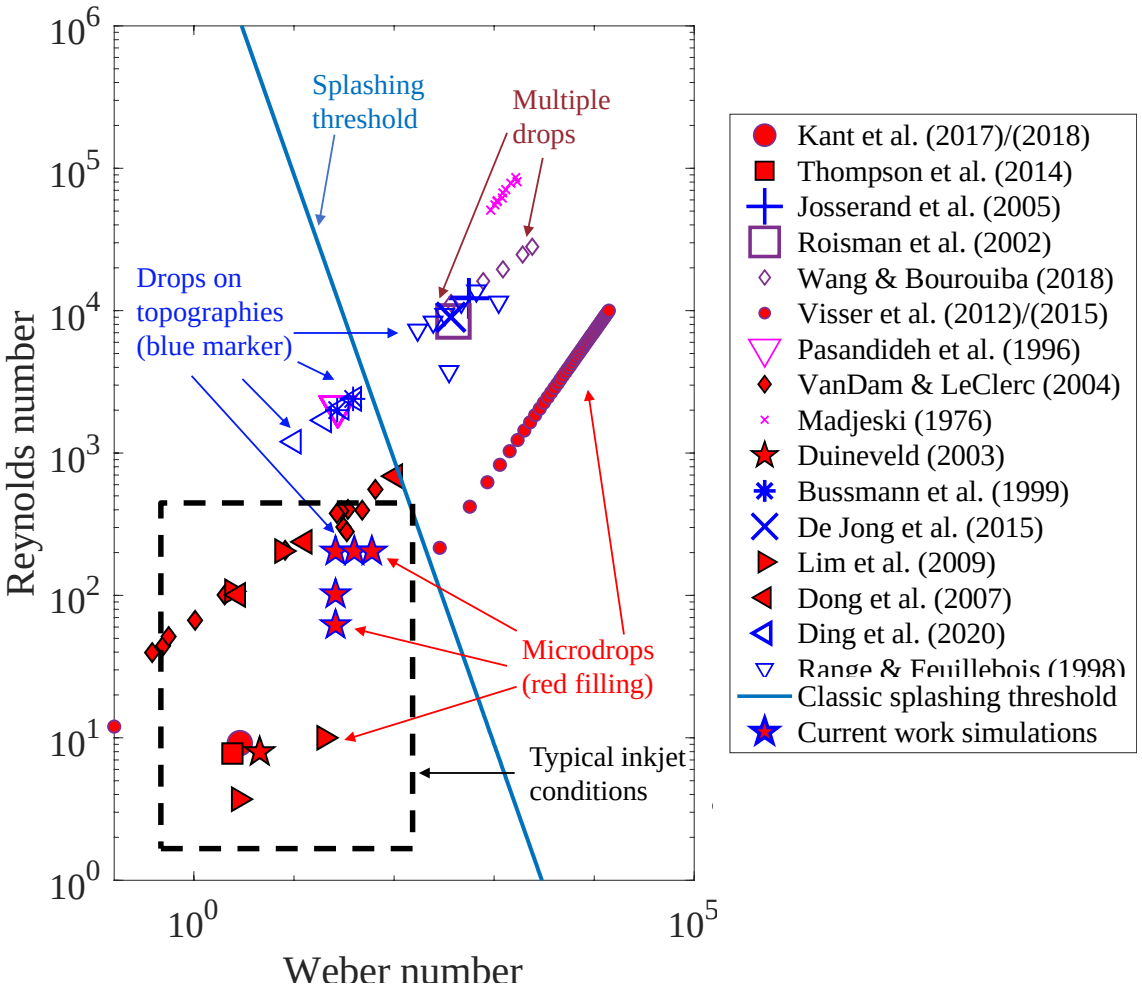

Figure 2.1: A map of previous studies of single and multiple droplet impact onto surfaces with and without topographical features in terms of Reynolds number and Weber number.

2.1.2 Equilibrium Spreading Diameter

The shape of a droplet in equilibrium on an ideal flat substrate (i.e. in the absence of hysteresis and topography) will depend on the contact angle and Bond number Bo (also called Eötvös number) defined as,

$$Bo = \frac{\Delta\rho g D_0}{\gamma}, \tag{2.2}$$

where g is the acceleration due to gravity and $\Delta\rho$ is the density difference between the liquid and the gas. For droplets with $Bo < 1$, which holds for microdroplets, the droplet forms a spherical cap. Knowing the equilibrium contact angle θ_{eq}, we can write an expression for the radius of the spherical cap using conservation of volume (Van Dam and Le Clerc, 2004),

$$\frac{4}{3}\pi R_0^3 = R_{eq}^3 \tan\left(\frac{\theta}{2}\right)\left(3 + \tan^2\frac{\theta}{2}\right);$$

so the equilibrium diameter normalised as $\beta_{eq} = D_{eq}/D_0 = R_{eq}/R_0$, is:

$$\beta_{eq} = 2\left(\tan\frac{\theta}{2}\left(3 + \tan^2\frac{\theta}{2}\right)\right)^{-1/3}. \tag{2.3}$$

Other forms have distinguished between hydrophilic cases where $\theta_{eq} < \pi/2$, and hydrophobic cases, $\theta_{eq} > \pi/2$ (Lee et al., 2016),

$$\beta_{eq} = \begin{cases} \left(\frac{4\sin^3\theta}{2-3\cos\theta+\cos^3\theta}\right)^{1/3} & \text{if } \theta < \pi/2 \\ \left(\frac{1}{(2+\cos\theta)\sin^4(\theta/2)}\right)^{1/3} & \text{if } \theta > \pi/2. \end{cases} \tag{2.4}$$

Equations (2.3) and (2.4) match for $\theta < \pi/2$ and differ only slightly otherwise.

2.1.3 Maximum Spreading Diameter

For a droplet impacting a planar surface, the maximum spreading diameter D_{max} (normalised as $\beta_{max} = D_{max}/D_0$) has been extensively studied and found to depend on the impact velocity and fluid properties captured in the Reynolds and Weber numbers (2.1). Pasandideh-Fard et al. (1996) showed that for low Weber and Reynolds numbers, surface wettability also becomes a significant variable. Clanet et al. (2004) demonstrated that there are two regimes for droplet deposition: one is the capillary regime with low We and high Re, where viscous effects are negligible, and the other is the viscous regime with high We and low Re, where capillary forces are negligible. Early studies reported two conflicting β_{max} scalings with We in the capillary regime: studies that used an energy balance predicted a $We^{1/2}$ dependence (Madejski, 1976; Chandra and Avedisian, 1991; Bennett and Poulikakos, 1993), while those using a momentum balance predicted $We^{1/4}$ (Clanet et al., 2004). In the viscous regime, most studies predict a $Re^{1/5}$ dependence (Madejski, 1976; Chandra and Avedisian, 1991; Bennett and Poulikakos, 1993).

Eggers et al. (2010) showed, using a dynamical model with a viscous boundary layer, that if the $We^{1/2}$ scaling holds, then $\beta_{max} = Re^{1/5}F(P)$, where F is a function of $P = WeRe^{-2/5}$. Laan et al. (2014) showed, using experiments on three liquids with different viscosities, that the $We^{1/2}$ scaling holds rather than $We^{1/4}$ and used Padé interpolation to approximate $F(P)$ for $We > 10$. Lee et al. (2016) extended this to $We > 1$ by incorporating surface wettability by incorporating the β_{eq} from equation (2.4). Table 2.1 lists a selection of models from the literature. In fact, some models developed earlier than (Eggers et al., 2010), can be written in the form $\beta_{max} = Re^{1/5}F(P)$. For example, Wang and Bourouiba (2018) rewrote the model by Scheller and Bousfield (1995) in table 2.1 using $F(P) = 0.61P^{1/6}$, so

$$\beta_{max} = 0.61Re^{1/5}P^{1/6}. \tag{2.5}$$

We can similarly rewrite the model by Roisman (2009) in table 2.1 using $F(P) = 0.87 - 0.4P^{-1/2}$ so,

$$\beta_{max} = 0.87 - 0.4P^{-1/2}. \tag{2.6}$$

Wildeman et al. (2016) recently used extensive simulations and modelling to bridge the energy balance and the momentum balance approaches and developed a model for β_{max}. All these models have good agreement with experimental and numerical data (Josserand and Thoroddsen, 2016; Lee et al., 2016; Wildeman et al., 2016). It is challenging to test the applicability of these models to large Re because of the onset of splashing for millimetre droplets before maximum spreading is reached (Josserand and Thoroddsen, 2016) and the difficulty in speeding up microdroplets.

2.1.4 Continuous Bead Printing On Flat Substrates

A series of droplets overlapping on the substrate coalesce and form a continuous bead also called a printed line/track especially after drying. The stability of a printed line is sensitive to droplet spacing, contact angle and contact line pinning. Davis (1980) studied the stability of a liquid bead, using linear stability analysis, under three conditions of the contact–line: (i) is pinned, (ii) moves but with a fixed contact angle, and (iii) movement with a contact angle that behaves as a smooth function of contact–line speed. For cases (ii) and (iii), he found wavenumbers for which the continuous bead is unstable and breaks into several segments. When the contact line is pinned, i.e. case (i), he found the bead to be stable for contact angles $\theta_{eq} < \pi/2$. Schiaffino and Sonin (1997) and Gau et al. (1999) experimentally confirmed the theoretical prediction by Davis (1980).

Duineveld (2003) demonstrated another instability called *the bulging instability*. He showed that when one bulge forms it acts as a seed for subsequent bulges and hypothesised that it forms due to the initial head, also called the primary head. He did not study the formation of the initial bulge, however (Thompson

number	Study	β_{max} $(= D_{max}/D_0)$
1	Chandra and Avedisian (1991)	$\frac{3We}{2Re}\beta_{max}^4 + (1-\cos\theta)\beta_{max}^2 - \left(\frac{We}{3}+4\right) \approx 0$
2	Scheller and Bousfield (1995)	$0.61Re^{1/5}(P)^{1/6}$
3	Pasandideh-Fard et al. (1996)	$\sqrt{\frac{We+12}{3(1-\cos\theta_A)+4(We/\sqrt{Re})}}$
4	Roisman (2009)	$Re^{1/5}(0.87-0.4(WeRe^{-2/5})^{-1/2})$
5	Laan et al. (2014)	$Re^{1/5}\frac{P^{1/2}}{1.24+P^{1/2}}$
6	Lee et al. (2016)	$\sqrt{\frac{We^{1/2}Re^{1/5}}{7.6+We^{1/2}}+\beta_{eq}^2}$
7	Wildeman et al. (2016)	$\frac{3(1-\cos\theta)}{We}\beta_{max}^2 + \frac{0.7}{\sqrt{Re}}\beta_{max}^2\sqrt{\beta_{max}-1} = \frac{12}{We}+\frac{1}{2}$

Table 2.1: A selection of previously published models for predicting the maximum spreading diameter of a droplet impacting on a flat surface. Here $P = WeRe^{-2/5}$ and β_{eq} is the equilibrium spread diameter.

et al., 2014). Thompson et al. (2014) studied the initial bulge more carefully, using a quasi–static model and experiments. They found that the primary head forms because of contact angle hysteresis (CAH). There are three cases to consider in terms of CAH characterised by Thompson et al. (2014) using $\epsilon \equiv \theta_R/\theta_A$: (i) $\epsilon = 1$, (ii) $\epsilon = 0$ and $\theta_R = 0$ and (iii) $0 < \epsilon < 1$.

When $\epsilon = 1$, the only possible morphology is a circular island. When $\epsilon = 0$ and $\theta_R = 0$, the contact line is pinned and forms the non–receding morphology characterised by a long and shallow rivulet as seen in (Duineveld, 2003). Otherwise, when $0 < \epsilon < 1$, θ_R is finite and the contact line is allowed to recede. This allows the retraction of the rivulet towards the primary head; this is known as *the drawback effect*. The accumulation of the drawback effect eventually results in the landing droplet not making contact with the existing fluid. The drawback effect can decrease the resolution of a 3D inkjet printed pattern, reduce dimensional tolerance and cause displacement of solder bumps on printed circuit boards (Dalili et al., 2014). This results in the formation of a new line. Thompson et al. (2014) think that this retraction of the rivulet is what is happening rather than a Rayleigh (1879) type instability breaking a continuous line as claimed in (Duineveld, 2003). Through their models, Thompson et al. (2014) demonstrated that bulging occurs because of competition between the transport of fluid into the pre–existing rivulet and spreading of the new droplet. This bulging instability increases with decreasing spacing — i.e. increasing overlap.

There are two competing trends: decreasing spacing compensates for the drawback effect but also has the effect of inadvertently increasing the bulging instability. A trade–off, therefore, exists between these competing trends. Figure 2.2 shows this trade–off: for low spacing, bulges are bigger and more frequent than for higher spacing lines. For high spacing, liquid islands or individual droplets are formed rather than a line. For moderate spacing, bulges are not formed but a primary head is. Note that figure 2.2 has a spacing $\delta = \dfrac{\Delta x}{D_0} = 0.5$ where Δx is the

difference between two consecutive droplet centres. Dalili et al. (2014) studied the drawback effect and droplet spacing and arrived at a criterion for break up, given by

$$b_c = \frac{2\Delta x}{\Delta x + D_{flat}} \tag{2.7}$$

where Δx is the centre to centre spacing, D_{flat} is the equilibrium spreading diameter when only one droplet is deposited, and b is a drawback index given by,

$$b = \frac{L}{D_{flat} + (m-1)\Delta x} \tag{2.8}$$

where m is the number of droplet and L is the actual length, and b_c is the critical drawback value below which breakup occurs and above which it does not.

In this thesis, we focus on lines with $\epsilon = 0$ and $\theta_R = 0°$ because they are characteristic of the colloidal inks ubiquitous in the printed electronics industry. This means that the drawback effect is not important here, but spacing persists as an important variable. Other factors that affect printed lines include delay time (i.e. printing frequency), substrate temperature, and printing procedure, however, these will not be considered in this thesis. For studies on these refer to Soltman and Subramanian (2008), Soltman (2011), and Kwon et al. (2018). Some authors also studied line features such as minimum and maximum widths as a function of droplet spacing, refer to Yang et al. (2021) for a recent publication on the topic.

Other studies have considered the impact of single and multiple droplets onto substrates with topographies, we discuss these next.

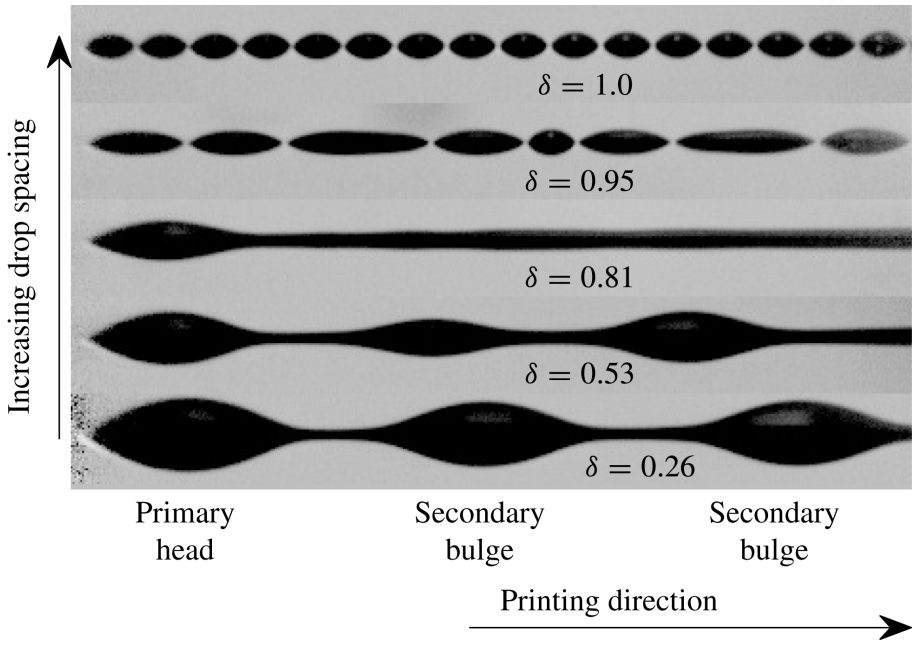

Figure 2.2: Experiments by (Thompson et al., 2014) that looking at the continuity of printed lines with varying the distance between droplets characterised by $\delta = \frac{\Delta s}{D_{flat}}$ where Δs is difference between two droplet centres and R is the radius of a single droplet. The formation of periodic bulges can be seen clearly at $\delta = 0.26$. Picture from (Thompson et al., 2014) **page 262** (Permission not needed for reuse in thesis).

2.2 Impact on Substrates with Topographies

Only a few studies have examined the effect of substrate features on droplet impact. Bussmann et al. (1999) studied the impact of millimetre–sized droplets onto a substrate with a sharp step. They found that a droplet can split due to the presence of a corner. De Jong et al. (2015) studied experimentally the impact of similar–sized droplets near closed pits and open–ended pores and their effect on splashing. Most relevant to this study, since we consider micro–droplets, Rashidian et al. (2019) developed an analytical model and used lattice Boltzmann method (LBM) simulations to investigate how the presence of a small protrusion can cause the rupture of a droplet's spreading lamella and the effect of impact velocity, wettability and protrusion dimensions on this phenomenon. It is found that the presence of a small protrusion can rupture the lamella of the spreading droplet possibly resulting in a non–continuous coating. Kant et al. (2017) studied experimentally the spreading of

a micro–droplet on a substrate with a recessed pixel and found that the presence of its side wall can either enhance or hinder spreading depending on the gradient of the topography ahead. They found that topography can be used to restrict small volumes of liquids to a specific region; a droplet spreading with the topography ahead sloping downhill will be pinned. Jackson et al. (2019) used LBM simulations to explore the effects of misalignment between droplets and small cavities and the filling of the cavities.

Seemann et al. (2005) studied the wetting of micro–structured surfaces using regular grooves separated with ridges. A small liquid volume was deposited using vapour condensation rather than deposition. Two main morphologies were observed, namely an overspilling droplet that extends onto the ridges and neighbouring grooves, and extended filaments that run parallel to the grooves.

Figure 2.3 shows droplet sizes vs feature sizes of studies in the literature compiled by the author. The majority of studies focus on millimetre droplets on millimetre features and millimetre droplets on micron features usually in the context of rough substrates. The study by Seemann et al. (2005) used condensation rather than droplet impact. With the exception of the studies by the Kant et al. (2017) group, literature has not focused on micron droplets on micron features. This is the region of interest for inkjet printing.

As droplet sizes decrease, driven by the desire for higher resolution, it is expected that substrate topographical features will have a greater effect on the printed morphology and product quality. There have been no studies of how such minor variations or defects on a substrate change the morphology of an impacting droplet.

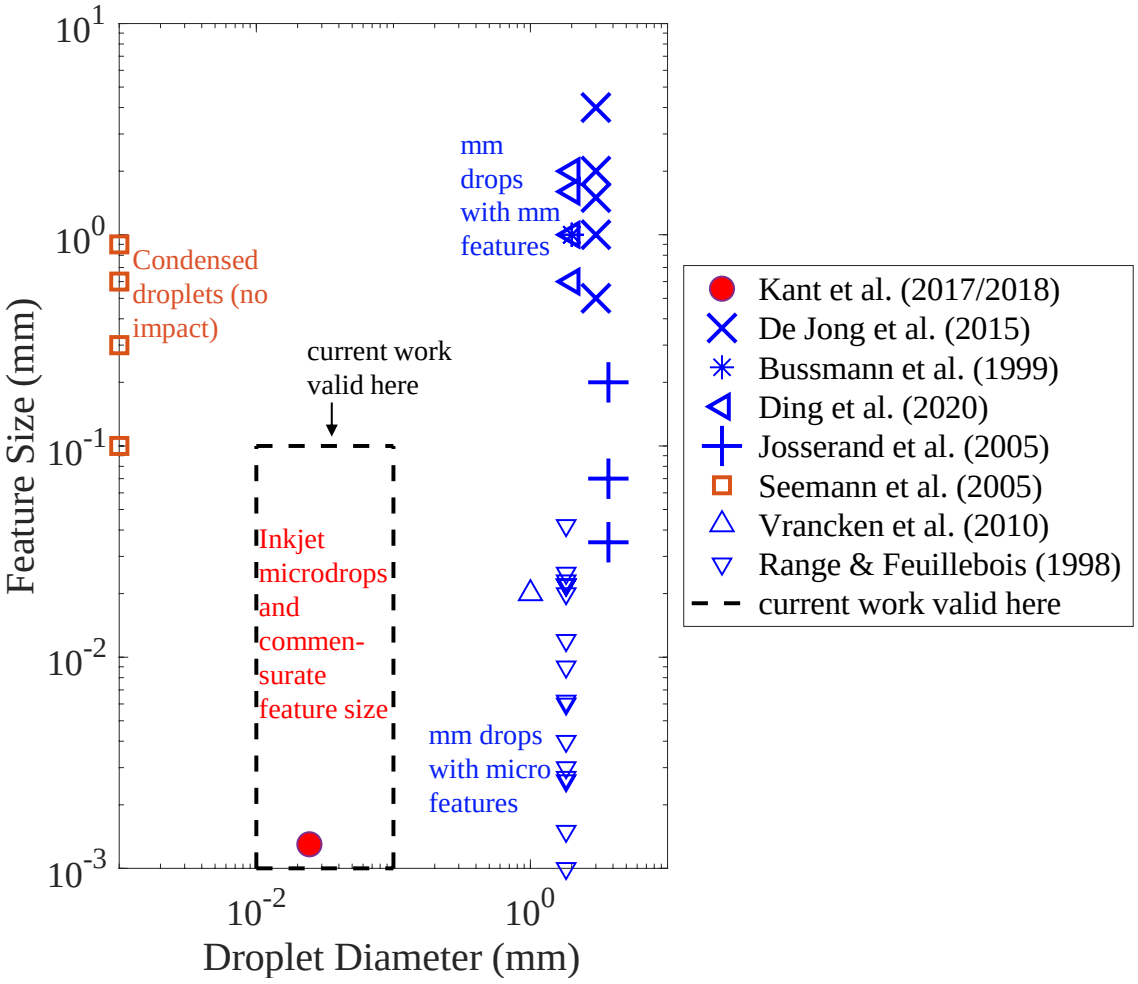

Figure 2.3: Maps of previous studies of single and multiple droplet impact onto surfaces with and without topographical features in terms of droplet diameter and size of feature on the substrate.

2.3 Simulation Methods for Droplets on Surfaces

2.3.1 Multiphase Flows

Droplet impact is a multidimensional process that is particularly challenging to investigate experimentally (Shikhmurzaev, 2007), hence the numerical approach is usually undertaken. Several methods can be used to simulate multiphase (two–phase in our case) flow. There are typically five challenges faced by these methods: conserving mass, momentum and kinetic energy, capturing discontinuities across the interface, dealing with complex topologies and scale separation, issues with robustness for realistic simulations, and capturing surface tension (Mirjalili et al., 2017).

Several possible methods could be used to simulate deforming droplets on surfaces, see e.g. Wilson and Kubiak (2016) for a review. A key requirement of any such method is the ability to represent and determine the shape of the liquid free–surface as it deforms. One possibility is to use an interface tracking approach, where the computational mesh is fitted to and deforms with the free surface — for example as in the finite element technique used by Feng (2015). While this approach provides excellent sharp representations of free surfaces, it cannot track surfaces that break apart or intersect without remeshing, which can lead to instability (Furlani, 2015). This makes the method challenging when simulating systems with critical phenomena such as the breakup or coalescence of small droplets. A more common approach is to use an interface capturing method, of which there are many types, such as the volume-of-fluid (VOF), level-set and phase-field methods — see Mirjalili et al. (2017) for a classification and review. In such methods, the liquid–fluid interface moves through the computational mesh, allowing greater flexibility in terms of severe interface deformations and topological changes in the liquid volume, subject to sufficient mesh resolution.

VOF is used frequently for droplet deposition onto surfaces, with work by Wildeman et al. (2016) being a recent example. However, a key limitation in VOF approaches — and Navier-Stokes based approaches in general — is that the *dynamic* contact angle θ_d usually has to be prescribed as an input. For relatively well–behaved systems, empirical relations between θ_d and the contact line velocity U can be used (Yokoi et al., 2009; Sykes et al., 2020). However, for a complex 3D geometry evolving in time, as considered here, this is not straightforward.

The lattice Boltzmann method (LBM) is increasingly used to simulate the fluid mechanics of multiphase systems. The mesoscopic nature of the method, which retains some molecular–scale physics via probability density distributions, makes it well suited to multiphase simulations, with interface motion, break–up and coalescence readily captured in 3D. Multiphase LBM does not require a relation between θ_d and U, but just the static contact angle θ_s in the case without contact angle hysteresis (CAH), and the advancing θ_A and receding θ_R contact angles in cases with CAH. The dynamic contact angle results naturally from the statistical mechanical nature of the method. LBM is localised and lends itself to parallel computing with GPUs (Krüger et al., 2016); we make use of this feature to run an extensive parametric study here. A disadvantage of LBM is that macroscopic variables such as density, viscosity, velocity, and surface tension are derived quantities, see below. It is also a memory–intensive method, putting limits on domain size when using GPUs, and local grid refinement is still a developing area. These disadvantages did not affect this work.

2.3.2 Lattice Boltzmann Method

Although an alternative to traditional CFD methods, multiphase LBM can be considered an interface–capturing method. In LBM the liquid and ambient fluid are modelled as one fluid with two phases. This method requires the receding and advancing contact angles and the dynamic contact angle arises from the statisti-

cal nature of the method. The advantages and disadvantages of this method are discussed below and the method is discussed in section 3. LBM has the following advantages:

- LBM is algorithmically simple in comparison to other methods such as finite element (Geier and Schönherr, 2017).
- After initialising which involves setting the probability distribution function at every node to the equilibrium distribution function, and choosing ρ and $\boldsymbol{u}$, only two steps are involved; streaming and collision discussed in section 3.2.
- The method is highly localised making it implementable in a highly parallel fashion (Wilson and Kubiak, 2016).
- Using GPUs to run LB simulations is popular and can lead to running speeds hundreds of times faster than CPU's (Wilson and Kubiak, 2016).
- LBM has been extended to model multiphase flow resulting in a diffuse interface representing the liquid–air interface (Shan and Chen, 1993; 1994; Swift et al., 1995; He and Doolen, 2002).
- Surface wettability is incorporated in terms of the static contact angle using a wetting parameter see section 3.5.2.
- LBM can capture contact angle hysteresis (Castrejón-Pita et al., 2011; Castrejón-Pita et al., 2013), also see section 4.7.
- It is well suited to modelling rough surfaces for example work by Khatir et al. (2016) and Yuan and Zhang (2017), porous media for example work by (Spaid and Phelan, 1997) and complex geometries such as work by Succi et al. (1989).
- Simulations including topographical features are fairly straightforward and hence the real surface maps obtained by white light interferometry can be directly imported to the computational and aligned with the lattice nodes (Phelan et al., 1999).

Disadvantages of LBM, however, include:

- Measurable macroscopic variables such as density, viscosity, velocity and surface tensions cannot be directly input into the method as discussed in chapter 3.
- The method is also more memory intensive because statistical variables at every lattice site have to be saved as well as the derived macroscopic variables we are interested in (Guo et al., 2008).
- LBM and especially LBM for multiphase flows is still a developing area. All multiphase models have limitations and improvements are being proposed in the literature.
- Local grid refinement is not yet a fully developed capability in LBM (Di Ilio et al., 2017).
- The governing length scale in our simulations is the smallest length in our physical system. Because local grid refinement is not yet well developed, problems with high aspect ratios can become very big an example is simulations in chapter 5.
- Both the droplet and ambient have to be modelled which makes it necessary to capture more space around the droplet. This makes the spatial dimension bigger than free surface simulations where the ambient is ignored (Wilson and Kubiak, 2016).

2.4 Summary

Several possible methods could be used to simulate droplets on surfaces. These including interface tracking methods (usually using level–set methods e.g. Hu et

al. (2014)) and diffuse interface methods, typically volume of fluid (VOF) and increasingly also the Lattice Boltzmann Method (LBM), e.g. Shan and Chen (1993). Surface tracking methods cannot track surfaces that break apart or intersect without regridding which can lead to instability (Furlani, 2015). This makes the method challenging when simulating systems with critical phenomena such as the breakup or coalescence of small droplets.

Given the advantages of LBM outlined in this chapter, it is adopted in this thesis. In the following two chapters, chapter 3 presents the fundamentals of LBM and the basic implementation of a multiphase LBM model and chapter 4 discusses how this model can be extended to realistic conditions, validated with literature–reported experimental data and accelerated to run on GPUs.

Chapter 3 | Lattice Boltzmann Method (LBM)

Contents

Having concluded the Lattice Boltzmann method (LBM) is suitable for simulating microdroplets impacting substrates with topographies, see section 2.3, we present a review of the method in this chapter. The next chapter presents extensions to the method adopted in this thesis to capture high-density ratios, thermodynamically consistent simulations and wetting.

Originally developed in the 1980s from lattice gas models, LBM has recently seen major developments in the breadth of applications and technical capability (Succi, 2018). In contrast to the continuum simulation methods that seek appropriate solutions to the Navier Stokes equations, the LBM method is derived directly from kinetic theory and statistical mechanics.

3.1 Relevant Scales

To present the origins of the Lattice Boltzmann method, we consider a gas system, in which its constituent molecules/atoms have positions $\boldsymbol{x}$, and velocities $\boldsymbol{\xi}$ at time t. The separation between these particles is assumed to be such that the gas is neither rarefied nor so dense that multiple, particles collisions become frequent. All collisions are assumed two-bodied, and elastic. Before considering the distribution function of the system, we discuss the typical length and time scales relevant to fluid mechanics.

Classical fluid mechanics considers the fluid as a continuum, requiring that the problem's length scale l, i.e. typical scale for gradients in macroscopic properties, is much greater than the size of an atom l_a and mean free path l_{mfp}. This requires the Knudsen number Kn,

$$\mathrm{Kn} = \frac{l}{l_{mfp}} \tag{3.1}$$

to be large, Kn >> 1. In addition to this hierarchy of length scales, there is a corresponding hierarchy of time scales. The shortest timescale is the collision time between two molecules of matter $t_a = l_a/v_t$, where v_t is associated with thermal motion velocity given by $v_t \propto (kT/m)^{1/2}$, where T, k and m are temperature, Boltzmann's constant, and mass of a molecule respectively. Kinetic theory assumes that $t_a \to 0$, i.e. collisions are instantaneous. The time between collisions is called the mean free time t_{mfp} and is defined as $t_{mfp} = l_{mfp}/v_t$. Kinetic theory operates on the time-scale t_{mfp}, which is the time taken to reach local thermodynamic equilibrium through collisions. This local equilibrium does not imply the system is in global thermodynamic equilibrium, a fact that is exploited in the Lattice Boltzmann Method in solving for global dynamics on timescales larger than t_{mfp}.

Depending on whether a fluid flow system is in the *viscous* or *inertial* regime, the next shortest timescale is either the timescale for diffusion $t_{diff} = \rho l^2/\mu$ or the advective timescale $t_{adv} = l/u$. Here ρ and μ are density and dynamic viscosity respectively, and u is the ensemble mean velocity, which, at low Mach numbers, is small compared to the thermal velocity. In the inertial regime, viscous dissipation is low relative to inertia, and the opposite is true in the viscous regime. The conventional way to determine the regime of a fluid flow is by using the Reynolds number defined as the ratio of the two timescales,

$$\mathrm{Re} = \frac{t_{diff}}{t_{adv}} = \frac{\rho u l}{\mu}. \tag{3.2}$$

Fluid dynamics problems can be approached using various methods depending on the relevant length and timescales, see figure 3.1. Because all matter is composed of atoms/molecules, tracking each would in principle capture the whole picture. Macroscopic properties are then derived from the microscopic details. However, such molecular dynamics calculations are possible only for very short time and length scales. At the other extreme, where length and time scales are large,

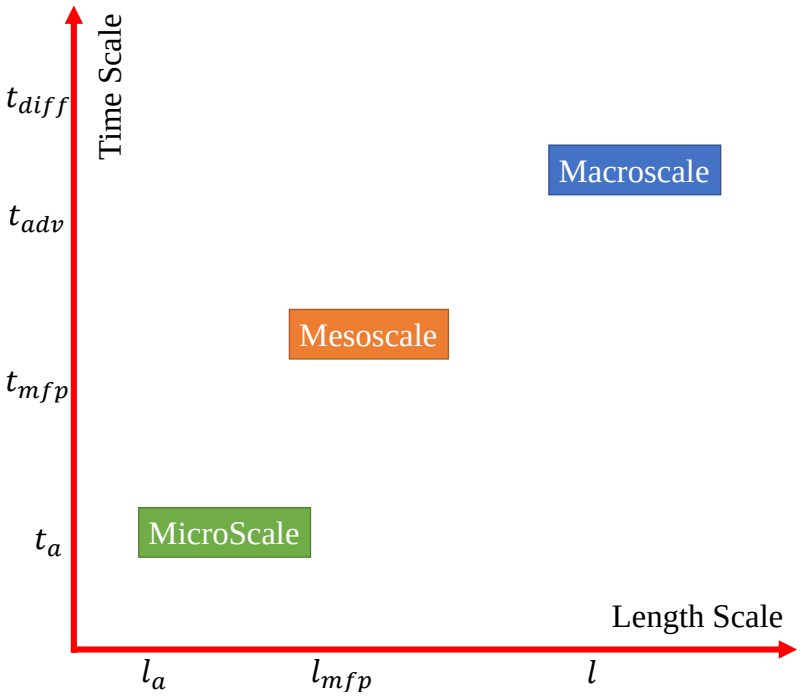

Figure 3.1: Simulation Length and timescales for different methods in fluid dynamics.

the continuum assumption applies and only the macroscopic quantities are tracked using the Navier–Stokes equations. There is an intermediate region between the microscopic and macroscopic pictures. Here, the average behaviour of collections of atoms/molecules is tracked using statistical methods and kinetic theory. This region is termed *mesoscopic*. Macroscopic quantities are calculated from moments of the statistical distributions of these collections of atoms/molecules. The Lattice Boltzmann method is a mesoscopic method where the fundamental quantity is the probability distribution function whose evolution in time and space is governed by the Boltzmann equation.

3.2 The Boltzmann Equation

The density function $f(\boldsymbol{x}, \boldsymbol{\xi}, t)$, the fundamental quantity in the Lattice Boltzmann method, determines the probability of finding a particle at position near $\boldsymbol{x}$, moving at a molecular velocity $\boldsymbol{\xi}$ at time t. The position and molecular velocity are the

micro–state variables in the statistical mechanics of a gas system. If an external force density $\boldsymbol{F}$ acts on a particle in the system, in the absence of collisions, it will be translated in a time period dt from $\boldsymbol{x}$ to a new position $\boldsymbol{x} + \Delta\boldsymbol{x} = \boldsymbol{x} + \boldsymbol{\xi}dt$ with a new velocity $\boldsymbol{\xi} + \Delta\boldsymbol{\xi} = \boldsymbol{\xi} + \frac{\boldsymbol{F}}{\rho}dt$. As a consequence the distribution will be shifted such that

$$f\left(\boldsymbol{x} + \boldsymbol{\xi}dt, \boldsymbol{\xi} + \frac{\boldsymbol{F}}{\rho}dt, t + dt\right) - f(\boldsymbol{x}, \boldsymbol{\xi}, t) = 0. \tag{3.3}$$

This purely translational step is called *streaming*. This means that along characteristics given by $\frac{d\boldsymbol{x}}{dt} = \boldsymbol{\xi}$ and $\frac{d\boldsymbol{\xi}}{dt} = \frac{\boldsymbol{F}}{\rho}$, f remains constants. We can write this as,

$$\frac{\mathrm{d}f}{\mathrm{d}t} = \frac{\partial f}{\partial t} + \boldsymbol{\xi} \cdot \frac{\partial f}{\partial \boldsymbol{x}} + \frac{\boldsymbol{F}}{\rho} \cdot \frac{\partial f}{\partial \boldsymbol{\xi}} = 0. \tag{3.4}$$

Equation (3.4) is the Boltzmann equation without a source term. Collisions between molecules will cause them to exchange momenta that will cause f to relax back towards local thermodynamic equilibrium. This is captured by introducing a source term $\Omega(f)$, so that equation (3.4) becomes

$$\frac{\mathrm{d}f}{\mathrm{d}t} = \frac{\partial f}{\partial t} + \boldsymbol{\xi} \cdot \frac{\partial f}{\partial \boldsymbol{x}} + \frac{\boldsymbol{F}}{\rho} \cdot \frac{\partial f}{\partial \boldsymbol{\xi}} = \Omega(f). \tag{3.5}$$

Equation (3.5) is the full Boltzmann equation. It can be shown that integrating equation (3.5) and taking appropriate moments leads to the Navier–Stokes equation, see for example (Sukop and Thorne, 2006; Krüger et al., 2016) for more details. Therefore, solving (3.5) indirectly solves the Navier–Stokes equations. However, in general, it is more challenging to solve (3.5) *analytically* than the Navier–Stokes equations since it requires determining the entire distribution of molecular velocities at each point rather than just the ensemble mean velocity.

However, solving equation (3.5) *numerically*, using *streaming* and *collision* steps, is comparatively simple in terms of implementation and parallelisation. This simplicity compared with numerical solutions of the Navier–Stokes equations has increased attention event even though it involves solving for the entire velocity distribution. This numerical method of solving the Boltzmann equation, and hence indirectly solving the Navier–Stokes equations, is called the Lattice Boltzmann *Method*.

3.3 The Lattice Boltzmann Method

As previously mentioned, LBM solves equation (3.5) using a streaming and collision process to solve the Boltzmann equation. To achieve this, the equation needs to be discretised in space, velocity and time, and its collision operator defined in a discrete and solvable form. Macroscopic quantities also need to be derived from the solutions. Space $\boldsymbol{x}$ discretisation is done by introducing a cubic lattice with edge length $\Delta\boldsymbol{x}$, with f defined only at the lattice vertices. The values of f are updated with timestep Δt. The steps in time Δt and space $\Delta\boldsymbol{x}$ define the resolution in a chosen set of units, conventionally artificial lattice units are adopted such that Δt and $\Delta\boldsymbol{x}$ are both equal to unity. Conversion between these units and another set of units, such as SI units, is straightforward. However, we also require a discretisation of velocity $\boldsymbol{\xi}$.

The continuous velocity space is discretised to a set of velocity vectors and corresponding weights $\{\boldsymbol{e}_i, \boldsymbol{w}_i\}$ which correspond to velocity required to move to a neighbouring lattice point in time Δt, so that the velocity $\boldsymbol{e}_i$ are give in units of $\Delta\boldsymbol{x}/\Delta t$, see figure 3.2. These velocity sets are denoted by DdQq, where d is the number of spatial dimensions and q is the number of discrete velocity vectors. The most commonly used velocity sets in fluid mechanical applications are D2Q9 and D3Q19 in 2D and 3D problems respectively, we use these sets throughout this thesis.

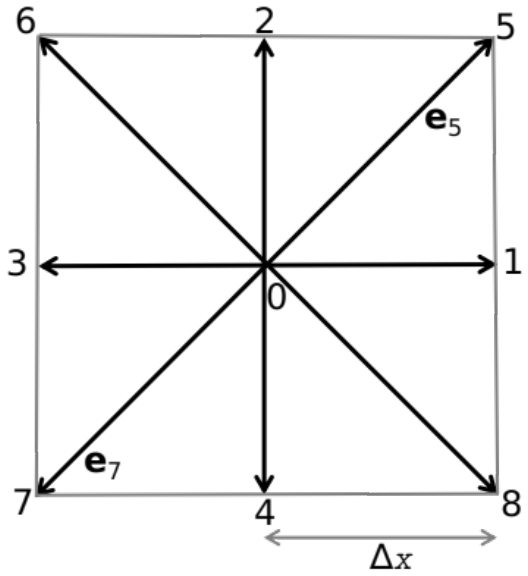

Figure 3.2: The D2Q9 velocity discretisation. The spacing between lattice sites is $\Delta \boldsymbol{x}$ and each velocity vecot reaches a neightbouring lattice site in time Δt.

Table 3.1: Definition of D2Q9 velocity set written explicitly with corresponding weights, commonly used for 2D fluid mechanics problems.

i	0	1	2	3	4	5	6	7	8
w_i	4/9	1/9	1/9	1/9	1/9	1/36	1/36	1/36	1/36
e_{ix}	0	1	0	-1	0	1	-1	-1	1
e_{iy}	0	0	1	0	-1	1	1	-1	-1

The D2Q9 and D3Q19 velocity sets are in tables 3.1 and 3.2 respectively.

Various collision terms have been proposed to approximate the original term proposed by Boltzmann; a cumbersome double integral that takes into account all possibilites of a two–body collision (Krüger et al., 2016). The most commonly used collision operator is the BGK operator developed by Bhatnagar et al. (1954) and by Welander (1954) at the same time (Mohamad, 2019). This is written as,

$$\Omega(f) = -\frac{1}{\tau}(f - f^{eq}). \tag{3.6}$$

Equation (3.6) relaxes the local distribution function f to the local equilibrium distribution function f^{eq} at a timescale τ. f^{eq} is the equilibrium density function

Table 3.2: Definition of D3Q19 velocity set written explicitly with corresponding weights, commonly used for 3D fluid mechanics problems.

i	w_i	e_{ix}	e_{iy}	e_{iz}
0	1/3	0	0	0
1	1/18	1	0	0
2	1/18	-1	0	0
3	1/18	0	1	0
4	1/18	0	-1	0
5	1/18	0	0	1
6	1/18	0	0	-1
7	1/36	1	1	0
8	1/36	-1	-1	0
9	1/36	1	0	1
10	1/36	-1	0	-1
11	1/36	0	1	1
12	1/36	0	-1	-1
13	1/36	1	-1	0
14	1/36	-1	1	0
15	1/36	1	0	-1
16	1/36	-1	0	1
17	1/36	0	1	-1
18	1/36	0	-1	1

arises given by the minimisation of the free energy of a gas system, which is given by,

$$f^{eq}(\boldsymbol{\xi}) = \frac{\rho}{(2\pi RT)^{3/2}} \exp\left(-\frac{1}{2RT}(\boldsymbol{\xi} - \boldsymbol{u})^2\right), \tag{3.7}$$

where ρ is the macroscopic density, $\boldsymbol{\xi}$ the microscopic velocity, $\boldsymbol{u}$ the macroscopic density, T the absolute temperature, and R the specific gas constant. Using Hermite polynomials and discretisation, an approximate discrete form of f^{eq} can be written as,

$$f^{eq}(\omega_i, \boldsymbol{e}_i) = f_i^{eq} = w_i \rho \left(1 + \frac{\boldsymbol{u} \cdot \boldsymbol{e}_i}{c_s^2} + \frac{(\boldsymbol{u} \cdot \boldsymbol{e}_i)^2}{2c_s^4} - \frac{\boldsymbol{u} \cdot \boldsymbol{u}}{2c_s^2}\right), \tag{3.8}$$

where w_i are the weights of the corresponding velocity set, $\boldsymbol{u}$ is the macroscopic velocity, and c_s the speed of sound corresponding to the velocity set defined later in this section. Using equation (3.3) and (3.6), we can write

$$f\left(\boldsymbol{x} + \boldsymbol{\xi}dt, \boldsymbol{\xi} + dt\boldsymbol{F}/m, t + dt)\right) - f(\boldsymbol{x}, \boldsymbol{\xi}, t) = -\frac{\Delta t}{\tau}(f(\boldsymbol{x}, \boldsymbol{\xi}, t) - f^{eq}(\boldsymbol{\xi})). \tag{3.9}$$

The moments of f give the macroscopic variables of density and momentum. Density is, by definition, the zeroth moment Π_0,

$$\Pi_0 = \rho(\boldsymbol{x}, t) = \int f(\boldsymbol{x}, \boldsymbol{\xi}, t) d\boldsymbol{\xi} = \sum_i f_i = \sum_i f_i^{eq}. \tag{3.10}$$

Similarly, the momentum density is obtained from the first moment,

$$\Pi_1 = \rho(\boldsymbol{x}, t)\boldsymbol{u}(\boldsymbol{x}, t) = \int \boldsymbol{\xi} f(\boldsymbol{x}, \boldsymbol{\xi}, t) d\boldsymbol{\xi} = \sum_i \boldsymbol{e}_i f_i = \sum_i \boldsymbol{e}_i f_i^{eq}. \tag{3.11}$$

Velocity $\boldsymbol{u}(\boldsymbol{x}, t)$ is the result of dividing equation (3.11) by $\rho(\boldsymbol{x}, t)$. The Chapman–Enskog analysis, see (Chapman and Cowling, 1952), derives the link between the Boltzmann equation and the Navier–Stokes equations and demonstrates that they are equivalent with kinematic viscosity given by

$$\nu = c_s^2 \left(\tau - \frac{\Delta t}{2} \right), \tag{3.12}$$

and pressure by

$$p(\boldsymbol{x}, t) = c_s^2 \rho(\boldsymbol{x}, t). \tag{3.13}$$

where c_s is the speed of sound given by $c_s^2 = \left(\partial p / \partial \rho\right)_s$ and in the case of an isothermal system $c_s^2 = RT$. The relation is used in the approximation of f^{eq} using Hermite polynomials in equation (3.8) and each velocity discretisation DdQq has a unique value of c_s. Both D2Q9 and D3Q19 both have $c_s^2 = 1/3$. We are now ready to implement an LBM algorith using the streaming and collision steps. For each discrete velocity the collision step can be written as,

$$f_i^*(\boldsymbol{x}, t) = f_i(\boldsymbol{x}, t) - \frac{\Delta t}{\tau}(f_i(\boldsymbol{x}, t) - f_i^{eq}), \tag{3.14}$$

where f_i^* is the post–collision distribution function, f_i^{eq} is found using (3.8). An alternative implementation steps that is reportedly faster especially when $\tau = \Delta t$ is

(Krüger et al., 2016),

$$f_i^*(\boldsymbol{x},t) = f_i(\boldsymbol{x},t)\left(1-\frac{\Delta t}{\tau}\right) + f_i^{eq})\frac{\Delta t}{\tau}. \tag{3.15}$$

In the absence of an external force, the streaming step can implemented as,

$$f_i(\boldsymbol{x}+\boldsymbol{e}_i\Delta t, t+\Delta t) = f_i^*(\boldsymbol{x},t). \tag{3.16}$$

To include a force, we rewrite equation (3.9) to include the forcing term,

$$f\left(\boldsymbol{x}+\boldsymbol{\xi}dt, \boldsymbol{\xi}+dt\boldsymbol{F}/m, t+dt\right)) - f(\boldsymbol{x},\boldsymbol{\xi},t) = [\Omega_i(\boldsymbol{x},t) - S_i(\boldsymbol{x},t)]\Delta t, \tag{3.17}$$

where S_i is given by (Guo et al., 2002),

$$S_i = (1-1/2\tau)F_i, \tag{3.18}$$

and F_i is given by

$$F_i = \omega_i\left[\frac{\boldsymbol{e}_i-\boldsymbol{u}}{c_s^2} + \frac{\boldsymbol{e}_i\cdot\boldsymbol{u}}{c_s^4}\boldsymbol{e}_i\right]\cdot\boldsymbol{F}. \tag{3.19}$$

The density can still be found using (3.10) but the momentum density is now given by,

$$\rho\boldsymbol{u} = \sum_i \boldsymbol{e}_i f_i + \frac{\boldsymbol{F}\Delta t}{2\rho}, \tag{3.20}$$

this correction is performed before calculating f^{eq}.

3.4 Multiphase Lattice Boltzmann

The LBM method described above is for a single–phase fluid. To simulate printing onto real surfaces under realistic conditions, the chosen model has to capture multiphase flows with a high–density ratio $O(10^3)$ between phases. It also has to simulate micro–droplet impact onto a surface within the parameter space presented in chapter 1. This requires the simulation to remain stable at a high–density ratio, and appropriate viscosity ratio, and velocity. It also needs to capture contact angle wetting in the presence of topography without diverging.

There are four main approaches in LBM to multiphase flows: colour–gradient (Rothman and Keller, 1988), pseudo–potential (Shan and Chen, 1993; 1994), free–energy (Swift et al., 1995), and phase–field (He et al., 1999). The colour–gradient assigns a colour for each phase and tracks it with a density function, introduces an extra collision term and performs an additional recolouring step compared with single–phase models. The pseudo–potential model introduces an interactive force that scales with a density–dependent term called pseudo–potential which replaces the ideal EOS in equation (3.13) with a non–monotonic EOS that results in two stable phases. As its name implies, the free–energy starts with a free energy functional that describes the desired multiphase system from which a representative force or pressure tensor is derived and inserted in the Lattice Boltzmann equation. The phase–field is described as a descendant of van der Waals and Cahn–Hilliard classical approaches, it introduces an order parameter to track the interface given by an additional distribution function.

Each of these approaches struggle with all or some of the following challenges:

- Spurious velocities around the interface. When simulating a static droplet, for example, velocity should be **0** everywhere in the system; unexpected velocities

appear near the interface in the four models, however. The magnitude of these spurious velocities differs among models. These currents cause numerical instability. However, if these velocities are small compared with the system speed, the issue can be ignored.

- Small density ratio between phases constraint. These models in their original form are all constrained to density ratios of O(10) except the pseudo–potential model which is capable of O(100) ratios. Increasing the density ratio increases spurious currents. Many applications such as droplet fall in air are characterised by a density ratio of O(1000).

- Small surface tension forces. The range of achievable surface tension (in lattice units) achievable in these models is limited and restricts the accessible parameter space. Increasing surface tension also increases spurious currents. The pseudo–potential model in its original form cannot vary the surface tension and density ratio independently. This poses a challenge for performing parametric studies.

Numerous modifications of the four models have been proposed to overcome these issues and it is still an active area of research. We will not detail these proposed models here nor the differences between the four models and their weaknesses and strengths, refer to Huang et al. (2015) and Li et al. (2016) for such comparisons. We note, however, that the pseudo–potential is the simplest, most efficient, and the model with most extensions and studies of the four models. Therefore, we present it in its basic form in the rest of this chapter and employ an appropriate extension, validate it and accelerate it in the next chapter.

3.5 The Pseudo-Potential Model

A sufficiently attractive force between a gas molecules will cause two phases to form: liquid and gas. This fact inspired Shan and Chen (1993) to introduce an attractive force between the molecules. The force needs to be attractive, i.e. negative in sign, additive, i.e proportional to $\rho(\boldsymbol{x})\rho(\bar{\boldsymbol{x}})$ where $\boldsymbol{x} \neq \bar{\boldsymbol{x}}$ and dependant on the distance between molecules, this can be represented by distance dependent Green's function $G(\boldsymbol{x}, \bar{\boldsymbol{x}})$. The force can be written as (Krüger et al., 2016),

$$\boldsymbol{F}_{int}(\boldsymbol{x}) = -\int (\bar{\boldsymbol{x}} - \boldsymbol{x}) G(\bar{\boldsymbol{x}}, \boldsymbol{x}) \psi(\boldsymbol{x}) \psi(\bar{\boldsymbol{x}}) d^3\bar{x}, \tag{3.21}$$

where, to avoid numerical instability at high densities, density ρ has been replaced with an effective density ψ called *pseudo-potential*, hence the name of the method. Shan and Chen (1993) proposed ψ be given by,

$$\psi(\rho) = \rho_0[1 - \exp(-\rho/\rho_0)], \tag{3.22}$$

where ρ_0 is a reference density usually kept at unity. Equation (3.22) bounds ψ between 0 and ρ_0 keeping the pseudo–potential finite even for large densities. The pseudo–potential model also assumes the force is short ranged, most commonly to lattice nodes connected by $\boldsymbol{e}_i \Delta t$. The force is assumed isotropic so it depends on the magnitude of the distance between molecules $|\boldsymbol{x} - \bar{\boldsymbol{x}}|$. The Green's function is therefore given by,

$$G(\bar{\boldsymbol{x}}, \boldsymbol{x}) = \begin{cases} \omega_i G & if\ \bar{\boldsymbol{x}} = \boldsymbol{x} + \boldsymbol{e}_i \Delta t \\ 0 & \text{otherwise} \end{cases}. \tag{3.23}$$

the spatially disctretised force $\boldsymbol{F}_{int}$ can be written as (Shan and Chen, 1994),

$$\boldsymbol{F}_{int}(\boldsymbol{x},t) = -G\psi(\boldsymbol{x},t)\sum_i w_i\psi(\boldsymbol{x}+\boldsymbol{e}_i\Delta t,t)\boldsymbol{e}_i\Delta t. \tag{3.24}$$

The magnitude of G in (3.24) is used to control the strength of the interaction force. Taylor expanding $\psi(\boldsymbol{x}+\boldsymbol{e}_i\Delta t,t)$ about $\boldsymbol{x}$, substituting into (3.24) and including terms up to third order,

$$\boldsymbol{F}_{int} = -G\psi\left(c_s^2\Delta t^2\boldsymbol{\nabla}\psi + \frac{c_s^2\Delta t^4}{2}\boldsymbol{\nabla}\boldsymbol{\nabla}^2\psi\right). \tag{3.25}$$

The first term in (3.25) has the form of a gradient in the pseudo–potential and can be considered as an addition to the pressure giving a pseudo–potential EOS as (Krüger et al., 2016)

$$p = c_s^2\rho + \frac{c_s^2 G}{2}\psi^2(\rho). \tag{3.26}$$

Plotting equation (3.26) for multiple values of G with $\rho_0 = 1$ and $c_s^2 = 1/3$ in figure 3.3, we can see that the pressure becomes multivaluesd for a range of pressures for $|G| \geq 4$ with two stable equilibrium densities a liquid ρ_l and gas ρ_g densities separated by an unstable intermediate state as seen for $p = p_0$ in figure 3.3. The maximum achievable density ratio before the system becomes unstable is ≈ 70 when $G \approx -7$.

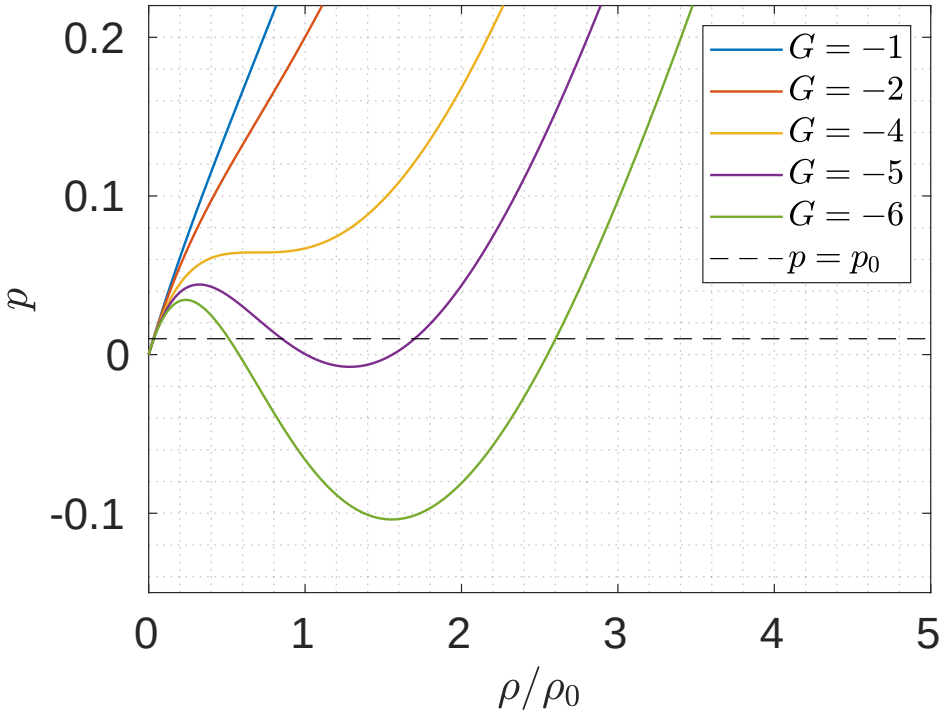

Figure 3.3: Phase separation from EOS in equation (3.26) for various values of G.

3.5.1 Surface Tension

Surface tension is an emergent property in the pseudo–potential model. To calculate surface tension, the Young–Laplace law given by

$$\Delta P = \begin{cases} \gamma \frac{1}{R} & \text{in 2D} \\ 2\gamma \frac{1}{R} & \text{in 3D} \end{cases}. \tag{3.27}$$

Equation equation (3.27) is exploited by simulating a series of droplets with varying radii R. The pressure differences between the inside and outside of the droplets Δp is calculated in the simulation. The pressure differences Δp and the inverse of the droplet radii R^{-1} are plotted. The relationship is a straight line with the surface tension γ in 2D, or 2γ in 3D, as the slope. The surface tension depends on the strength of the interaction force G which also changes the density ratio, hence surface tension cannot be varied without varying the density ratio, and vice–versa.

This Young–Laplace test is used later in figure 4.1.

3.5.2 Wetting

The easiest way to achieve a certain contact angle (θ) with a solid boundary is to introduce a force similar to that in equation (3.17) between the solid nodes and boundary nodes, i.e. fluid cells closes to the solid boundary. This force, technically a force density, between solid and boundary nodes $\boldsymbol{F}^s_{int}$ is given by,

$$\boldsymbol{F}^s_{int}(\boldsymbol{x}, t) = -G\psi(\boldsymbol{x}, t) \sum_{i}^{solid} w_i \psi(\rho_s) \boldsymbol{e}_i \Delta t, \tag{3.28}$$

where ρ_s is an effective density at solid nodes chosen to achieve a specific contact angle. The range of achievable contact angle depends, not only on ρ_s, but also on the value of G. A calibration between $\{G, \rho_s\}$ and θ is needed, see Wilson and Kubiak (2016) for an example.

As implemented above, the pseudo–potential model captures density ratios only up to 70. We cannot manipulate surface tension without changing the density ratio, and we expect an issue will arise with the current wetting model as the density ratio increases. The next chapter investigates extensions of this SC model to mitigate these issues.

3.6 Summary

We have derived the discrete Lattice Boltzmann equation and presented its implementation for a single–phase fluid. We have chosen the pseudo–potential model for this thesis and implemented it in its original form, demonstrated how the Laplace–Young law is used to find surface tension and presented how a partial wetting con-

dition is achieved. Because of the constraint on density ratio and surface tension of the pseudo–potential model, we will investigate extending it to appropriate density ratio, appropriate surface tension, and contact angle options in the next chapter.

Chapter 4 | Extending the LBM Method

Contents

As presented in the previous chapter, the original pseudo–potential multiphase model is not able to simulate density ratios above O(100), struggles with spurious currents, low surface tension and thermodynamic inconsistency. It is also not clear if the constant wall density model will be stable in a high–density ratio simulation. In this chapter, we present the various modifications that have been proposed to mitigate these issues using various strategies. Various collision operators section 4.1, equations of state section 4.2, force capturing schemes section 4.3, and forms of interactive force section 4.4 have been proposed. We briefly present these and choose a form of the pseudo–potential model with appropriate modifications. The geometric wetting model is presented in section 4.7. We then validate the model with wetting in section 4.8 and accelerate its execution in section 4.9.

4.1 Collision Operators

A collision operator has to conserve mass, momentum, and, in the case of the Lattice Boltzmann Method, translational energy. These conservation restrictions can be written as moments of the collision operator, with mass conservation given by

$$\int \Omega(f)\mathrm{d}^3\xi = \sum_i \Omega_i(f_i) = -\sum_i s(f_i - f_i^{eq}) = 0, \tag{4.1}$$

and momentum conservation given by

$$\int \boldsymbol{\xi}\Omega(f)\mathrm{d}^3\xi = \sum_i \boldsymbol{e}_i\Omega_i(f_i) = -\sum_i s(f_i\boldsymbol{e}_i - f_i^{eq}\boldsymbol{e}_i) = \mathbf{0}. \tag{4.2}$$

There are three commonly used collision operators in LBM: the single relaxation time operator discussed in chapter 4, also called BGK, Multiple Relaxation Times (MRT) and Two Relaxation Times (TRT). The two former variations have been used in multiphase LBM pseudopotential models; we discuss them next.

4.1.1 BGK Collision Operator

The most commonly used collision is the BGK operator which relaxes the local distribution equilibrium to the equilibrium distribution function as discussed in 3,

$$\Omega(f) = -\frac{1}{\tau}(f - f^{eq}). \tag{4.3}$$

This operator is considered the simplest collision operator that satisfies the constraints in equations 4.1 and 4.2. It is also the most efficient and easiest to implement but this comes at the cost of reduced stability and accuracy (Krüger et al., 2016). When increasing Reynolds number in LBM simulations and to avoid increasing lattice (grid) resolution, either the viscosity (i.e. relaxation time τ) is decreased or velocity is increased. However, there are limits to how low τ and how high $\boldsymbol{u}$ can go. The relaxation time has to be greater than 0.5 and $u << c_s$ for stability. To overcome these limitations, collision operators with more degrees of freedom have been proposed, including MRT.

4.1.2 Multiple Relaxation Times (MRT)

The BGK single relaxation time uses a single relaxation rate $s = 1/\tau$, MRT, as the name implies, uses multiple relaxation rates s_i and performs the relaxation step in the moments space rather than population space. We can rewrite equations 4.1 and 4.2 as,

$$\int \Omega(f)\mathrm{d}^3\xi = \sum_i \Omega_i(f_i) = -\sum_i s(f_i - f_i^{eq}) = -s(\rho - \rho^{eq}) = 0, \tag{4.4}$$

and

$$\int \boldsymbol{\xi}\Omega(f)\mathrm{d}^3\xi = \sum_i \boldsymbol{e}_i\Omega_i(f_i) = -\sum_i s(f_i\boldsymbol{e}_i - f_i^{eq}\boldsymbol{e}_i) = -s(\rho\boldsymbol{u} - \rho^{eq}\boldsymbol{u}^{eq}) = \boldsymbol{0}. \quad (4.5)$$

MRT starts by converting the population space f_i to the moment space, applies a relaxation step to the equilibrium moment space, then converts this equilibrium moment space back to the population space. We can see how this works by looking at the original discrete Boltzmann equation with the BGK operator in the absence of a force in vector form,

$$\boldsymbol{f}(\boldsymbol{x} + \boldsymbol{e}_i\Delta t, t + \Delta t) - f(\boldsymbol{x}, t) = -\Delta t s\left(f(\boldsymbol{x}, t) - f^{eq}(\boldsymbol{x}, t)\right). \quad (4.6)$$

Multiplying through by an identity matrix $\boldsymbol{I} = \boldsymbol{M}^{-1}\boldsymbol{M}$ where $\boldsymbol{M}$ is an invertible matrix called a *collision matrix*,

$$\begin{aligned}
\boldsymbol{f}(\boldsymbol{x} + \boldsymbol{e}_i\Delta t, t + \Delta t) - \boldsymbol{f}(\boldsymbol{x}, t) &= -\boldsymbol{M}^{-1}\boldsymbol{M}\Delta t s\left(\boldsymbol{f}(\boldsymbol{x}, t) - \boldsymbol{f}^{eq}(\boldsymbol{x}, t)\right) \\
&= -\boldsymbol{M}^{-1}\Delta t s\left(\boldsymbol{M}\boldsymbol{f}(\boldsymbol{x}, t) - \boldsymbol{M}\boldsymbol{f}^{eq}(\boldsymbol{x}, t)\right) \\
&= -\boldsymbol{M}^{-1}\Delta t s\boldsymbol{I}\left(\boldsymbol{m}(\boldsymbol{x}, t) - \boldsymbol{m}^{eq}(\boldsymbol{x}, t)\right) \\
&= -\boldsymbol{M}^{-1}\Delta t\boldsymbol{\Lambda}\left(\boldsymbol{m}(\boldsymbol{x}, t) - \boldsymbol{m}^{eq}(\boldsymbol{x}, t)\right),
\end{aligned} \quad (4.7)$$

where $\boldsymbol{m}$ is a vector of moments $\boldsymbol{m} = \boldsymbol{M}\boldsymbol{f}$, $\boldsymbol{m}^{eq}$ is a vector of equilibrium moments $\boldsymbol{m}^{eq} = \boldsymbol{M}\boldsymbol{f}^{eq}$, and $\boldsymbol{\Lambda} = s\boldsymbol{I} = \mathrm{diag}(s, ..., s)$ is a diagonal matrix that relaxes all moments with one rate s using the term $\boldsymbol{\Lambda}\left(\boldsymbol{m} - \boldsymbol{m}^{eq}\right)$. The result is then multiplied by the inverse matrix $\boldsymbol{M}^{-1}$ to transform it back to population space. MRT suggests instead of using a diagonal matrix of the same relaxation rate s, using a different rate for each moment, $\boldsymbol{\Lambda} = \mathrm{diag}\left(s_0, ..., s_{q-1}\right)$, where q is the number of velocity

vectors, recall the notation DdQq.

The diagonal relaxation matrix $\mathbf{\Lambda}$ and the collision matrix $\boldsymbol{M}$, and hence $\boldsymbol{M}^{-1}$, can take different but equivalent forms depending on how they are derived. The most commonly used collision matrix is that derived using the Gram–Schmidt procedure (D'Humières et al., 2002). The relaxation and collision matrices and inverse matrices can be respectively written for the D2Q9 as,

$$\mathbf{\Lambda} = \mathrm{diag}(0, s_\zeta, s_\pi, 0, s_q, 0, s_q, s_\nu, s_\nu), \tag{4.8}$$

$$\boldsymbol{M} = \begin{bmatrix} 1 & 1 & 1 & 1 & 1 & 1 & 1 & 1 & 1 \\ -4 & -1 & -1 & -1 & -1 & -1 & 0 & 1 & 0 \\ 1 & -1 & -1 & 0 & 0 & 1 & 1 & -1 & 0 \\ 1 & -1 & -1 & -1 & 1 & 0 & 0 & 1 & 0 \\ 1 & -1 & -1 & 0 & 0 & -1 & 1 & -1 & 0 \\ 1 & 1 & 1 & 1 & 1 & 1 & 1 & 0 & 1 \\ 1 & 1 & 1 & -1 & -1 & 1 & 1 & 0 & -1 \\ 1 & 1 & 1 & -1 & -1 & -1 & -1 & 0 & 1 \\ 1 & 1 & 1 & 1 & 1 & 1 & 1 & 0 & -1 \end{bmatrix}, \tag{4.9}$$

and

$$\boldsymbol{M^{-1}} = \begin{bmatrix} \frac{1}{9} & -\frac{1}{9} & \frac{1}{9} & 0 & 0 & 0 & 0 & 0 & 0 \\ \frac{1}{9} & -\frac{1}{36} & -\frac{1}{18} & \frac{1}{6} & -\frac{1}{6} & 0 & 0 & \frac{1}{4} & 0 \\ \frac{1}{9} & -\frac{1}{36} & -\frac{1}{18} & 0 & 0 & \frac{1}{6} & \frac{1}{6} & -\frac{1}{4} & 0 \\ \frac{1}{9} & -\frac{1}{36} & -\frac{1}{18} & -\frac{1}{6} & \frac{1}{6} & 0 & 0 & \frac{1}{4} & 0 \\ \frac{1}{9} & -\frac{1}{36} & -\frac{1}{18} & 0 & 0 & -\frac{1}{6} & \frac{1}{6} & -\frac{1}{4} & 0 \\ \frac{1}{9} & \frac{1}{18} & \frac{1}{36} & \frac{1}{6} & \frac{1}{12} & \frac{1}{6} & \frac{1}{12} & 0 & \frac{1}{4} \\ \frac{1}{9} & \frac{1}{18} & \frac{1}{36} & -\frac{1}{6} & -\frac{1}{12} & \frac{1}{6} & \frac{1}{12} & 0 & -\frac{1}{4} \\ \frac{1}{9} & \frac{1}{18} & \frac{1}{36} & -\frac{1}{6} & -\frac{1}{12} & -\frac{1}{6} & -\frac{1}{12} & 0 & \frac{1}{4} \\ \frac{1}{9} & \frac{1}{18} & \frac{1}{36} & \frac{1}{6} & \frac{1}{12} & \frac{1}{6} & \frac{1}{12} & 0 & -\frac{1}{4} \end{bmatrix}. \tag{4.10}$$

where s_ζ and s_ν determine the bulk and kinematic shear viscosities respectively. s_π and s_q are relaxation rates for non–hydrodynamic moments that can be tuned to ensure the stability of the simulation.

Similar matrices can be found for the D3Q19 velocity set. The collision matrix can be found in Krüger et al. (2016) and the inverse matrix can be readily found using mathematical software. The relaxation matrix is,

$$\boldsymbol{\Lambda} = \mathrm{diag}(1, s_\zeta, s_\nu, 1, 1, s_q, 1, s_q, s_\nu, s_\nu, s_q, s_q, s_q, s_q, s_q, s_\pi s_m, s_m, s_m). \tag{4.11}$$

where s_m is also a relaxation rates for non–hydrodynamic moment. The multiple relaxation time (MRT) collision operator is written as

$$\Omega_{\alpha\beta} = (\boldsymbol{M^{-1}\Lambda M})_{\alpha\beta}, \tag{4.12}$$

where $\boldsymbol{M}$ is the collision matrix and $\boldsymbol{\Lambda}$ is a diagonal relaxation matrix used to relax the various moments of the distribution density function at various rates.

The most commonly used collision matrix is that derived using the Gram–

Schmidt procedure (D'Humières et al., 2002), however, an equivalent but more efficient and easier to implement matrix has been derived by Li et al. (2019), which is used in this work, its corresponding diagonal relaxation matrix is given by

$$\mathbf{\Lambda} = \mathrm{diag}(1, 1, 1, 1, s_\zeta, s_\nu, s_\nu, s_\nu, s_\nu, s_\nu, s_q, s_q, s_q, s_q, s_q, s_q, s_\pi s_\pi, s_\pi, s_\pi), \tag{4.13}$$

where s_ζ and s_ν determine the bulk and kinematic shear viscosities respectively. s_π and s_q are relaxation rates for non–hydrodynamic moments that can be tuned to ensure the stability of the simulation. The collision matrix can be found in Li et al. (2019) and its inverse readily computed.

4.2 Equations of State

Incorporating various equations of state into the pseudo–potential has been shown to allow accessing higher density ratios and surface tension. This model results in a pressure, $p = c_s^2\rho + \psi^2\frac{c_s^2 G}{2}$, supporting two phases, where $c_s = 1/\sqrt{3}$ is the speed of sound of the lattice (Shan and Chen, 1993). Yuan and Schaefer (2006) showed that this equation of state, with the choice of $\psi(\boldsymbol{x}, t) = \rho_0(1 - \exp(-\rho/\rho_0))$ originally proposed by Shan and Chen (1993), is limited in terms of achievable density ratio between the liquid and vapour phases and instead proposed using a different expression for $\psi(\boldsymbol{x}, t)$,

$$\psi(\boldsymbol{x}, t) = \sqrt{\frac{2(p - c_s^2\rho(\boldsymbol{x}, t))}{c_s^2 G}}. \tag{4.14}$$

This enables using different equations of state for pressure such as the Carnahan–Starling equation of state used in this work,

$$p = \rho RT\frac{1 + b\rho/4 + (b\rho/4)^2 - (b\rho/4)^3}{(1 - b\rho/4)^3} - a\rho^2, \tag{4.15}$$

where $a = 0.49963R^2T_c^2/p_c$ and $b = 0.18727RT_c/p_c$, where T_c and p_c are the critical temperature and pressure respectively, T is temperature, and R is the universal gas constant set to 1. The parameter a physically represents the strength of the molecular interaction in the EOS and lowering it results in a thicker interface and a more stable simulation at higher density ratios Li et al. (2013). Reducing T in (4.15) increases the density of the liquid and lowers that of the gas, hence increasing the density ratio. The parameter b represents the volume occupied by the material's atoms and is chosen arbitrarily and kept constant.

Other commonly used equations of state in the pseudo–potential model include: vand der Waals, Redlich–Kwong, Redlich–Kwong Soave, and Peng–Robinson, for a review on these refer to Yuan and Schaefer (2006).

4.3 Force Capturing Schemes

Various force capturing methods have been proposed to improve the original pseudo–potential model. For detailed discussions on forcing schemes, refer to Guo et al. (2002) and Huang et al. (2011). Krüger et al. (2016) present the various force capturing schemes by rewriting the discrete form of f^{eq} as,

$$f^{eq}(\omega_i, \boldsymbol{e}_i) = f_i^{eq} = w_i\rho\left(1 + \frac{\boldsymbol{u}^{eq}\cdot\boldsymbol{e}_i}{c_s^2} + \frac{(\boldsymbol{u}^{eq}\cdot\boldsymbol{e}_i)^2}{2c_s^4} - \frac{\boldsymbol{u}^{eq}\cdot\boldsymbol{u}^{eq}}{2c_s^2}\right), \tag{4.16}$$

where $\boldsymbol{u}^{eq}$ is given by

$$\boldsymbol{u}^{eq} = \rho^{-1}\sum_i \boldsymbol{e}_i f_i + A\frac{\boldsymbol{F}\Delta t}{\rho}. \tag{4.17}$$

The relevant force capturing schemes can be expressed with different values

of A and the source term in (3.17). The model in 3.3 has a value $A = 1/2$ and source term given by (3.18), this scheme is called *Guo et al. (2002)*. The original approach in the pseudo–potential model uses $A = \tau\Delta t$ and source term $S_i = 0$, this scheme is henceforth called *Shan and Chen velocity shift*. Another method, *He et al. (1999)* uses $A = 1/2$ and a source term S_i^{He} given by,

$$S_i^{He} = \left(1 - \frac{\Delta}{2\tau}\right) \frac{f_i^{eq}(\boldsymbol{e}_i - \boldsymbol{u})}{\rho c_s^2} \cdot \boldsymbol{F}. \tag{4.18}$$

A method proposed by Kupershtokh et al. (2009), called the *exact difference method (EDM)*, is given by $A = 0$ and source term S_i^{EDM} given by

$$S_i^{EDM} = f_i^{eq}(\rho, \bar{\boldsymbol{u}} + \Delta\boldsymbol{u}) - f_i^{eq}(\rho, \bar{\boldsymbol{u}}), \tag{4.19}$$

where $\bar{\boldsymbol{u}} = \sum_i f_i \boldsymbol{e}_i/\rho$ and $\Delta\boldsymbol{u} = \boldsymbol{F}\Delta t/\rho$.

The MRT version of the Guo et al. (2002), we call *MRT–Guo et al. (2002)*,

and the source term is given for D2Q9 by,

$$\boldsymbol{S} = \begin{bmatrix} 0 \\ 6(F_x u_x + F_y u_y) \\ -6(F_x u_x + F_y u_y) \\ F_x \\ -F_x \\ F_y \\ -F_y \\ 2(2F_x u_x - 2F_y u_y) \\ F_y u_x + F_x u_y \end{bmatrix}. \tag{4.20}$$

Similarly the D3Q19 is given by

$$\boldsymbol{S} = \begin{bmatrix} 0 \\ F_x \\ F_y \\ F_z \\ 2\boldsymbol{F}\cdot\boldsymbol{u} \\ 2(2F_xu_x - F_yu_y - F_zu_z) \\ 2(F_yu_y - F_zu_z) \\ F_xu_y + F_yu_x \\ F_xu_z + F_zu_x \\ F_yu_z + F_zu_y \\ c_s^2F_y \\ c_s^2F_x \\ c_s^2F_z \\ c_s^2F_x \\ c_s^2F_z \\ c_s^2F_y \\ 2c_s^2(u_xF_x + u_yF_y) \\ 2c_s^2(u_xF_x + u_zF_z) \\ 2c_s^2(u_yF_y + u_zF_z) \end{bmatrix}. \tag{4.21}$$

4.4 Form of the Interactive Force

To improve the stability of the pseudo–potential model, improved force density terms are proposed. The simple extension is considering not only the nearest neighbours for interactions but also the next neighbours, this is called multirange, refer to Sbragaglia et al. (2007). Another forcing form, called the *beta scheme* or *quadratic forcing*, attempts to improve the isotropy of the force by including a combination of the pseudo–potential at the nearest nodes as well as the square, refer to Gong and Cheng (2012) for more details.

4.5 Pseudo–Potential Model by Li et al.

Li et al. (2012) studied the forcing schemes in section 4.3 and derived the macroscopic equations resulting from them. They then used this analysis and proposed a new force density capturing model, by improving the MRT–Guo et al. (2002), by

rewriting equation (4.20) as

$$\boldsymbol{S} = \begin{bmatrix} 0 \\ 6(F_x u_x + F_y u_y) + \frac{12\sigma|\boldsymbol{F}|^2}{\psi^2(s_\zeta^{-1}-0.5)} \\ -6(F_x u_x + F_y u_y) + \frac{12\sigma|\boldsymbol{F}|^2}{\psi^2(s_\pi^{-1}-0.5)} \\ F_x \\ -F_x \\ F_y \\ -F_y \\ 2(2F_x u_x - 2F_y u_y) \\ F_y u_x + F_x u_y \end{bmatrix}. \tag{4.22}$$

Li et al. (2019) performed a similar analysis for 3D and rewrote the source

term by Guo et al. (2002) in equation (4.21) as

$$\boldsymbol{S} = \begin{bmatrix} 0 \\ F_x \\ F_y \\ F_z \\ 2\boldsymbol{F}\cdot\boldsymbol{u} + \frac{6\sigma|\boldsymbol{F}|^2}{\psi^2(s_\zeta^{-1}-0.5)} \\ 2(2F_xu_x - F_yu_y - F_zu_z) \\ 2(F_yu_y - F_zu_z) \\ F_xu_y + F_yu_x \\ F_xu_z + F_zu_x \\ F_yu_z + F_zu_y \\ c_s^2F_y \\ c_s^2F_x \\ c_s^2F_z \\ c_s^2F_x \\ c_s^2F_z \\ c_s^2F_y \\ 2c_s^2(u_xF_x + u_yF_y) \\ 2c_s^2(u_xF_x + u_zF_z) \\ 2c_s^2(u_yF_y + u_zF_z) \end{bmatrix}. \tag{4.23}$$

Li et al. (2019) proposed a new MRT scheme that is more efficient and simpler to implement. Li et al. (2013; 2019) studied the effect of the parameter a

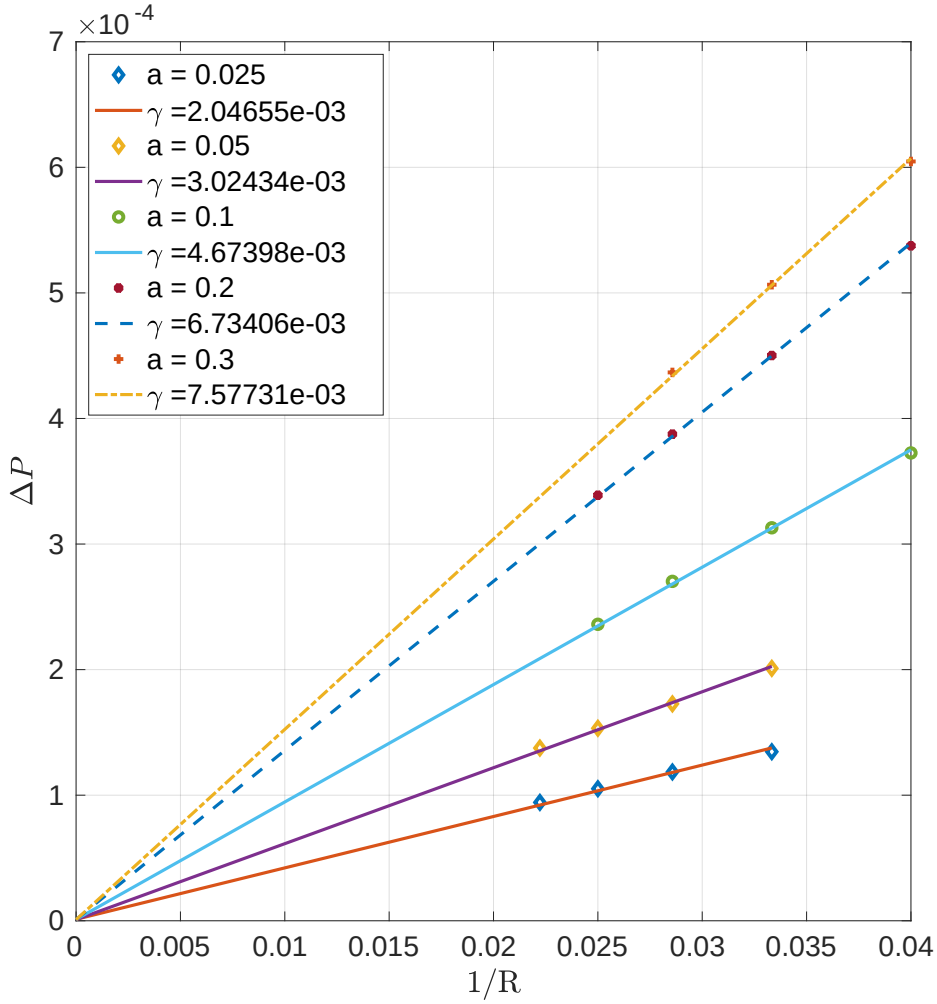

Figure 4.1: Young–Laplace test of the pseudo–potential model with the modifications from Li et al. (2013; 2019). a is the parameter from the Carnahan–Starling EOS, equation (4.15). Increasing a increases surface tension γ in lattice units.

on stability and surface tension. Performing the Young–Laplace test and varying a from equation (4.15), we can see that the surface tension increases with a, we also found the simulations stable for density ratios > 1000 between phases particularly for low values of a.

4.6 Choosing a Version of the Pseudo–Potential Model

The author implemented the original pseudo–potential model by Shan and Chen (1993) in 2D and 3D in C++ code from scratch and then also implemented all the suggested improvements discussed in the previous sections of this chapter. To enable investigating all these options, a GPU version of the code was also implemented by the author to accelerate the simulations, see section 4.9. This not only enabled efficient exploration of model options but also running parametric studies and multiple–droplet simulations in chapters 5 and 6 respectively. This enabled efficient exploration of model options, running parametric studies later in chapter 5 and multiple droplet simulations in chapter 6. Of the modifications proposed in sections 4.14.3, 4.4, and 4.5 and their combinations, we have found those proposed by Li et al. (2012; 2013; 2019), see section 4.5, most suitable for this thesis. It enables us to simulate droplets at density ratio between phases up to O(1000), and control surface tension through the a parameter in the Carnahan Starling Equation of state (4.15). It is also thermodynamically consistent, i.e. its phase separation is consistent with thermodynamic expectations represented in the Maxwell equal–area construction. The spurious currents are also lowered using this model. We discuss partial wetting then validate the model chosen here in combination with the chosen wetting model and finally accelerate it.

4.7 Wetting and CAH Boundary Condition

Various methods can be used to prescribe a contact angle at a wall boundary, such as introducing an interaction force between the solid and fluid nodes (see for example Li et al. (2014)) or prescribing a constant density at the wall to achieve a predetermined contact angle (see for example Castrejón-Pita et al. (2013)). These

methods work well at relatively low density ratios but become unstable at higher values. The prescription of a constant density at the wall also requires calibration to give a specific contact angle whenever the density ratio or the equation of state is changed (Wilson and Kubiak, 2016). An alternative is to use the geometric boundary condition developed by Ding and Spelt (2007), which has been used to simulate inkjet printed droplets at high density ratio without loss of stability, and hence it is used in this study. This condition was originally developed for the volume of fluid method and adopted in the phase field multiphase lattice Boltzmann methods by (Connington and Lee, 2013) and has been used for the pseudo–potential multiphase models by Zhang et al. (2018). The geometric model works by dynamically assigning a density to each wall boundary lattice site at each time step depending on the density field in the nearby fluid nodes to satisfy prescribed θ_A and θ_R. The derivation of this model is presented next. The dynamic contact angle θ_d is an emergent property stemming from the statistical mechanical nature of the LBM.

4.7.1 Deriving the Geometric Wetting Model

Consider a droplet spreading on a solid surface with unit normal $\boldsymbol{n}$. The unit normal and unit tangent to the droplet surface are $\boldsymbol{n}_s$ and $\boldsymbol{t}$ respectively. Since the droplet is made of the liquid (heavy) phase submerged in the gas (light) phase, the density gradient at the droplet surface will point in the direction of $-\boldsymbol{n}_s$. Therefore,

$$\boldsymbol{n}_s = -\frac{\boldsymbol{\nabla}\rho}{|\boldsymbol{\nabla}\rho|}. \tag{4.24}$$

Looking at figure 4.2, an expression for θ is derived,

$$\tan\left(\frac{\pi}{2} - \theta\right) = \frac{\boldsymbol{n_s}\cdot\boldsymbol{n}}{|\boldsymbol{n}_s - (\boldsymbol{n}_s\cdot\boldsymbol{n})\boldsymbol{n}|}. \tag{4.25}$$

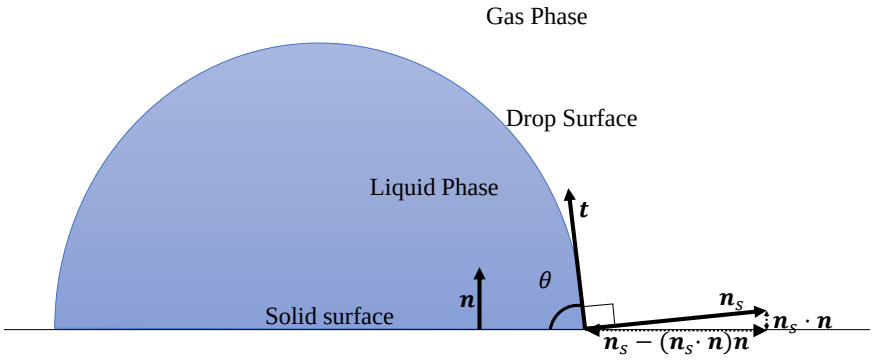

Figure 4.2: Schematic of the geometry at the three–phase contact line where $\boldsymbol{n}$ is the unit normal to the solid surface, $\boldsymbol{n}_s$ and $\boldsymbol{t}$ are the unit normal and unit tangent to the droplet surface. The unit normal to the fluid surface can be calculated using the density field which in turn can be used in geometric arguments to calculate the density on the solid surface to satisfy the contact angle θ.

Substituting equation (4.24) into (4.25) and simplifying,

$$\tan\left(\frac{\pi}{2}-\theta\right)=\frac{-\boldsymbol{\nabla}\rho\cdot\boldsymbol{n}}{|\boldsymbol{\nabla}\rho-(\boldsymbol{\nabla}\rho\cdot\boldsymbol{n})\boldsymbol{n}|}. \tag{4.26}$$

4.7.2 Discrete Geometric Model

Equation (4.26) can be discretised and used to calculate a density to assign to the solid wall locally to satisfy a given contact angle. The discrete form for our geometry is detailed here. Equation (4.26) was discretised differently for the various parts of the geometry depending on the local normal $\boldsymbol{n}$. The geometry is illustrated through a cross–section seen in figure 4.3, with the various geometry types numbered. Similar boundary conditions are labelled with similar patterns. The fluid domains are surrounded by ghost nodes whose density is calculated to satisfy a pre–determined contact angle. The density at these ghost nodes of type 1 can be calculated using the equation (4.26), giving

$$\rho_{ijk}=\rho_{ij+2k}+\tan\left(\frac{\pi}{2}-\theta\right)\zeta, \tag{4.27}$$

where,

$$\zeta = \sqrt{(\rho_{i+1jk} - \rho_{i-1jk})^2 + (\rho_{ijk+1} - \rho_{ijk-1})^2}. \tag{4.28}$$

A similar form can be used for node types 2,3, and 4. For corner 7,

$$\rho_{ijk} = \rho_{i+2j+2k} + \tan\left(\frac{\pi}{2} - \theta\right)\zeta, \tag{4.29}$$

where,

$$\zeta = \sqrt{(\rho_{i+1j+3k} - \rho_{i+3j+1k})^2 + 2(\rho_{i+2j+2k+1} - \rho_{i+2j+2k-1})^2}. \tag{4.30}$$

A similar form is used for all other corners. Equations (4.29) and (4.30) cannot be used for solid nodes directly adjacent to corner nodes because a solid node might be used to update another solid node. Instead, a second order accurate forward difference scheme is used for node type 11,

$$\rho_{ijk} = \rho_{ij-2k} + \tan\left(\frac{\pi}{2} - \theta\right)\zeta, \tag{4.31}$$

where,

$$\zeta = \sqrt{(-\rho_{i+3j-1k} + 4\rho_{i+2j-1k})^2 - 3(\rho_{i+1j-1k+1} - \rho_{ij-1k-1})^2}. \tag{4.32}$$

A similar form was used for all solid nodes neighbouring a corner.

4.7.3 Contact Angle Hysteresis CAH

Contact angle hysteresis was implemented by calculating the local contact angle using the inverse of equation (4.26). If the value of the local contact angle is lower than the receding contact angle (θ_R) then θ is replaced with θ_R and similarly, if the local contact angle is higher than the advancing contact angle, it is replaced with θ_A. Assigning the density on the wall controls the interaction pseudo–potential in

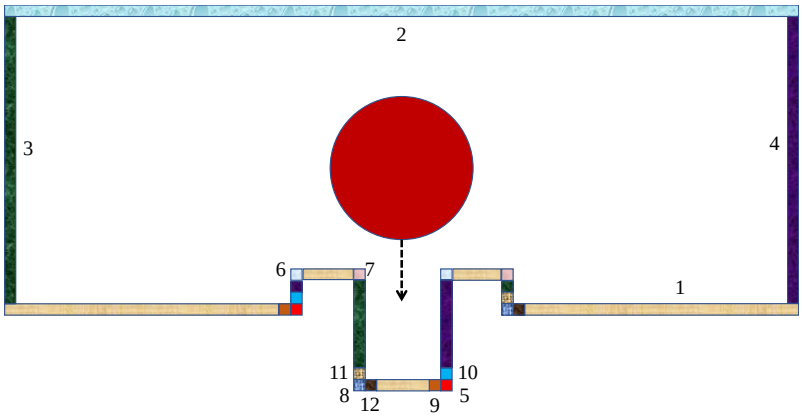

Figure 4.3: The fluid domain is surrounded by adjacent ghost lattice nodes to apply the boundary conditions.

equation (4.14) to satisfy the contact angle θ. In order to capture CAH, the wall lattice sites are initialised with θ in equation (4.26) set to θ_A. This allows the droplet to spread provided that the contact line forms a local contact angle of $\theta \geq \theta_A$. Once a lattice site has been wetted, the value of θ in equation (4.26) is replaced with θ_R for this lattice site. This will stop the droplet from dewetting or the contact line to recede unless the local contact angle at contact line is $\theta \leq \theta_R$. This is implemented by rearranging equation (4.26) for θ and calculating in every time step locally in every wall lattice site. Note that the values of θ assigned at the wall are used to control the interaction force, while the contact line can have any contact angle. The Shan and Chen (1993) model with these additions can capture a range of contact angles, contact angle hysteresis, coalescence and breakup, and contact line dynamics at high density ratio up to 10^3. The simulation is stable for $45° \leq \theta_A \leq 140°$ in the smooth surface case and $55° \leq \theta_A \leq 130°$ in the case with the scratch.

4.8 Validation

4.8.1 Validation of Simulations with Experiments

For the impact of a single droplet falling onto a smooth solid surface we compare our simulations to experimental data from Lim et al. (2009), who examined droplets with in–flight diameter $D_0 = 48.1\,\mu\text{m}$ hitting a smooth surface at speed $u = 1.9\,\text{m}\,\text{s}^{-1}$ corresponding to a Reynolds number $Re = uD_0/\nu = 107$, Weber number $We = \rho u^2 D_0/\gamma = 2.4$, and Ohnesorge number $Oh = \sqrt{We}/Re = 0.015$, where γ is the surface tension. The advancing and receding contact angles were reported to be $\theta_A = 60°$ and $\theta_R = 40°$ respectively. The normalised spreading diameter of the droplet D_s/D_0 and height H_s/D_0 were tracked over time. (Lim et al., 2009) data are compared with equivalent simulations in figure 4.4. To give an indication of the sensitivity of the simulations to the resolution of the lattice, several different lattices were tested, with the resolution expressed in terms of the number of nodes per initial droplet radius. Note that in the lattice Boltzmann method, testing the sensitivity to lattice resolution is not as straightforward as for direct discretisations of the Navier–Stokes equations, since the lattice discretises both coordinate space and the molecular velocity space. Hence modifications of the lattice node spacing require adjustments of other parameters to ensure that the same physical system is being simulated.

In general terms, good agreement is achieved between the simulations and both sets of experimental data as the lattice resolution increases; oscillations in height agree well particularly for the first few periods, while the spreading rate and final diameter are close, with some small variation in experimental data due to experimental noise. There is still some sensitivity in the time scales of the simulations using different lattices, which becomes more evident at later times, but the same equilibrium state is reached in each case. In the non–axisymmetric simulations pre-

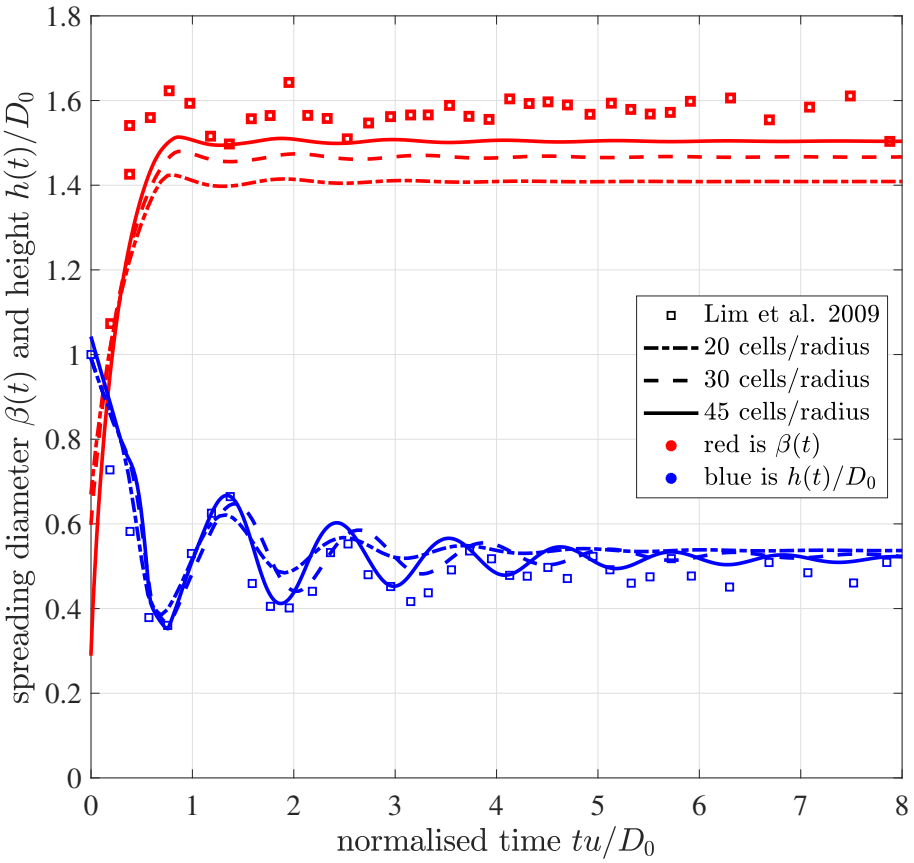

Figure 4.4: Comparison between the experimental results by Lim et al. (2009) and corresponding simulations of a 48.1 µm droplet impacting a flat surface at 1.9 m s^{-1} ($Re = 107$; $We = 2.4$) using different lattice resolutions. The data show the spreading diameter (in red) and height (in blue) of the droplet, all scaled by the initial droplet diameter.

sented in section 5.2, the finest resolution was used and, for a random sample of the conditions considered, simulations were repeated with the other lattice resolutions. The same equilibrium shapes were obtained with each lattice.

4.8.2 Comparison with Analytical Models

Models for the equilibrium spreading diameter of a droplet impacting a surface without contact angle hysteresis have been proposed, see section 2.1.2 for more detail. One such model is that by Van Dam and Le Clerc (2004) given by equation (2.3) which we rewrite here for convenience,

$$\beta_{eq} = 2\left(\tan\frac{\theta}{2}\left(3+\tan^2\frac{\theta}{2}\right)\right)^{-1/3}. \tag{4.33}$$

We use (4.33) this model as well as models of maximum spreading diameters in table 2.1 here for validation.

As validation for the simulation methodology, and to provide a baseline simulation for more complex topographies, a typical inkjet droplet impacting a smooth surface was simulated. The droplet was 48.8 µm in diameter falling at $3.74\,\mathrm{m\,s^{-1}}$, with density $1000\,\mathrm{kg\,m^{-3}}$, surface tension $26\,\mathrm{N\,m^{-1}}$, and dynamic viscosity $9\times10^{-4}\,\mathrm{Pa\,s}$ (i.e. $Re = 204$ and $We = 26$). Several simulations were run without contact angle hysteresis for various θ and using different lattice resolutions. The resulting equilibrium diameters are compared to values predicted by equation (4.33) in figure 4.5, which shows very good convergence of the numerical simulations to the analytical result.

Figure 4.5 shows the maximum spreading diameter of a droplet (scaled by its initial diameter) obtained from numerical simulations with contact angle hysteresis included ($\theta_A = 75°$; $\theta_R = 1°$) for different values of the Weber number. For comparison, the grey shaded area represents the range of maximum spreading diam-

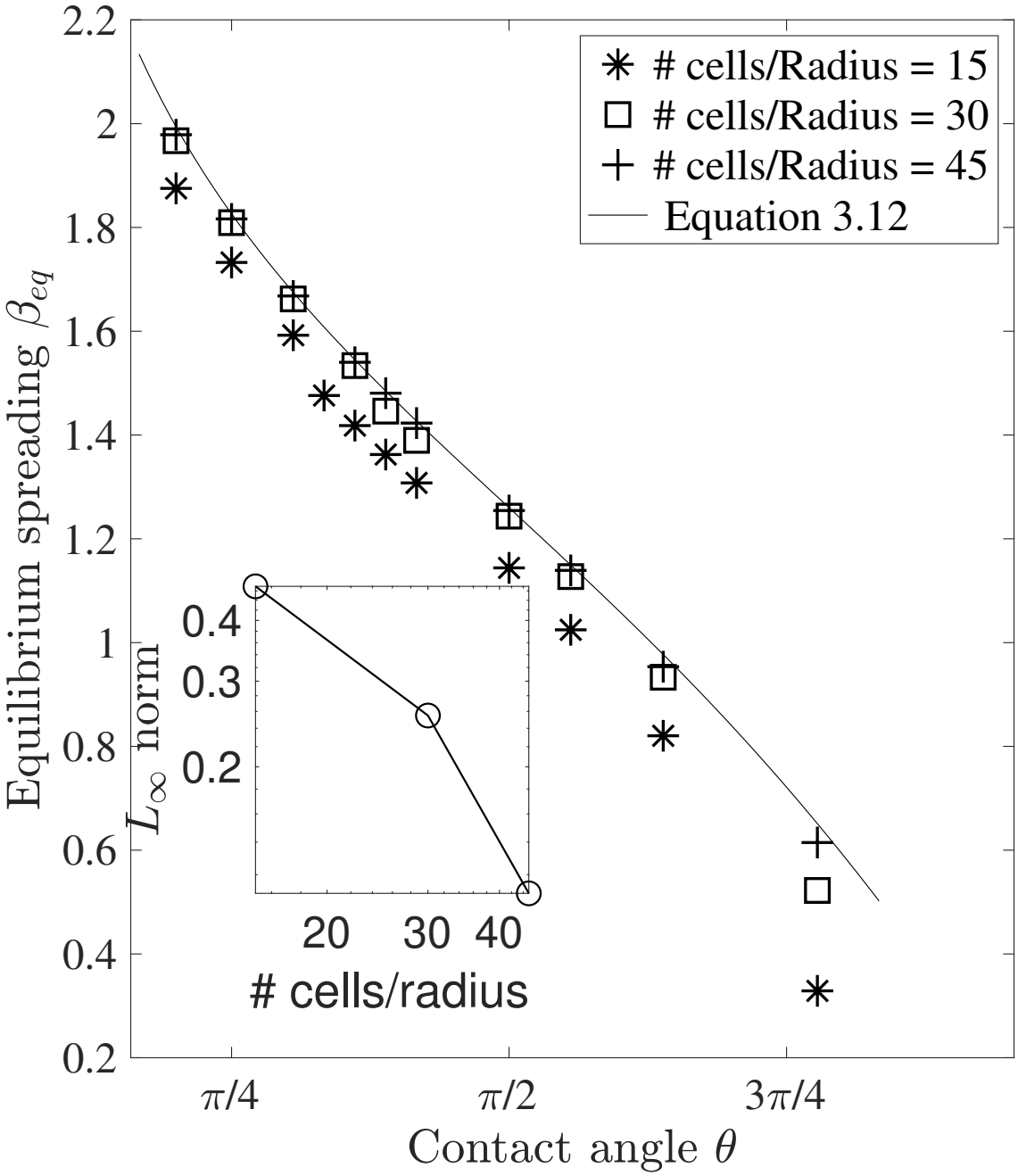

Figure 4.5: Comparison of simulation predictions with analytical models for droplet spreading diameters on a flat surface. The equilibrium diameter is determined without contact angle hysteresis using different lattice resolutions and compared with equation (4.33) for different contact angles. The inset plot shows the L_∞–norm of the error.

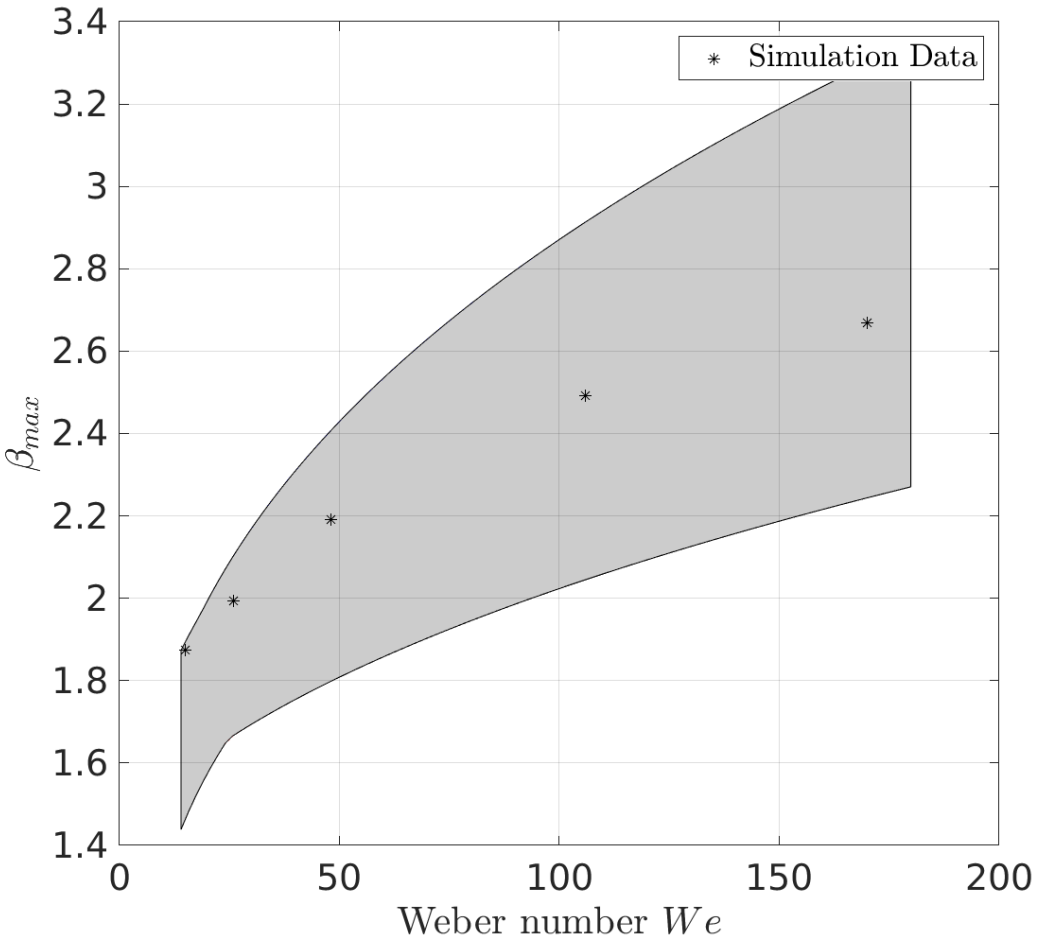

Figure 4.6: The maximum spreading diameter, normalised by D_0, from simulations using the finest lattice is shown for different Weber numbers, with $\theta_A = 75°$ and $\theta_R = 1°$. The grey shaded region indicates the range of predictions using the models in table 2.1.

eters predicted by the spreading models in table 2.1, showing that the simulations are consistent with the collective predicted behaviour. Note that not all the models are valid for the whole range of We shown. Further comparison with the models in table 2.1 is given in figure 4.7 for the specific case $We = 26$. The figure highlights the effect of contact angle hysteresis on the spreading. With hysteresis accounted for (again with $\theta_A = 75°$ and $\theta_R = 1°$), the contact line expands as the droplet spreads and becomes pinned essentially at the maximum spread diameter since the receding contact angle is so low. Such pinning is important in printing applications and is seen in practice with the colloidal inks used in the printed electronics industry (Duineveld, 2003). The grey shaded band again corresponds to the predictions of maximum spreading diameter from the models in table 2.1. In contrast, when contact angle hysteresis is not included in the simulation, the droplet recoils and contracts after reaching its maximum extent, then overshoots and oscillates in diameter as it settles to an equilibrium diameter consistent with equation (4.33).

4.9 Simulation Acceleration

Several methods can speed up the execution of an LBM code. These include using optimisations during compilation, section 4.9.1, optimising memory array access management, section 4.9.2, and running the code on a GPU, section 4.9.3. There are other options for speeding up LBM simulations including OpenMP and MPI parallelisations but are not considered here because the aforementioned methods were found sufficient. To measure improvements in runtime, a unit of measurement is needed. LBM simulations speed is conventionally measured in million lattice updates per second (MLUPS) which is calculated by multiplying the domain size by the number of time steps and dividing by the total runtime.

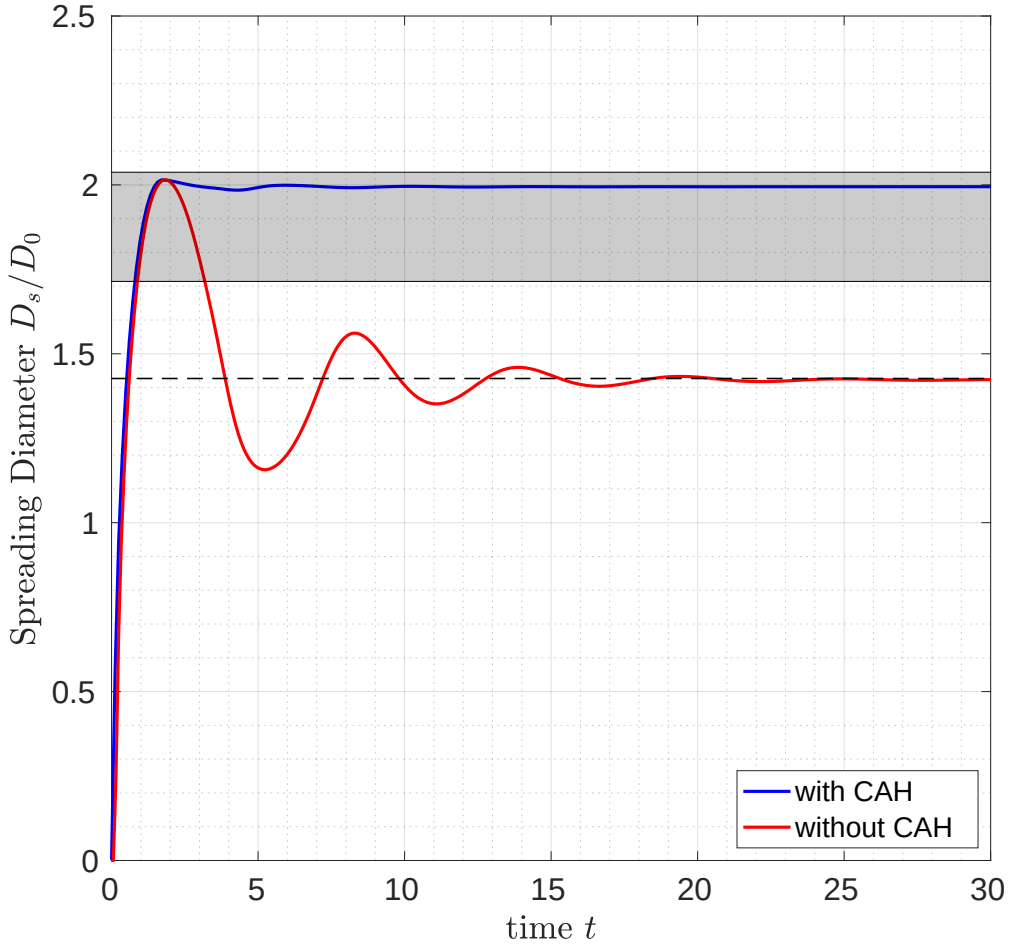

Figure 4.7: The spreading diameter D_s as a function of time for a single droplet on a smooth surface. These are results from simulations with and without contact angle hysteresis compared to predictions of the maximum spread diameter from the models in table 2.1 (grey shaded area) and the equilibrium diameter given by equation (4.33) (grey dashed line).

4.9.1 Compilation Optimisation

Having used the compiled language C++, compile–time optimisation lends itself to accelerate the simulations. The GNU compiler collection (gcc) offers five compilation optimisation options that can be accessed when compiling the code using the command:

```
$ gcc -On code.cpp -o run.exe
```

, where n can be replaced by the five options: 0, 1, 2, 3 or fast. The default value in gcc is 1, and 0 is the option without optimisation. These work by optimising the execution of instructions as well as their order. Running 2D simulations of a stationary droplet with periodic boundary conditions on an Intel Xeon Gold 6138 @ 2GHz, the different optimisation options are compared in figure 4.8.

For small domain sizes, all optimisation options are significantly faster than no optimisations, see figure 4.8. The fast option is the quickest with a simulation speed of 10.59 MLUPS for a domain size $nx = ny = 32$ compared to a speed of 2.59 MLUPS for the same domain size. The optimisation options 2 and 3 are very similar and follow a similar trend, see figure 4.8. As the domain size increases, however, the simulation speeds converge to a relatively low speed of about 0.51 – 0.76 MLUPS. This indicates that optimisation using compilation options is not effective for larger domain sizes. Another option is the management of array storage in memory discussed next.

4.9.2 Array Memory Access

Optimising the memory access pattern to exploit cache memory is said to increase simulation speeds significantly (Krüger et al., 2016). This can be achieved by converting the `(x,y,d)` arrays in 2–D or `(x,y,z,d)` arrays in 3–D into 1-D arrays. One way to linearise the arrays for a 2–D code is to to map a location `(x,y,d)` to

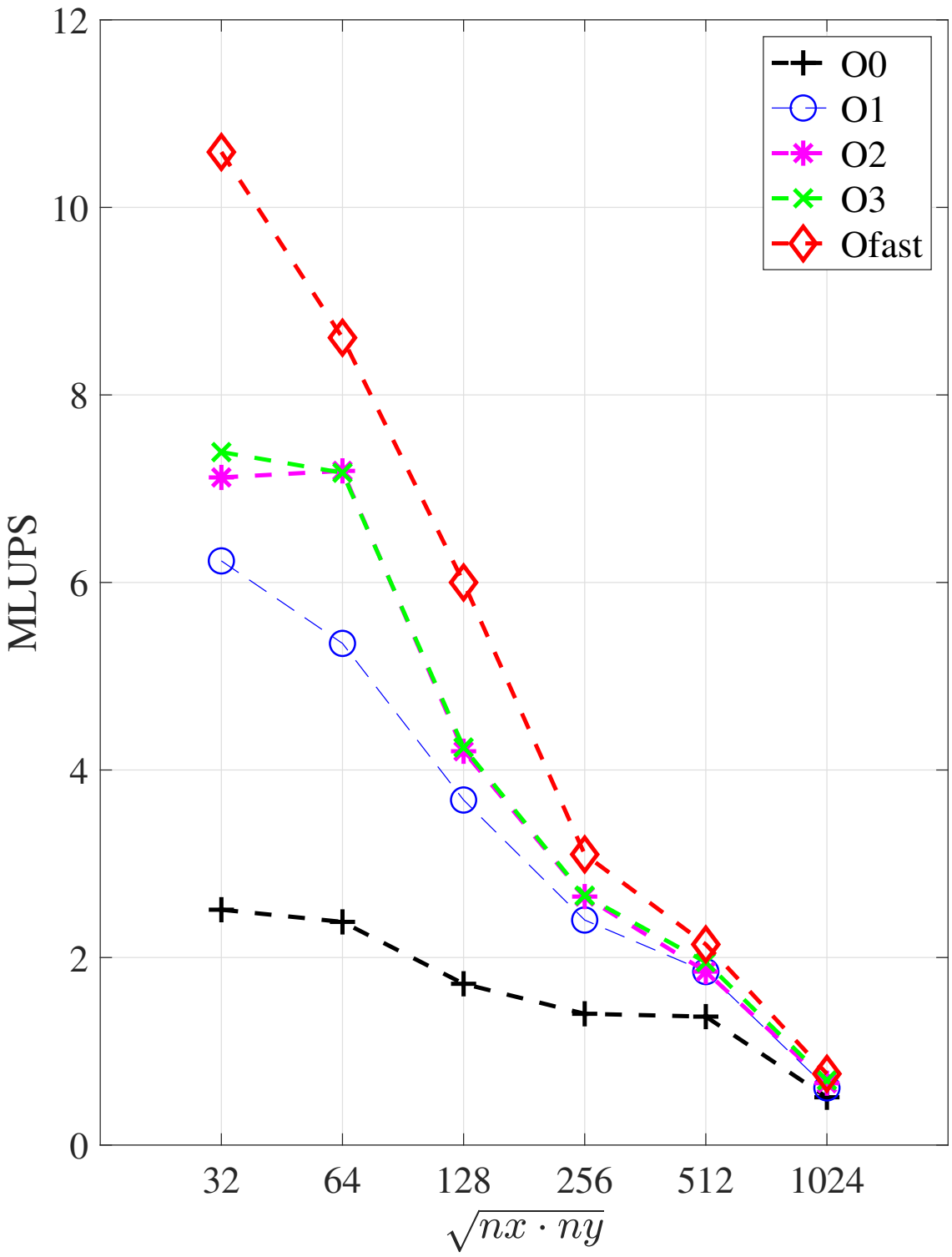

Figure 4.8: Simulation speeds for the five compile optimisation options vs domain size.

`(ndir-1)*(nx*y+x)+(d-1)` in a one dimensional array, where `ndir` is the number of velocity directions. This form facilitates the writing of the arrays to memory by writing array elements in consecutive order. It also facilitates the reading of the information in the 1-D array. The speeding up in reading and writing of arrays decreases run times. To test this, 2-D simulations of a stationary droplet surrounded by periodic boundary conditions are performed with the linearised arrays for various domain sizes. The results are plotted in figures 4.9 and 4.10. In the latter figure, the results for the multidimensional arrays are labelled Multi–dim and the 1–D arrays are labelled Linearised.

For large domain sizes, the linearised arrays simulations perform quicker than their multidimensional arrays counterparts. For example, for a domain size $nx = ny = 1024$, the linearised simulation speed is 3.88 MLUPS while that of the multidimensional array simulation is 0.76 MLUPS for the same size both using the fast optimisation during compilation. The opposite is true for small domain sizes. For example, for the domain size $nx = ny = 32$, the simulation speeds for the multidimensional and linearised array simulations are 10.59 and 5.28 MLUPS respectively. In addition, the linearised arrays simulations scale better and the speeds do not dramatically decrease with increasing domain size, unlike in multidimensional array simulations see figure 4.10. The optimisation options make a significant improvement in speed for both large and small domain sizes in the linearised case, see figure 4.9. These still do not permit large parametric studies required in this thesis, hence acceleration using GPUs is discussed next.

4.9.3 GPU Acceleration

Graphics Processing Units (GPUs) were originally developed to render graphics for computer screens but they are now found in workstations and high–performance computing facilities where they are used for other applications, including fluid simulations particularly using LBM and smooth particle hydrodynamics. Both in 2–D

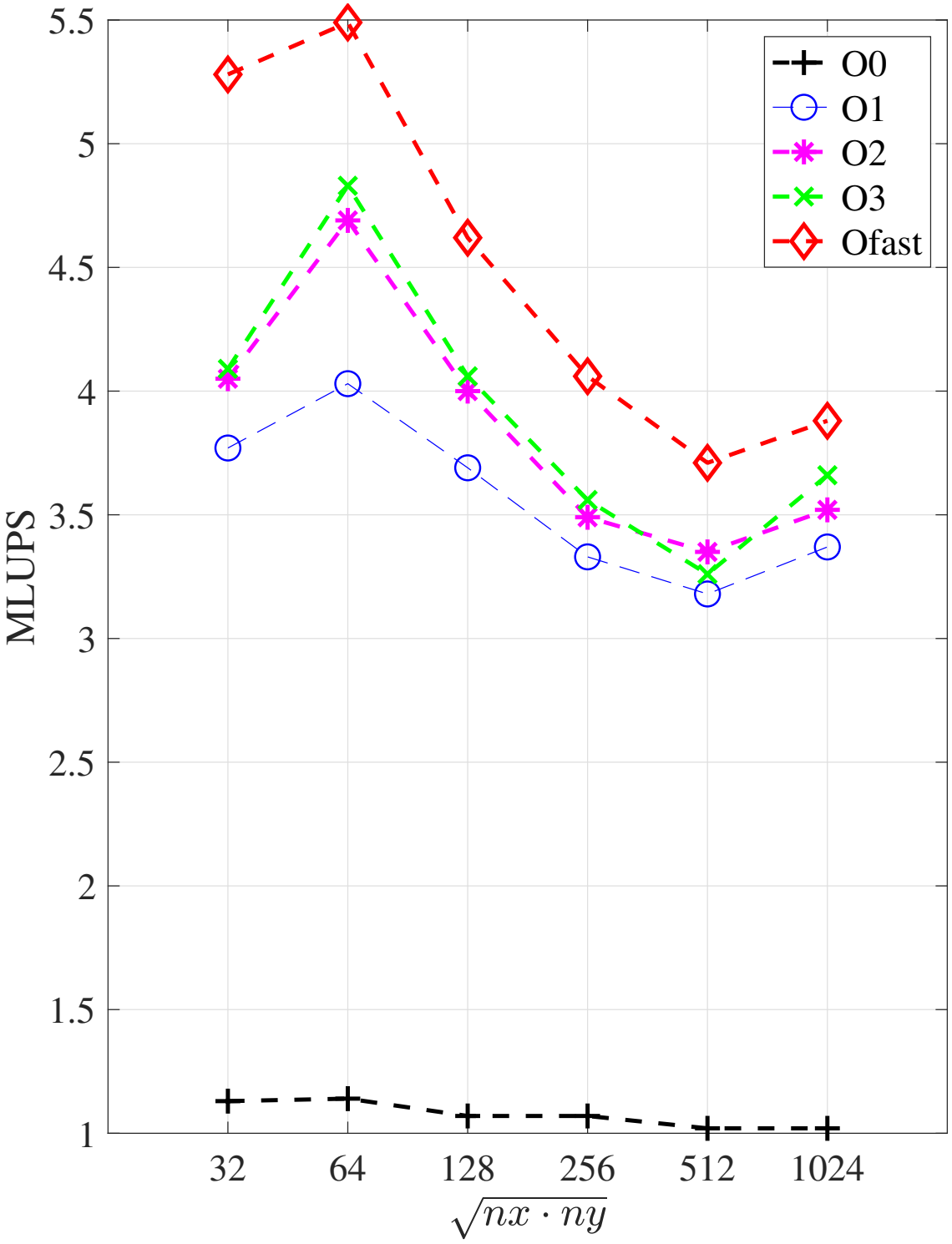

Figure 4.9: Simulation speeds using the various optimisation strategies and linearised array arrangements.

and 3–D graphics, similar and usually simple, computations are repeatedly performed on different input data, this lends these computations for parallel computation.

GPUs were designed to perform such simple but numerous computations in parallel. GPUs exploit the fact that the same operations are repeated, a bigger fraction of the transistors is dedicated to computation in a GPU than in a CPU. CPUs, on the other hand, use more transistors for caches and logical control and treats all input sequentially making it more suitable for complex non–repeating computations.

To exploit the efficiency of GPUs in processing repeated computations in parallel, software engineers map and design non–graphic algorithms to run on GPUs. Modern GPUs, compared to their older counterparts, are more precise, support double floating–point arithmetic and are designed to support scientific computation.

There are two major GPU vendors: NVIDIA and AMD. I will use NVIDIA's computing platform because the GPU devices in the University of Leeds are from this vendor and limit the subsequent discussion accordingly. To run programs on NVIDIA GPUs, they have to be written in the Compute Unified Device Architecture (CUDA) programming language supported by the vendor. The GPUs available at the University of Leeds supercomputer facility ARC3, at the time of performing simulations for this thesis, are NVIDIA K80, P100. The latter will be used for the simulations in this thesis because they have greater memory. The P100 and has a memory of approximately 11GB.

Each GPU has a CPU multiprocessor called the Host which is used to manage the threads of the GPU. The Host provides each thread with the code it has to run when it needs it. Threads are grouped in units called warps typically consisting of 32 threads each. All threads in a warp execute their command concurrently. GPUs perform most efficiently when an algorithm can be divided among

numerous threads. To exploit the parallel nature of GPUs, algorithms should be arranged such that threads follow the same computation paths.

The threads of a GPU are arranged in a hierarchy of three levels: the first is threads which are arranged into *blocks* which are in turn arranged into a *grid*. Each thread is identified by its number in the block and its block's number in the grid. Data is usually arranged such that their dimensions match those of the threads, this is true for LBM where each thread is responsible for one lattice site.

A qualifier called `__global__` defines functions, without a return value, called *kernels* which the threads then perform. The instructions within these kernels are executed in every thread representing a loop executed *in parallel*. To identify the portion of data for a particular thread, the variables `threadIdx` which is the position of the thread within a block, `blockIdx` which is the position of the block within the grid, `blockDim` provides the dimensions of the block, and `gridDim` which provides the dimensions of the grid are needed.

Simulation domain sizes are usually bigger than a single block, the data set is spread across several blocks. To map between GPU thread coordinates to spacial 2D/3D coordinates, a code like that in listing 1 is used.

```
# in 2D
unsigned int j = blockIdx.y;
unsigned int i = blockIdx.x*blockDim.x+threadIdx.x;

# in 3D
unsigned int k = blockIdx.z;
unsigned int j = blockIdx.y;
unsigned int i = blockIdx.x*blockDim.x+threadIdx.x;
```

Listing 1: Converting GPU coordinates to special coordinates.

A kernel is called using the triple angle bracket command:

```
kernel_name<<<grid, threads, mem>>>(arg1,arg2,arg3,...)
```

```
#, where grid: is grid dimensions,
#, threads: is block dimensions.
#and mem: is shared memory set to 0 when missing.
```

CUDA also uses qualifiers for functions that run on a CPU or GPU: `__host__`, and `__device__` respectively. If a function has not a qualifier, it is compiled to run on the host. These qualifiers can be combined for a kernel to run on both host and device as `__host__ __device__`.

To implement the LBM multiphase methodology, the pseudocode in listing 2 was used. Firstly the variables are given a type and allocated memory on the device using `cudamalloc` and on the host using `malloc`. The droplet and the surrounding vapour are initialised including density, location, radius, and velocity. The distribution function is then initialised to the equilibrium distribution function values. Boundary values are then set using equation (4.27) for the wall to be impacted and similarly for the rest of the walls but with a neutral contact angle of $\theta = 90°$.

The collision step, using the MRT model and force modifications discussed earlier in this chapter, is then called upon with a kernel that runs on the device (GPU) followed by the streaming step. Bounce back is then applied on the solid walls followed by calculating the macroscopic quantities. Having calculated the density, the geometric boundary condition in equation (4.17) can be applied to assign densities to lattice cites on the impact wall. The thermodynamic pressure using the EOS and the pseudopotential are then calculated, see listing 2.

The code can be compiled using the `nvcc` command, see listing 3. The option `-arch sm_70` is the compute capability of the Nvidia Tesla P100 used in this thesis. The `--ptxas-options=-v` requires verbose output during compilation. `-O3` is the optimisation option as discussed in section 4.9.1.

```
// setup the GPU device and give it Id 0
cudaSetDevice(0)
int deviceId = 0;
cudaGetDevice(&deviceId)

// define domain size, and timestep (nx,ny,numTimSteps)

/* define fluid and flow properties(densities,
 relaxation times, speed, etc)*/

// start main
int main(int argc, char const *argv[]) {
  for(t=0; t<=NumSteps; t++){
    //allocate memory for all arrays using malloc and cudamalloc

    // kernel: intialise droplet's density, speed, radius, ...

    // kernel: initialise distribution function field eq 3.8

    // kernel: initialise boundaries

    // kernel: collision equations 4.12, 4.13, 4.22, 4.23

    // kernel: streaming equation 3.16

    // kernel: bounceback for solid boundaries

    // kernel: calculates macroscopic properties equation 3.10
    // and 4.17 with A =0.5

    // kernel: Geometric Wetting Boundary condition equation 4.27

    // kernel: calculate multiphase potential equation 4.14 and 4.15

    // print output for post processing in vtk format

    // free memory using free() and cudafree()

    // release resources associated with the GPU device
  }
  cudaDeviceReset();
  return 0;
}
```

Listing 2: Pseudocode for the LBM multiphase GPU used in this thesis written in CUDA C.

```
$ nvcc -arch sm_60 -v --ptxas-options=-v  ...
  -O3 LiModel3DMain.cu seconds.cpp -o run.exe
```

Listing 3: Command for compiling CUDA C code for the Nvidia Tesla P100.

To test the speed improvement by the GPU implementation, 2D simulations of a stationary droplet in domains of increasing size were performed and run on the Tesla P100 GPU. Compared to the CPU implementations, we can notice a speedup of up to two orders of magnitude, see figure 4.10 where the 2D GPU simulations are labelled GPU–2D. For example, for a domain size $nx = ny = 1024$, the simulation speeds for the linearised array CPU simulation and the corresponding the GPU–2D are 3.66 and 614.03 MLUPS respectively showing great improvement. The simulation speed for the 2D GPU implementation increases with increasing domain size but plateaus at approximately 600 MLUPS. A corresponding 3D code was implemented, see figure 4.10 where 3D results are labelled GPU-3D. Simulation speeds plateaued around 200 MLUPS on the Tesla P100 GPU. This speed enables parametric studies of the kind required for this thesis. A simulation that would take up to 3 days (of size 256×256×576 lattice nodes) on a single CPU then ran in under two hours.

4.10 Summary

Here, the options to mitigate issues of density ratio and surface tension of the pseudo-potential model were discussed. The improvement recommended by Li et al. (2012; 2013; 2019) were found most appropriate for this thesis. The model with these modifications was then validated against literature–reported data as well as analytical predictions. After validating the model, it was accelerated using GPU–CUDA. With a valid and efficient approach, parametric studies of inkjet printing can now be executed in the next chapter.

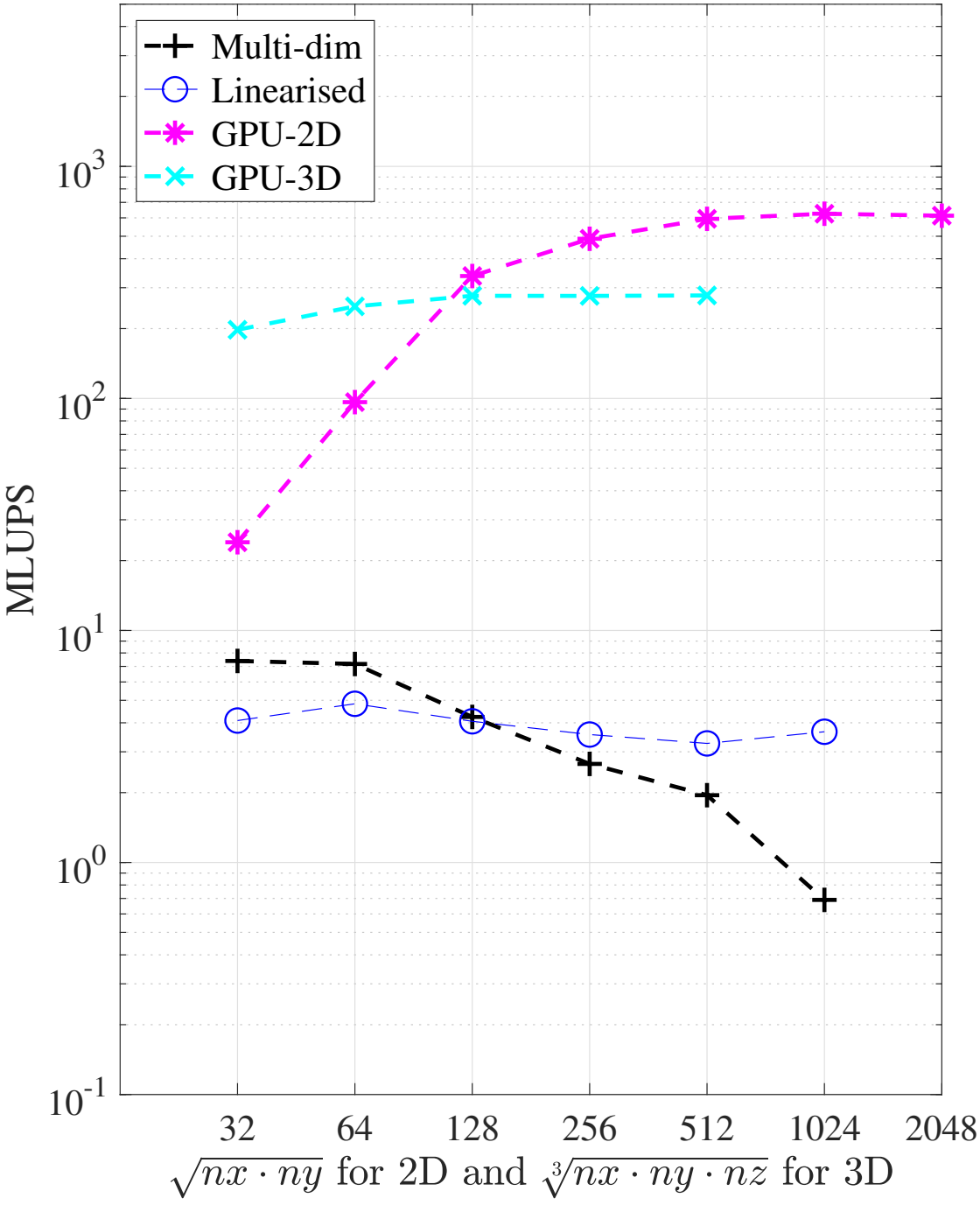

Figure 4.10: GPU acceleration results with in 2D (GPU–2D) and 3D (GPU–3D). For comparison, corresponding simulation speeds on a CPU with multidimensional and linearised arrays are also plotted labelled Multi–dim and Linearised respectively.

Chapter 5 | Printing onto an Idealised Scratch

Contents

Having developed validated and accelerated the simulations, this chapter investigates a droplet impacting onto a surface containing a linear topographic feature. We use an idealised geometry, explained in section 5.1, which mimics a scratch or an intentionally–manufactured groove to control droplet spreading. We consider how the spread of the droplet is affected by the geometry of the feature, the advancing and receding contact angles, and the droplet parameters as characterised by Re and $Oh = \sqrt{We}/Re$. These two dimensionless numbers capture the main flow and fluid properties including, viscosity, surface tension, density, speed, and droplet diameter, see equation (2.1). The chemical interaction between the droplet and substrate is captured by the contact angle. The colloidal nature of the droplet results in contact line pinning and very low $\theta_R \approx 0°$. The increased viscosity and reduced surface tension due to the colloidal nature of the typical inkjet inks are captured in the Re and We respectively. Therefore, the results in this thesis are applicable in the inkjet printing parameter space shown in figures 2.1 and 2.3. Before presenting the reults of parametric simulations in section 5.2, we postulate a regime map of possible morphologies and conditions for their occurence. section 5.2 will then test the validity of the postulated regime map using simulations for a typical inkjet Re and Oh. section 5.3 studies the effects of these dimensionless groups as well as θ_A, and θ_R on the regime map. Chapter 6 will discuss the implication of the findings for printing applications.

5.1 Idealised Scratch and Anticipated Dynamics

The specific surface geometry feature considered here is shown in figure 5.1. A scratch on the substrate is idealised as a continuous uniform groove of rectangular cross–section, with a rectangular ridge on each side representing solid material normally displaced during formation of the scratch. Hence the combined cross–sectional area of the side ridges matches that of the groove below the original substrate surface level. The side ridges are taken to have a height of $\frac{1}{2}\bar{d}$, where $\bar{d}$ is the depth

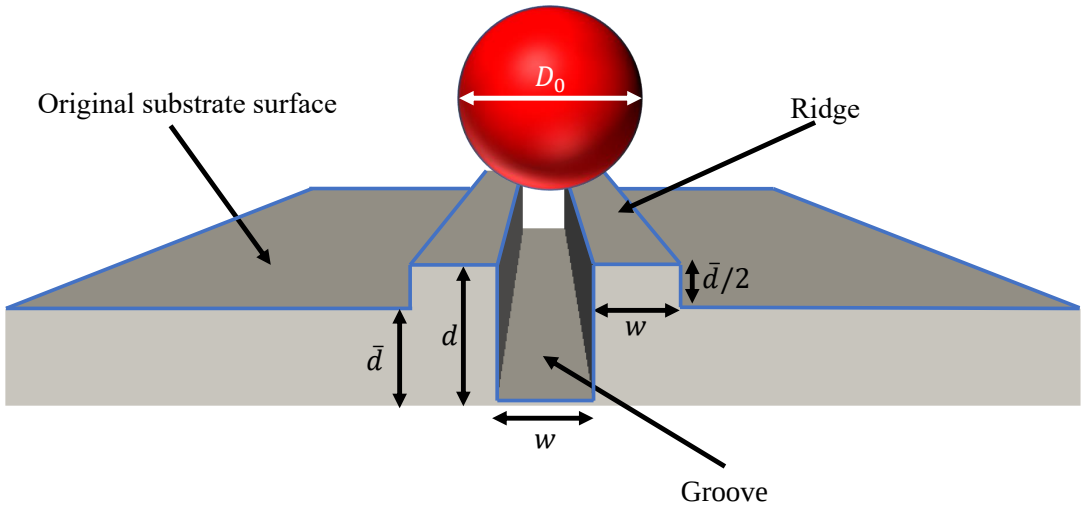

Figure 5.1: The geometry used to represent an idealised scratch. The groove has width w and so do the side ridges. The bottom of the groove is a depth $\bar{d}$ below the original substrate surface, and its total depth from the top of the side ridges is $d = \bar{d} + \frac{1}{2}\bar{d}$.

of the groove below the original surface. Hence the total depth of the groove from the top of the side ridges is $d = \frac{3}{2}\bar{d}$. The displaced material in real scratches is not as symmetric across the scratch nor as uniform along it, but the idealised geometry considered here is a good approximation. As well as representing a scratch, the geometry also mimics micro–structured surfaces such as those studied by Seemann et al. (2005), with the side ridges akin to the edges between two neighbouring grooves. Throughout this study, the groove width, w, and depth, d, are scaled by the in–flight diameter, D_0, of a droplet impacting on the solid surface. We will use the words 'groove' and 'scratch' interchangeably in what follows. Note that in practice scratch sizes can range from nanometers to tens of microns (Brostow et al., 2004; Chen et al., 2008; Dasari et al., 2009).

In considering possible outcomes of a single droplet impact on this topography, there are some obvious limiting behaviours. If the groove is much wider than the droplet, i.e. $w \gg 1$, and the droplet lands away from the side walls, the impact is simply that of a droplet on a flat surface, which has been widely studied (see section 5.1.2). If instead the droplet impacts the side wall, the situation corresponds to impact on a step as previously considered by e.g. Bussmann et al. (1999) and more

recently by Jackson et al. (2019) in the context of droplet deposition into square cavities. As the groove width becomes closer to the droplet diameter, i.e. $w \sim 1$, the dynamics are expected to become more complicated. If the droplet lands in the centre of the groove, full imbibition of the droplet into the groove would be expected, but only for sufficient groove depths and substrate wettability. At the other extreme, if $w \ll 1$ and the scratch is shallow, i.e. $d \ll 1$, it is expected to have a negligible effect on the spreading dynamics of the droplet, and we have again the well–studied scenario of droplet impact on a smooth flat surface. However, if d is sufficiently large compared to width, one would expect capillary flow to occur along the narrow channel if the substrate is sufficiently wetting, i.e. $\theta < 90°$.

In this chapter we therefore focus on the range $0 < w \leqslant 1$, i.e. where the droplet is of a similar size or larger than the scratch. The droplet impact regime is taken to be non–splashing, non–bouncing deposition as required for a successful inkjet printing operation, i.e. within the inkjet printing parameter space see section 2.1.1. It is also important to note that the advancing static contact angle is assumed to be less than 90° and the receding contact angle to be close to zero, again as is typical in printing systems. In all cases, the droplet initially spreads on impact due to inertia. Given the presence of ridges and edges in the geometry, it is expected that overspill, splitting and/or pinning of the droplet contact line on different edges will occur for certain conditions. A postulated regime map showing outcomes of single–droplet deposition on the centre of the scratch for different widths and depths is given in figure 5.2. The different droplet morphologies and estimates of the conditions under which they occur are explored and developed in the following subsections.

5.1.1 Capillary Flow Along Narrow Scratches

A scratch much narrower than the impinging droplet ($w \ll 1$) is expected to have little effect on the early stage inertial spreading of the droplet. However, once deposited, the drop becomes a source of liquid from which capillary flow can occur

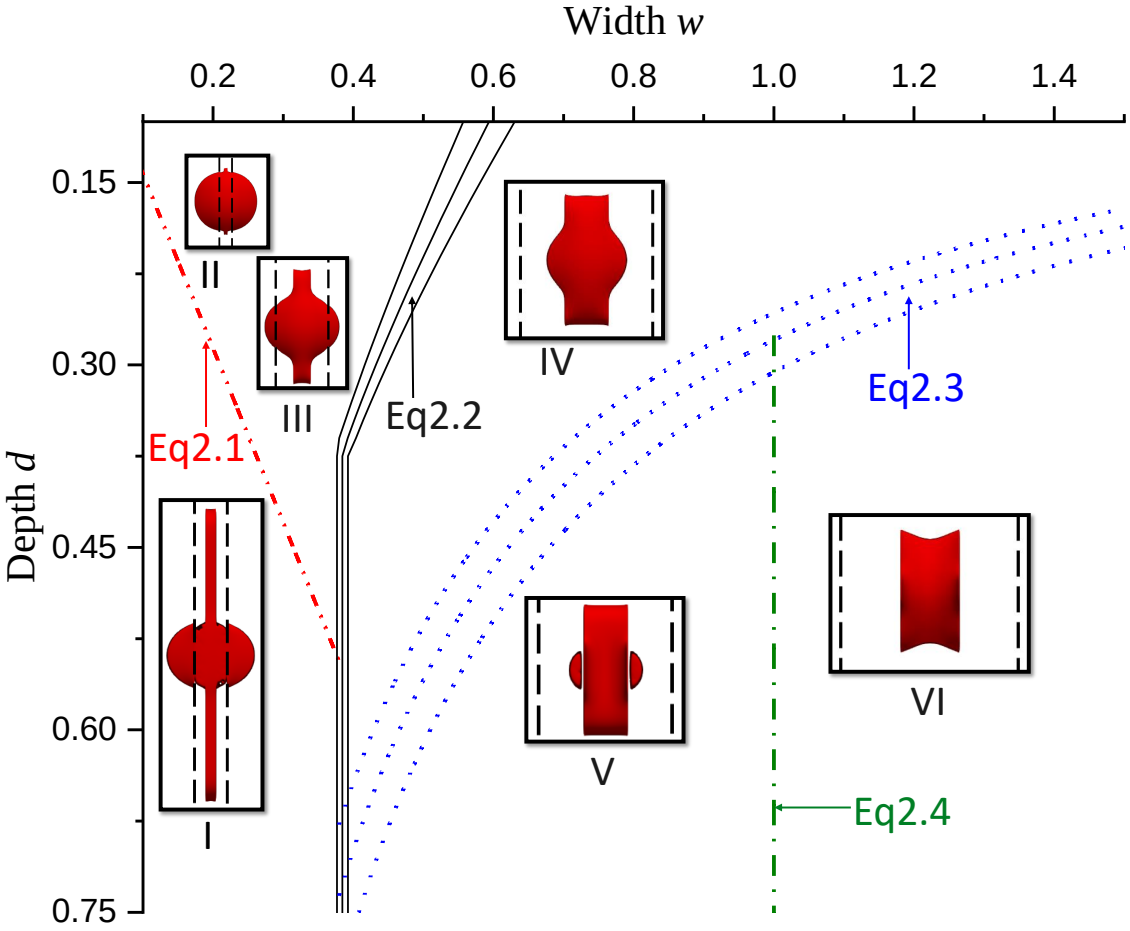

Figure 5.2: A postulated regime map for the outcome of a single droplet impact centred on the idealised scratch shown in figure 5.1 in terms of the scratch width and depth scaled by the droplet's in–flight diameter. The lines and curves indicate theoretically estimated critical conditions for behaviours including capillary flow, contact line pinning on edges, droplet splitting and full imbibition into the scratch. The inset top–view images within each region show examples of corresponding final printed droplet shapes predicted by numerical simulations, indicating possible different droplet morphologies. These are named: I 'capillary'; II 'quasi–spherical cap'; III 'inertial'; IV 'semi–imbibed'; V 'split semi–imbibed'; and VI 'fully–imbibed'. Note that the inset images are shown at different scales. The vertical dashed lines in each image indicate the outer edges of the side ridges of the scratch.

over a longer time scale along sufficiently narrow and deep scratches. Capillary flow has been extensively studied including in cylindrical micro–channels since the early twentieth century (Bell and Cameron, 1906; Lucas, 1918; Washburn, 1921). With the advent of microfluidics, recent attention has been paid to other micro–channel geometries; most relevant to our geometry is the work on open rectangular micro–channels by Yang et al. (2011) who, based on experiments and a model balancing capillary and viscous forces, proposed a critical channel width below which capillary flow occurs:

$$w_{cap} = 2d \cos\theta_A/(1 - \cos\theta_A). \tag{5.1}$$

The line given by (5.1) is shown in figure 5.2, with θ_A having a representative value of 75°. Below this line, the final printed droplet shape will consist of a localised droplet (since the small receding contact angle prevents full contraction of the droplet) with liquid filaments extending in both directions along the scratch. An example numerical simulation result (discussed later) is shown in figure 5.2 as image I. As a result of the mechanism producing it, we label this the 'capillary' morphology. The long filament within the scratch has been observed by Seemann et al. (2005), but not the liquid outside the scratch because they used vapour condensation rather than droplet deposition. Above the line (5.1), i.e. for shallow, narrow scratches, there will be only a small deviation from perfect sphericity, as indicated by image II in figure 5.2. This shape will be referred to as the 'quasi–spherical cap'.

5.1.2 Predicting Edge Pinning and Overspill

The impacting droplet will spread over the top of the side ridges while at the same time penetrating the scratch. Depending upon the width and depth of the scratch, overspill from the side ridges onto the original substrate may occur. To develop an estimate of conditions under which this will happen, we need to consider the expected maximum spreading diameter, D_{max}, of the droplet. A discussion of the available models for D_{max} can be found in section 2.1.3.

Although originally developed for axisymmetric conditions, maximum spreading laws like the those in section 2.1.3 can be modified by introducing a correction factor to account for the presence of the scratch, and hence used to estimate when overspill occurs. For ease of implementation we consider only models that can be written explicitly as $\beta_{max} = f(We, Re)$ or $\beta_{max} = f(We, Re, \theta_A)$. In particular, we use the models of Scheller and Bousfield (1995), Pasandideh-Fard et al. (1996), Roisman (2009), Laan et al. (2014), and Lee et al. (2016) listed in table 2.1.

Assuming that the droplet spreads on the tops of the side ridges and the inner scratch walls at the same rate, a correction factor can be derived by subtracting from the initial droplet volume the volume of liquid that will go into the scratch before the droplet reaches the outer edges. The new volume available for spreading can then be used to derive a new equivalent 'initial' droplet diameter to be used in the maximum spreading laws. Assuming that $d \leq w$, the volume to be subtracted is approximately $dD_0 \times wD_0 \times D_0 = wdD_0^3$, so the new volume of liquid available for spreading over the side ridges is $V_{new} = {}^{\pi D_0^3}/_6 - dwD_0^3 = D_0^3\,({}^{\pi}/_6 - dw)$. This is equivalent to a free droplet of diameter $D_{0,new} = D_0\,(1 - {}^{6dw}/_{\pi})^{1/3}$. The maximum spreading laws are of the form ${}^{D_{max}}/_{D_0} = f(Re, We, \theta_A)$, so replacing D_0 with the expression for $D_{0,new}$, $D_{max}/D_0 = f(Re, We, \theta_A)\,(1 - 6dw/\pi)^{1/3}$. This holds when $d \leq w$, otherwise the droplet reaches the outer edges of the side ridges before the entire depth is covered by the impacting droplet. If $d > w$, the volume to be subtracted will be $w^2D_0^3$ and hence $D_{0,new}$ will not depend on d, and w_{pin} will be the same value as that when $d = w$ for the entire range $d > w$. To spill over onto the original substrate, the droplet needs to spread beyond a distance of $3w$, i.e. the width of the scratch and the two side ridges, hence overspill is expected to occur only for scratches with widths smaller than w_{pin}, given by:

$$w < \frac{1}{3} f(We, Re, \theta_A) \begin{cases} \left(1 - \frac{6dw_{pin}}{\pi}\right)^{1/3} & if\ d \leq w_{pin} \\ \left(1 - \frac{6w_{pin}^2}{\pi}\right)^{1/3} & if\ d > w_{pin} \end{cases}. \tag{5.2}$$

The five different spreading model listed in table 2.1 give slightly different predictions for $f(We, Re, \theta_A)$, therefore, in plotting the values of w_{pin} in figure 5.2, the three solid black lines correspond to the mean and standard deviation of the five predictions. Note that equation (5.2) simply provides an estimate of scratch widths for which the droplet can reach the outer edge of the side ridges. Whether or not the droplet does spill over the edge will depend on whether or not it has sufficient inertia to overcome the Gibbs criterion for pinning of the contact line on the edge. Hence equation (5.2) provides an estimate for conditions under which the droplet contact line will pin on the outer edge of the side ridges. This will be discussed again with the benefit of numerical simulations in section 5.2.1. For w sufficiently below w_{pin}, the droplet inertia is expected to be sufficient for overspill onto the original substrate to occur and the final droplet morphology will look like image III in figure 5.2. This will be referred to as the 'inertial' morphology.

5.1.3 Droplet Splitting and Imbibition

For $w > w_{pin}$, the droplet does not cross the outer edges of the side ridges. For sufficiently shallow scratches, its final shape is expected to be one where the continuous liquid volume rests on top of side ridges while also filling the scratch. This morphology is labelled 'semi–imbibed', and an example is shown in image IV in figure 5.2. As the scratch depth increases, more of the liquid volume will occupy the scratch. Given that the low receding contact angle prevents significant contraction of the droplet contact line from the side ridges, for a deep enough scratch the droplet may split along the *inner* edges of the side ridges such that the liquid on the top of the side ridges and that in the scratch become separated. Splitting along the inner edges is expected when the cross–sectional area of the scratch multiplied by D_{along}, the length of spreading along the scratch, results in a greater volume than the droplet. Thus the critical width corresponds to when $wD_0 \times dD_0 \times D_{Along} = \frac{4}{3}\pi(D_0/2)^3$. Assuming that $D_{Along} = \beta_{max} D_0$, where β_{max} is again the maximum spreading on a

flat surface, this gives the following estimate of the critical width for which splitting will occur:

$$w_{split} = \frac{\pi}{6d\beta_{max}}. \tag{5.3}$$

Again the different models in table 2.1 have been used to give a spread of estimates of β_{max} (for $\theta_A = 75°$) and these result in the blue dotted curves in figure 5.2. For depths below these curves and $w < 1$, the final droplet shape will be a 'split semi–imbibed' morphology where most of the liquid occupies the scratch, but separate small droplets remain on the upper surfaces of the side ridges. See the example image V in figure 5.2.

The droplet fully imbibes into the scratch without spreading on the side–ridges when $w \geqslant 1$ and the scratch depth is sufficient to contain the entire the liquid volume. The result is a 'fully–imbibed' morphology as indicated in image VI in figure 5.2. By a similar argument to that above for droplet splitting, the condition for full imbibition into the scratch is:

$$w \geq 1, \quad \text{and} \quad d > \frac{\pi}{6\beta_{max} w_{split}}. \tag{5.4}$$

This corresponds to the region to the right of the vertical dash–dot line in figure 5.2. Having developed a postulated regimes map, figure 5.2, simulations can be used to test its validity.

5.2 Simulate Single Droplet Impact on Scratch

The droplet deposition scenario considered is as described in section 5.1 and shown in figure 5.1 following the methodology in chapter 4. To provide a representative

specific impact condition, simulation results are presented here for $Re = 204$ and $We = 26$, which are relevant to inkjet printing applications (Dong et al., 2007; Zhang et al., 2018) and as indicated in figure 2.1. The advancing and receding contact angles are set to $\theta_A = 75°$ and $\theta_R = 1°$, again to be relevant to inkjet printing (Davis, 1980; Duineveld, 2003). The effect of variations in these four key parameters are considered in section 5.3.

5.2.1 Printed Droplet Morphologies

Figure 5.3 presents a map of the scratch width–depth parameter space showing the outcomes of droplet impact simulations that were run until an equilibrium morphology was formed. Different symbols indicate the morphology obtained at each width–depth combination, and corresponding examples of the equilibrium shapes for the same Re, We, θ_A and θ_R are given in figure 5.2. In addition, figure 5.3 shows an example of an 'edge–pinned' final droplet, where the droplet has spread over the tops of the side ridges, reaching the outer edge with insufficient momentum to spill onto the original substrate surface. The contact line remains pinned on the outer edge as the very low receding contact angle prevents recession and the Gibbs pinning criterion is satisfied. Top views of the morphologies in figure 5.3 are in figure 5.4.

The theoretically estimated regime boundaries developed in section 5.1 are superimposed in figure 5.3 and show generally very good agreement with the outcomes of the numerical simulations. Recall that the three curves corresponding to equations (5.2) and (5.3) give the mean and standard deviations of the predictions based on the maximum spreading models in table 2.1. There is slight deviation between equation (5.1) and the boundary of the capillary regime identified from simulations because equation (5.1) assumes an infinite source of liquid and does not capture the force due to the Laplace pressure resulting from curvature of the droplet, which becomes significant when the source droplet is of commensurate width to the groove. However, the criterion (5.2) for pinning of the contact line on the edges

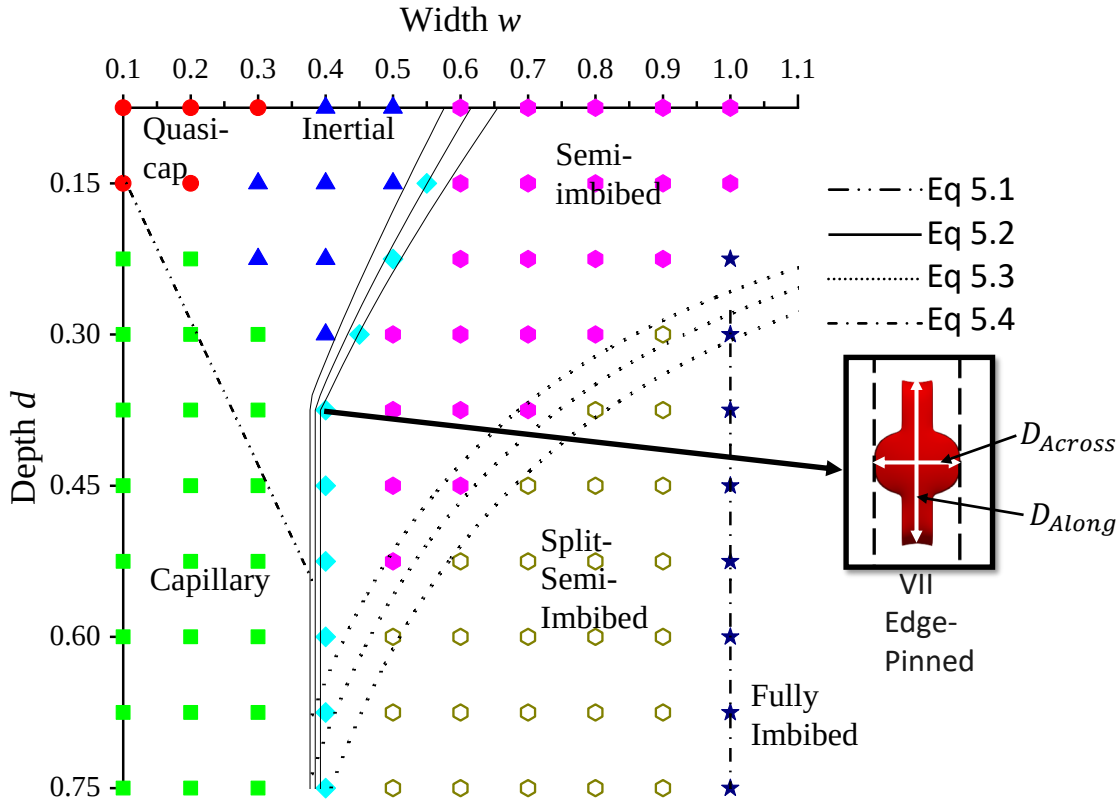

Figure 5.3: Numerically determined regime map for morphologies formed by printing a single centred droplet impact onto the idealised scratch shown in figure 5.1. Simulation parameters: $Re = 204$, $We = 26$, $\theta_A = 75°$, $\theta_R = 1°$. The overlaid lines and curves give the theoretically estimated regime boundaries developed in section 5.1.

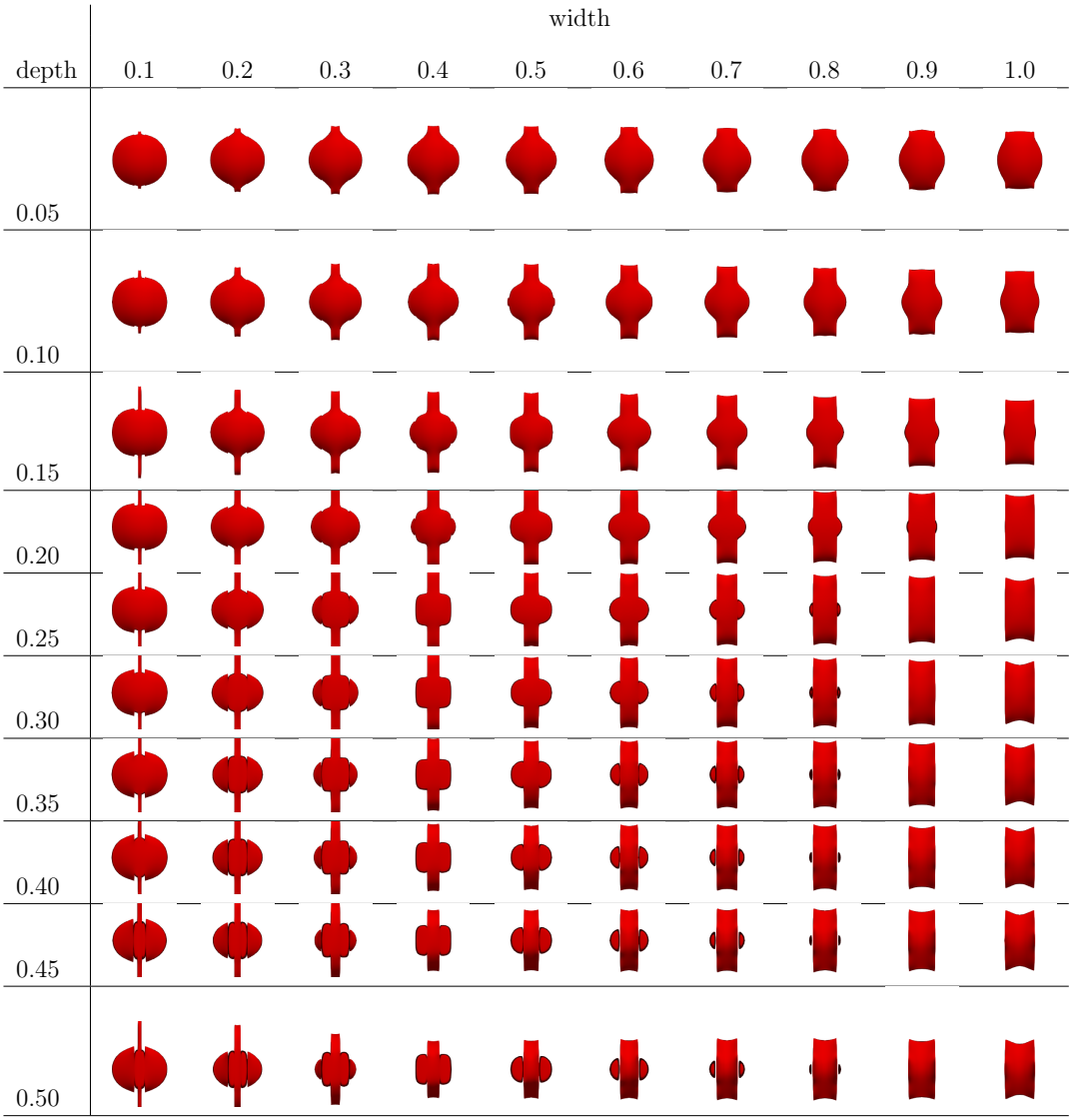

Figure 5.4: Top views of equilibrium morphologies for printing onto a scratch with various widths and depths for $Re = 204$ and $We = 26$. The zoom scale is kept constant.

of the side ridges captures very well the numerical predictions. Note that similar pinning has been observed even on rounded edges (Kant et al., 2017).

The splitting boundary of equation (5.3) also fits well with the simulation results but has a slight deviation at larger depths. This is likely due to the assumption that the entire depth of the scratch is filled when deriving equation (5.3), i.e. the simple geometrical argument does not account for the non–trivial shape of the liquid free–surface within the scratch. Similarly, the conditions for full imbibition of the droplet into the scratch are quite well identified by the criteria in (5.4), with some discrepancy in the critical depth due to the crude approximation of the free–surface shape within the scratch. The delineation of the 'quasi–spherical cap' region of figure 5.3 is somewhat subjective. Here we define this to be where the final droplet shape deviates from a spherical cap by less than 10% in the lateral dimensions.

5.2.2 Droplet Spreading Dynamics

Although seven different equilibrium morphologies have been identified in figures 5.2 and 5.3, essentially only two types of flow dominate the spreading dynamics, namely inertia–driven spreading and capillary flow. Front views of the droplet spreading process at different times are shown in figure 5.5 for a selection of scratch widths and depths that lead to each of the seven equilibrium morphologies, while figure 5.6 illustrates how the horizontal and vertical dimensions of the droplet change in time between different morphologies. There, D_{Along} refers to the length of the liquid in the direction of the scratch, D_{Across} is the diameter perpendicular to the scratch, and H is the droplet height measured at the centre of the scratch from the bottom of the scratch to the free surface. These quantities are normalised by the equilibrium spreading diameter of an equivalent droplet on a flat surface, D_{flat} and height H_{flat} of a corresponding droplet after impact on a smooth flat surface, i.e. with no scratch. Note that in most cases considered here $D_{flat} \approx D_{max}$ since the very low receding contact angle prevents contraction of the contact line, but for other values of θ_R

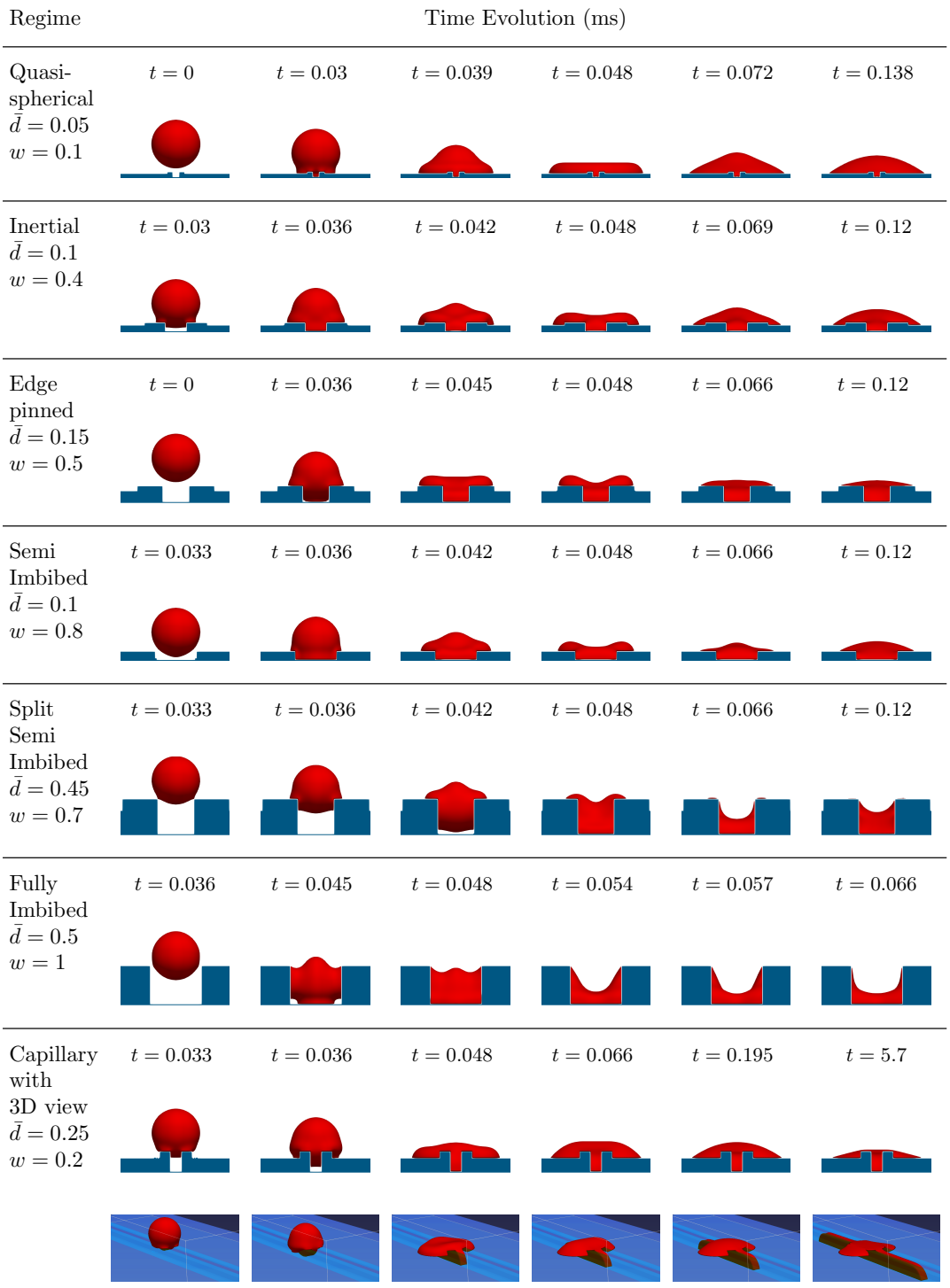

Figure 5.5: Front view snapshots of the different regimes evolving in time measured in milliseconds. The images are to scale, the zoom scale is constant and the droplet diameter (hence also volume) is kept constant. The last row contains 3D views to demonstrate the capillary flow along the scratch.

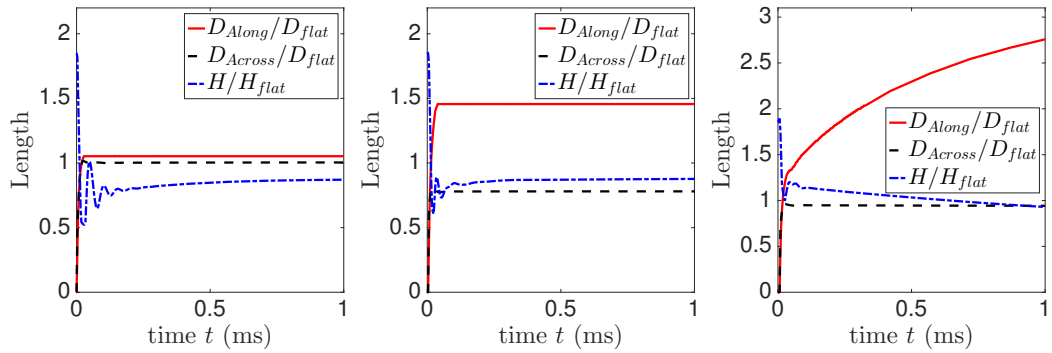

Figure 5.6: Evolution with time of the morphology height and dimensions along and across a scratch for the (a) quasi–spherical cap, (b) edge–pinned, and (c) capillary flow cases shown in figure 5.5.

these values are generally different.

In the quasi–spherical cap regime, the scratch is filled and covered very quickly, the droplet spreads to reach a maximum diameter and then oscillates, as seen in the H curve in figure 5.6(a), before relaxing more slowly to its equilibrium shape. The resulting horizontal dimensions D_{Along} and D_{Across} are similar to the corresponding spherical cap formed on a smooth flat surface. However, the slight extension of the droplet along the scratch results in a lower equilibrium height.

In the inertial regime, the droplet touches the side ridges, then penetrates to the bottom surface of the scratch. The liquid spreads on the side ridges and spills over onto the original substrate surface, as seen in the second row of figure 5.5. Compared to the quasi–spherical cap case, there is greater spreading along the scratch and slightly shorter spreading in the direction perpendicular to the scratch. The wider scratch results in a greater volume of liquid occupying the scratch, and consequently a slightly reduced final droplet height. In the edge–pinned regime, i.e. for wider scratches, the droplet contact line reaches the outer edges of the side ridges, but, as noted in section 5.2.1, there is insufficient momentum to carry the free surface past the edges, and the contact line remains pinned as seen in figure 5.5. Figure 5.6(b), which corresponds to $w = 0.5$, shows the increased inertia–driven spreading along the scratch and the subsequent halting of the contact line producing

a constant D_{Along} as a result of the very low receding contact angle. The extent of the droplet in the direction across the scratch is reduced by the enhanced flow along the direction of the scratch and the pinning on the ridge edges.

Under conditions leading to the semi–imbibed morphology, the droplet impacts the bottom of the scratch and spreads along and across the scratch and then impacts onto the side ridges, see figure 5.5. The droplet spreads on the top of the side ridges but the contact line does not reach the outer edges; it becomes pinned somewhere on the top of the ridges because of the very low receding contact angle. In the split-semi–imbibed regime, the droplet impacts the side ridges first, and then penetrates into the scratch, reaching the bottom and spreading along it. As the droplet spreads into the scratch, it splits along the inner edges of the side ridges, leaving separated droplets sitting on the top of the side ridges. These droplets are almost flat because of the very low receding contact angle. In the fully imbibed regime, the droplet never impacts on the top surface of the side ridges but falls into the scratch and spreads until an equilibrium is reached.

Finally, as shown in the 3D view included in the bottom row of figure 5.5, for scratches producing capillary flow, the droplet initially spills over the side ridges onto the original substrate as in the quasi–spherical cap and inertial regimes. However, the liquid then spreads along the scratch by capillary action until there is no more liquid to supply further flow. This can be clearly seen in the evolution of both D_{Along} and the droplet height in figure 5.6(c). Note the different scale on the vertical axis in this plot compared to the others in figure 5.6.

The rate of capillary propagation has been studied extensively starting with work by Washburn (1921), Bell and Cameron (1906) and Lucas (1918) on cylindrical capillaries. The main finding is that the propagation length x increases as the square root of time, that is $x \propto \sqrt{t}$. More recently this analysis has been extended to other geometries including, capillary flow in open rectangular micro–channels, studied theoretically and experimentally by Yang et al. (2011). They followed a similar

approach to that used to derive the Washburn model except that they applied the procedure to an open rectangular micro–channel. The reservoir droplet in their experiments was large enough relative to the micro–channel to ignore its Laplace pressure in the model. Although the capillary flow seen here initially follows the propagation rate predicted by their model, the limited volume of fluid in the droplet supplying the flow soon results in a more rapid decrease in the speed of propagation and the corresponding flattening of the D_{Along} curve in figure 5.6(c).

5.2.3 Groove Without Ridges

Removing the side ridges from the topography in figure 5.1 reduces the number of possible equilibrium morphologies from seven to five, and alters the combinations of groove width and depth at which the morphologies arise. The corresponding regime map, constructed from simulations for groove widths ranging from 0.1–1 and depths of 0.05–0.75 with increments of 0.1 and 0.05 respectively, is shown in figure 5.7. The morphologies caused by the presence of the ridges, namely edge–pinned and inertial (where the droplet spills over the ridges), are not seen with this topography. These both merge into the semi–imbibed morphology, where the equilibrium shape of the droplet occupies both the groove and the nearby region of the substrate surface, and is the dominant morphology for sufficiently shallow grooves. For narrow and shallow grooves, the morphology can still be classed as a quasi–spherical cap, and for narrow and deep grooves, the capillary morphology is still seen. The fully imbibed, and split semi–imbibed morphologies are again seen for sufficiently wide and deep grooves.

The theoretical estimates (5.1), (5.3) and (5.4) for the boundaries of the regions in the regime map are readily adapted by using the appropriate depth $\bar{d}$, and these are included in figure 5.7. Again, good agreement is seen between these estimates and the results of the simulations.

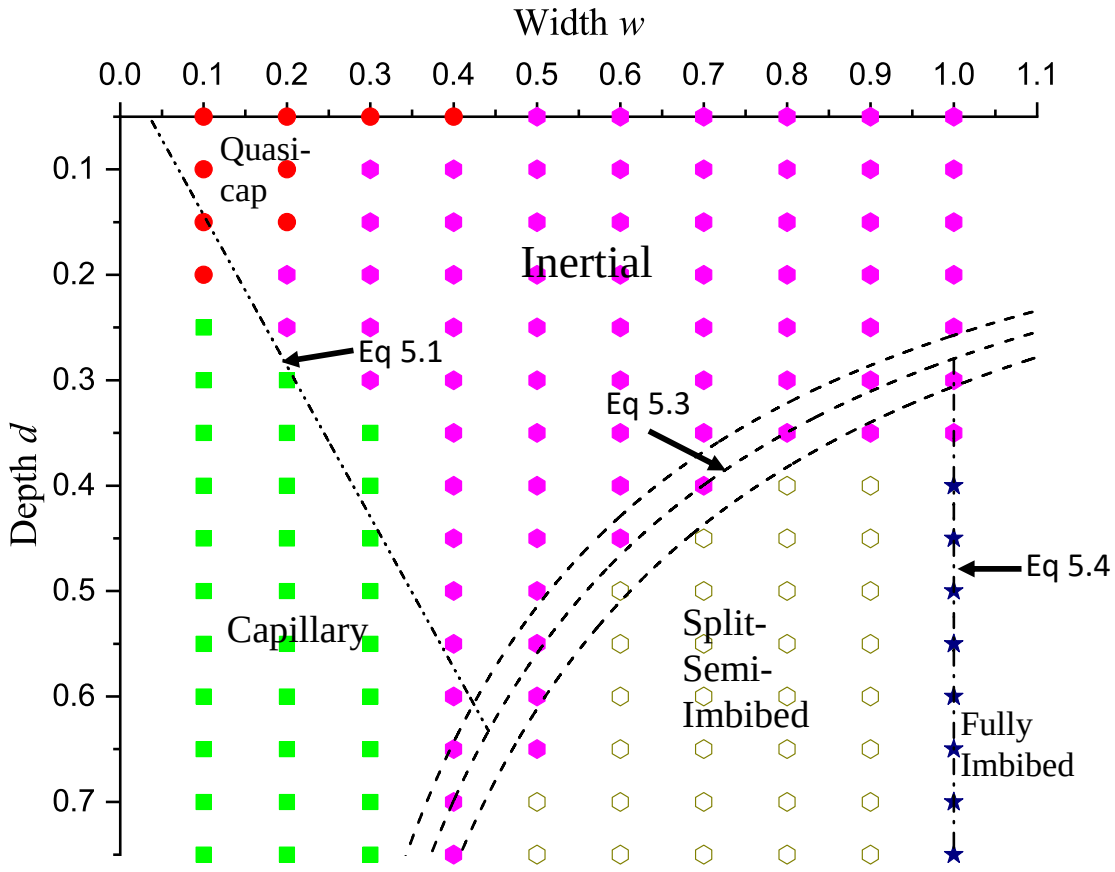

Figure 5.7: Regime map of equilibrium morphologies formed by printing a single droplet centred on a groove of width w and depth d with no side ridges. Simulation parameters: $Re = 204$, $We = 26$, $\theta_A = 75°$, and $\theta_R = 1°$. The overlaid lines and curves are theoretical estimates of the regime boundaries based on conditions (5.1), (5.3) and (5.4).

5.3 Effect of Flow and Substrate Parameters

The regime maps in figures 5.3 and 5.7 were constructed using a single set of material and flow parameters θ_A, θ_R, Re, and We to illustrate the effects of the scratch geometry and the relationships among the morphologies. For this case, the boundaries of the regions within the regime maps are found to be represented very well by the theoretical estimates (5.1)–(5.4) that are more broadly applicable. Apart from the criterion for capillary flow, these expressions are based on the maximum spreading diameter, for which many models exist that account for the effects of Reynolds number, Weber number and advancing contact angle (see table 2.1). Hence it is possible to predict new regime boundary estimates for other values of these parameters.

5.3.1 Effect of Reynolds and Weber Numbers

Increasing Re and/or We promotes greater spreading of the droplet on impact and the droplet is therefore able to spill over wider side ridges. Hence w_{pin} — the critical scratch width for edge pinning in (5.2) — increases and the 'inertial' region of figure 5.3 will expand to the right. This effect is illustrated in the specific case shown in figure 5.8, for a scratch geometry given by $d = 0.15$ and $w = 0.5$. A droplet impact at $Re = 62$ results in a 'semi–imbibed' morphology, whereas an impact on the same scratch at $Re = 102$ produces the 'edge–pinned' morphology, and at $Re = 204$ the 'inertial' morphology arises, consistent with the increase in the value of w_{pin}.

The greater inertia of the droplet will also result in greater penetration into and along the scratch, resulting in a smaller liquid height within the scratch and consequently a greater tendency for the droplet to split along the inner edges of the scratch and leave separate small droplets on the outer surface. From the form of equation (5.3) it is clear that the boundary of the 'split semi-imbibed' region in both figures 5.3 and 5.7 will expand upwards and to the left — i.e. towards narrower,

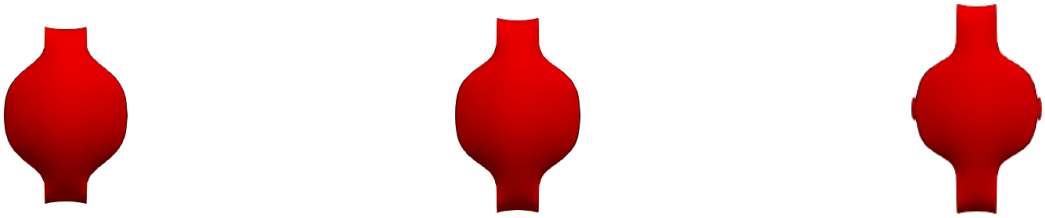

$Re = 62$
'semi-imbibed'

$Re = 102$
'edge-pinned'

$Re = 204$
'inertial'

Figure 5.8: Effect of Re on the morphology resulting from a droplet impact on a scratch of dimensions $d = 0.15$ and $w = 0.5$ at $We = 26$, with $\theta_A = 75°$ and $\theta_R = 1°$.

shallower scratches. The critical condition (5.1) for the onset of capillary flow is independent of Re and We since capillary flow is not inertia–driven and continues long after the initial spreading of the droplet. It is of course greatly influenced by θ_A, and this is discussed below.

5.3.2 Effect of the Advancing Contact Angle, θ_A

The effect of θ_A on the initial spreading of a droplet on a flat surface is captured in some of the models of maximum spreading diameter in table 2.1. It is well known that contact angles below 90° promote spreading and those above hinder it. Hence increasing θ_A results in reduced spreading both along and perpendicular to the scratch, and a consequently increased droplet height (unless of course the droplet is fully imbibed). However, θ_A also influences the shape of the liquid free surface within the scratch, as can be seen in figure 5.9, which shows just the liquid volume with the confining solid made invisible.

The contact line on the bottom of the scratch, which is generally concave at $\theta_A = 75°$, becomes convex when $\theta_A = 115°$ as the side walls of the scratch then act to hinder rather than assist spreading. The non–trivial shape of the liquid free surface in the 'semi–imbibed' and 'split semi–imbibed' cases illustrate why there is

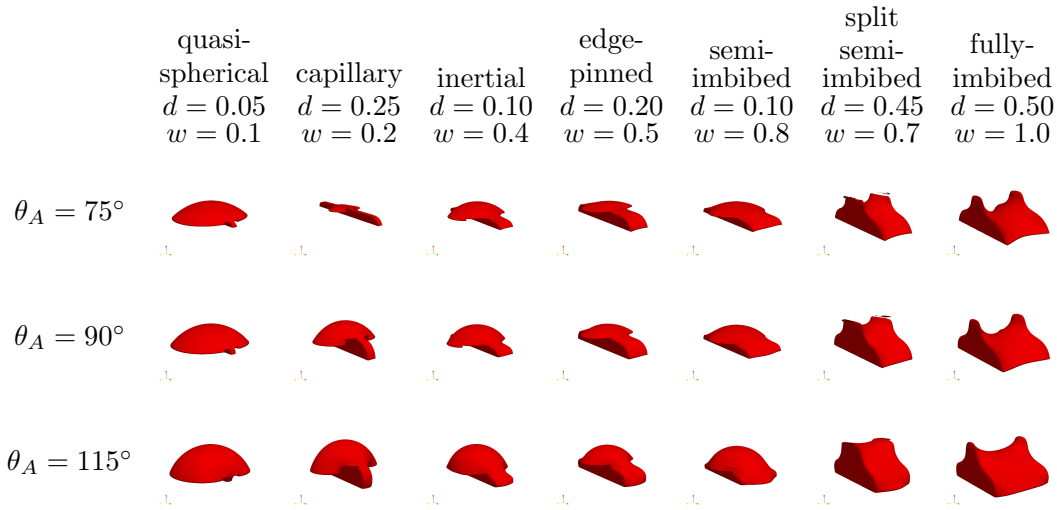

Figure 5.9: Effect of θ_A on final droplet shape for $Re = 204$, $We = 26$ and $\theta_R = 1°$. The images show just the liquid volume(s) within and around each scratch.

a small discrepancy between the predicted regime boundary given by equation (5.3) and that observed from the simulations.

In the 'quasi–spherical cap' regime, the liquid volume that runs along the scratch decreases with increasing θ_A until it no longer extends beyond the diameter perpendicular to the scratch, and for $\theta_A = 115°$ (figure 5.9) the liquid inside the scratch does not extend as far as that above the scratch. Moreover, capillary flow will no longer occur for $\theta_A \geqslant 90°$, and as a consequence the region in figures 5.3 and 5.7 where capillary flow exists moves to smaller values of w/d as θ_A increases, until the capillary flow region vanishes.

For a scratch that produces the 'inertial' morphology when $\theta_A = 75°$, the reduced spreading that occurs when θ_A is increased can mean that the droplet no longer has sufficient momentum to spill over the side ridges, and the droplet becomes 'edge–pinned' or 'semi–imbibed'. A similar effect is seen for wider scratches, and we conclude that the boundaries within the regime map in figure 5.3 shift towards lower widths as θ_A increases, with the capillary flow region eventually disappearing.

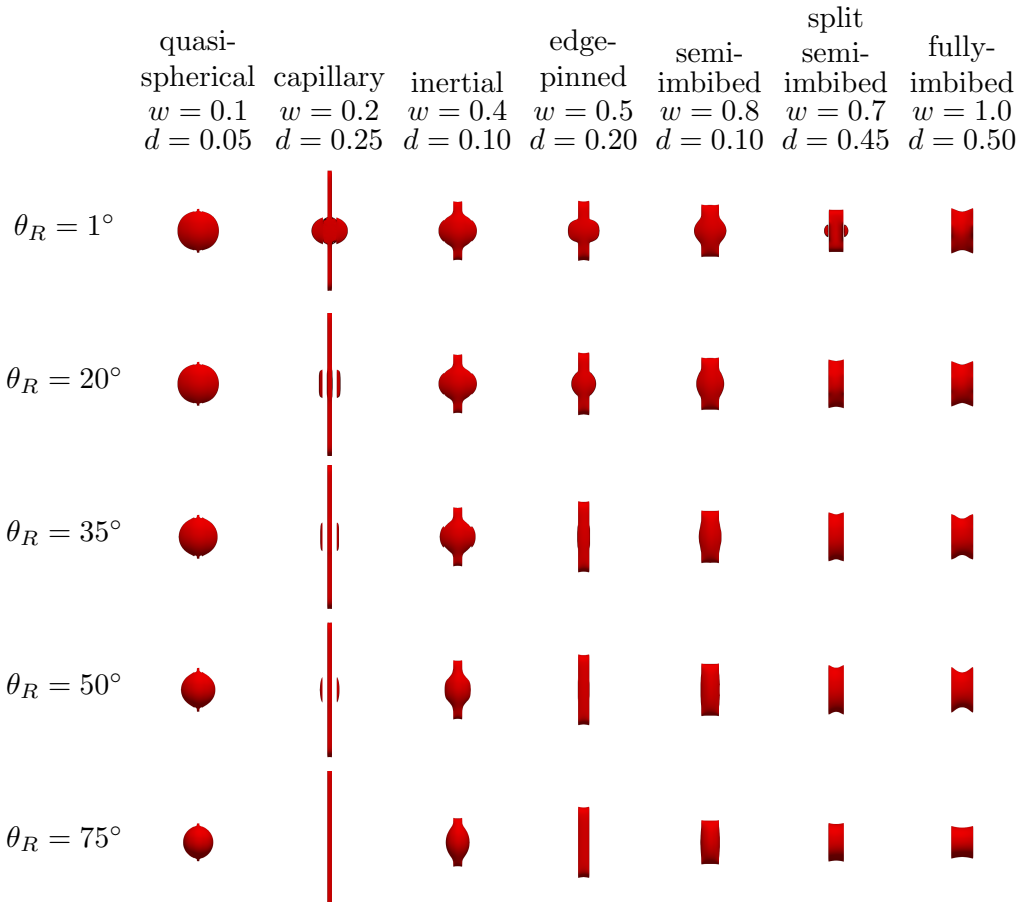

Figure 5.10: Effect of θ_R on final droplet shape. The images show top views for $\theta_A = 75°$, $Re = 204$, and $We = 26$.

5.3.3 Effect of the Receding Contact Angle, θ_R

If, as the droplet shape changes, the contact angle falls below the receding contact angle, the contact line will recede. Changes in θ_R are therefore be expected to have a significant influence on the droplet morphologies discussed above. Figure 5.10 highlights this via top-view plots of the final droplet shape for five different values of θ_R from the 1° value used to create figures 5.3 and 5.7 up to $\theta_R = 75°$, which corresponds to the case where there is no contact angle hysteresis.

For scratch dimensions leading to the quasi–spherical cap morphology, the droplet remains quasi–spherical, but its footprint becomes smaller as θ_R increases because the contact line recedes until an equilibrium is reached where the contact angle is everywhere equal to or greater than θ_R. The conditions for capillary flow

to occur are independent of θ_R, but as θ_R increases, the contraction of the droplet above the scratch means that more liquid is available to feed the capillary flow and the final extent of the capillary flow is therefore increased. However, for intermediate θ_R, as the droplet recedes from the top of the side ridges and original surface, small amounts of liquid are left behind in the corners between the outer wall of the side ridges and the original surface of the substrate. When there is no contact angle hysteresis ($\theta_R = \theta_A = 75°$), the entire droplet is pulled into the scratch by capillary action.

The 'inertial' morphology in figure 5.3 arises when the droplet spills over the side ridges of the scratch onto the original surface, but no capillary action occurs. When θ_R is larger, the contact line recedes after reaching its maximum spread, and climbs back onto the side ridges to reach a different equilibrium. Hence the 'inertial' morphology becomes 'edge–pinned' and 'semi–imbibed' for θ_R values of 50° and 75° respectively. The liquid inside the scratch also recedes with higher θ_R. The 'semi–imbibed' morphology becomes 'fully–imbibed' due to the recession of the footprint outside the groove into it. The 'edge–pinned' morphology turns into a 'semi–imbibed' and then 'fully–imbibed' as θ_R approaches θ_A. The fully imbibed morphology only changes in its extent along the scratch. Increasing the receding contact angle generally results in an equilibrium morphology that is less spread in the direction perpendicular to the scratch, and also shorter in the direction along the scratch. The exceptions are the capillary and edge–pinned regimes, where the lack of contact–line pinning on the upper substrate releases more liquid to penetrate along the scratch. All the regime map boundaries shift to lower widths, except the capillary regime because it is governed by θ_A.

5.4 Summary

In this chapter, the spreading of a single micro–droplet onto a scratched substrate has been investigated. The scratch is idealised into a groove of rectangular cross–section, with rectangular side ridges representing material displaced from the groove. Seven distinct equilibrium morphologies are identified as a result of inertial spreading, contact line pinning on various features of the topography, imbibition of the droplet into the scratch and capillary flow along it. These morphologies arise for distinct ranges of scratch depth and width, relative to the droplet size, which define regions of a regime map. Using existing models for the maximum spreading diameter of a droplet on a flat surface, and accounting for liquid entering the scratch, theoretical estimates of the boundaries within the regime map have been obtained that show good agreement with the numerical predictions. These expressions illustrate how the boundaries can be manipulated by varying the Reynolds number, Weber number, and advancing and receding contact angles.

We discuss the implications of the results found in this chapter from a practical perspective, in the next chapter.

Chapter 6 | Multiple Droplets Impact on Idealised Scratches

Contents

In printing an electrical circuit, a key requirement is continuity of the printed track. Achieving a stable, continuous printed line requires consistent droplet spreading behaviour and a careful balance of droplet generation frequency and printing speed to achieve the correct droplet spacing section 6.1 (Stringer and Derby, 2010). Variations in the droplet spreading caused by a scratch could therefore destabilise the line or cause a break in continuity. Hence quantitative measures of the spreading behaviour on a scratch are potentially useful. Here, for simplicity, the two simplest configurations will be considered, namely printing perpendicular section to a scratch 6.2 and printing along a scratch section 6.3.

6.1 Spacing and Frequency

Before simulating multiple droplets impacting onto a substrate with a scratch on its surface, the spacing between droplet centres $\Delta P = (X_{i+1} - X_i)/D_0$, where X_i is the position of the i^{th} droplet in the direction along the printing direction and D_0 is the in–flight diameter. The period between consecutive droplet impacts $\Delta\tilde{t}$ is measured in units of $\Delta t = 8.0723 \times 10^{-9}$second for the example droplet described in section 4.8.2. We do not consider temperature here. Temperature effects have been studied in Yang et al. (2021). As in the previous sections, we limit our study to the case with contact line pinning.

Before choosing specific ΔP and $\Delta\tilde{t}$, we simulate a range of them with five droplets and tabulate top view images of the results in figure 6.1. Rows are the different spacing between droplet centres and columns are periods. The spacing range considered is $0 - 0.45$, to picture how much overlap this results in, remember that the equilibrium spreading diameter here is $D^*_{flat} \approx 2D_0$. Time steps are reported in figure 6.1 in units of 8.0723×10^{-9}, ranging from 1000–10000.

For $\Delta P = 0$, a spherical cap is formed as expected. As ΔP increases the morphology starts elongating along the access of printing. The sides of the line

start forming a wave–like pattern as ΔP increases. Increasing ΔP further causes individual droplets to form, see $\Delta P = 0.45$. The best line quality is seen for ΔP in the range $0.2 - 0.3$. This is consistent with the results by Thompson et al. (2014), see figure 2.2. converting the δ values from figure 2.2 to Δx, $\delta = 0.81$ reported as spacing for a good quality line by Thompson et al. (2014) corresponds to $\Delta x \approx 3$ for our system which is consistent with our simulations. The period does not have a significant effect on the formed morphologies probably because of contact line pinning.

We, therefore, use $\Delta P = 0.25$ for the rest of this chapter when simulating printing multiple droplets onto a scratch.

6.2 Line Printing Across a Scratch

With the prospect of a break in line continuity, a key quantity to consider is the extent of droplet spreading in the direction perpendicular to the scratch. Figures 6.2a and 6.2b show the behaviour of D_{Across}, i.e. the length of the resulting droplet morphology in the direction perpendicular to the scratch (see figure 5.3 for a figure explaining D_{Across} and D_{Along}), as a function of scratch width and depth. The plots show D_{Across} normalised by D_{flat}, the equilibrium spreading diameter of an equivalent droplet on a flat surface. Recall that the scratch width and depth are scaled by the impacting droplet's in–flight diameter. While narrow, shallow scratches cause only a small change in the extent of spreading, it is clear that as the droplet and scratch become similar in size, a significant shortfall in the spread length occurs. Depending on the degree of overlap between consecutive droplets, which determines the printed line width (Stringer and Derby, 2010), such a reduction in spreading could prevent coalescence of a droplet with the rest of the line and hence a break in continuity. Note that the convergence of the lines in figure 6.2a and the sudden drop in the $w = 0.4$ line in figure 6.2b are a result of pinning of the contact line on

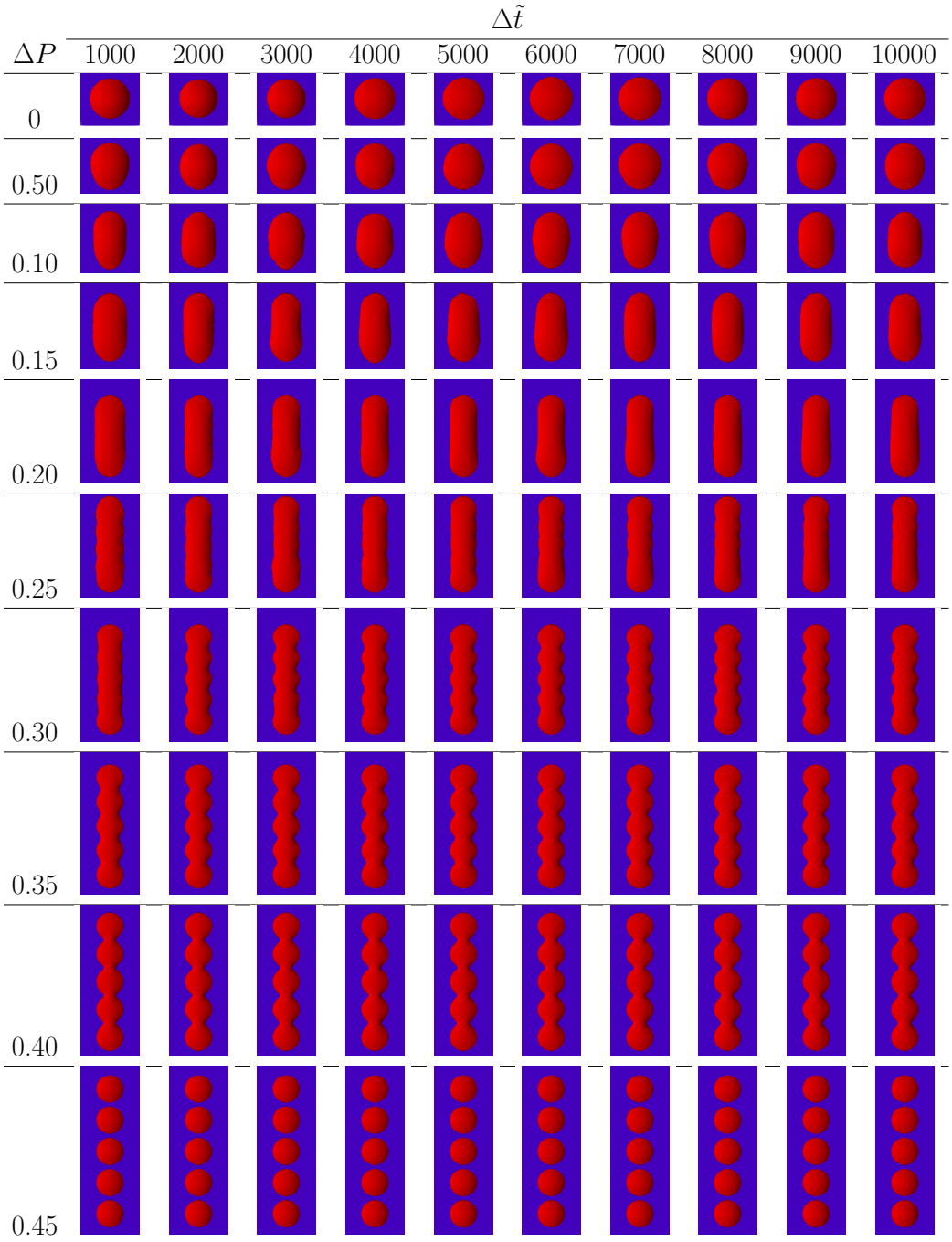

Figure 6.1: A table of morphologies formed by the printing of five droplets at $Re = 204$, $We = 26$, with $\theta_A = 75°$ and $\theta_R = 1°$. Columns represent different periods between droplet impacts in units of $\Delta\tilde{t}$ given in units of $\Delta t = 8.0723 \times 10^{-9}$second

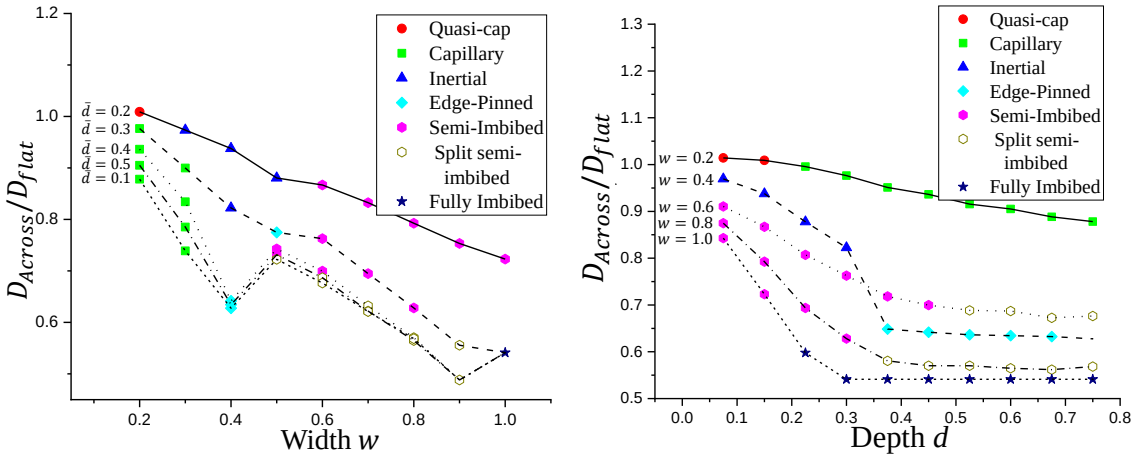

(a) (b)

Figure 6.2: D_{Across}, the length of the final single–droplet morphology in the direction perpendicular to a scratch following deposition of a droplet on the scratch shown in figure 5.1 at $Re = 204$, $We = 26$, with $\theta_A = 75°$ and $\theta_R = 1°$. The plots show variation with scratch width and depth, and the coloured symbols indicate the type of morphology following the same labelling as in figure 5.3.

the outer edge of the side ridges. The upturn between $w = 0.9$ and $w = 1.0$ in figure 6.2a is because for the 'fully–imbibed' morphology, $D_{Across} = w$.

Another mechanism by which line continuity could be broken is through the splitting of the droplet along the inner edge of the scratch. This is illustrated in figure 6.3, which shows simulations of printing a series of five droplets across two scratches with the same depth but different widths. Both scratches appear in the 'split semi–imbibed' region of figure 5.3, and the third droplet, landing on the scratch centre, splits along the inner edges of the scratch, as expected — see figure 6.3(b) and (f). For the wider of the two scratches, this splitting is irrecoverable and the printing continues with a separate line on the other side of the scratch. However, for the slightly narrower scratch, when the fourth droplet is printed, it pushes back on the pre–existing liquid on the substrate, making the liquid coalesce and become continuous again, see figure 6.3(g). This illustrates that the dynamics of the consecutively printed and coalescing droplets can be subtly different from the single–droplet dynamics. Note that while the narrower scratch does not cause a break in continuity, the thinner parts of the printed line could cause problems such as higher resistance or local heat generation.

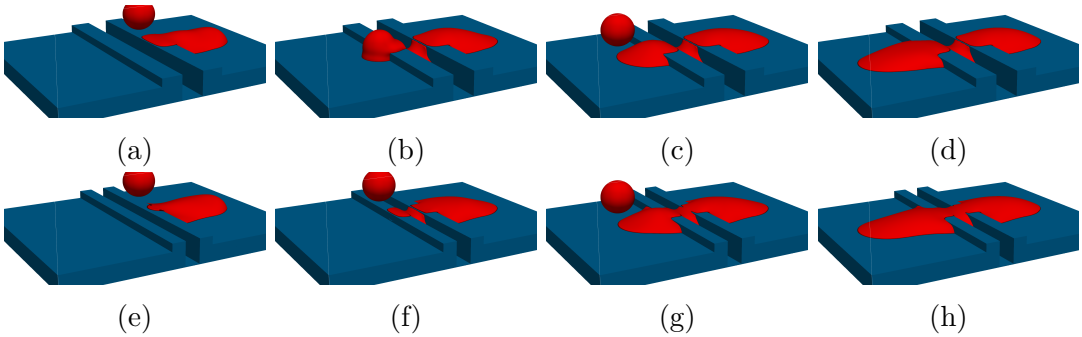

Figure 6.3: Simulations of printing consecutive droplets across scratches of depth $\bar{d} = 0.4$ ($d = 0.6$) and widths $w = 0.6$ (images a–d) and $w = 0.45$ (images e–h).

The extent of liquid spreading along a scratch, D_{Along} (see figure 5.3), is also an important consideration in line printing, and this is captured in figures 6.4a and 6.4b. For a line crossing the scratch, spreading along the scratch would create a variation in the thickness of the line that could potentially lead to instability and formation of bulges along the line. As can be seen in figures 6.4a and 6.4b, all dimensions of scratch lead to enhanced spreading along the scratch direction, with the most significant extent being of course that corresponding to the deep, narrow scratches where capillary flow occurs. The long filaments of the capillary morphology could be problematic if, for instance, two parallel lines are being printed in close proximity for a printed circuit: they could cause the two lines to connect unintentionally, resulting in a short circuit. However, because of the slower time-scale of the capillary flow, as seen in figure 5.6(c), this issue could perhaps be avoided using a fast enough curing mechanism or by creating a larger advancing contact angle. On the other hand, this morphology can be exploited to connect two lines by designing such a feature and using a slowly evaporating ink.

6.3 Printing Along a Scratch

The edge–pinned morphology is an example of how structured substrates can be exploited to print lines with sharp edges. To demonstrate this effect, five droplets are printed into a groove with depths of $\bar{d} = 0.3$ and $\bar{d} = 0.45$ and width $w = 0.4$,

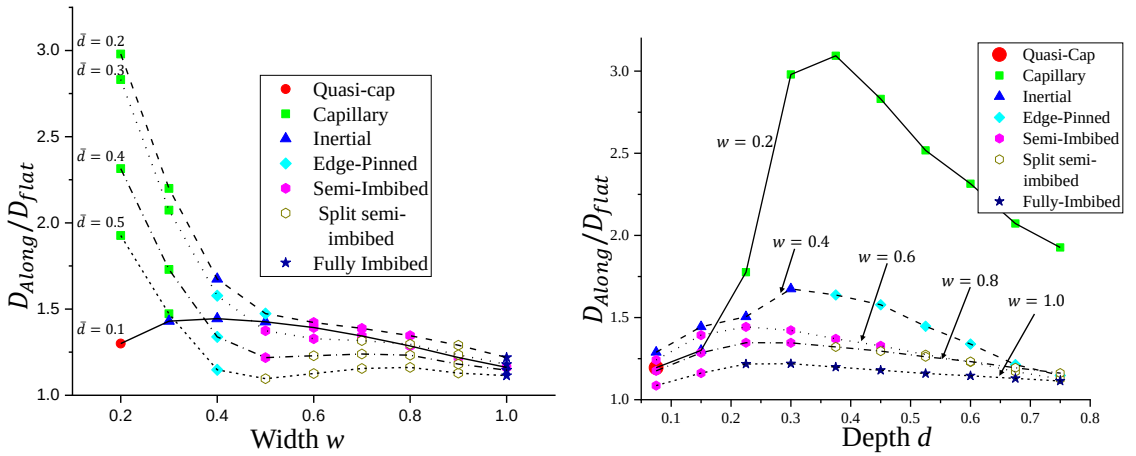

(a) (b)

Figure 6.4: D_{Along}, the length of the final single–droplet morphology in the direction along a scratch following deposition of a droplet on the scratch shown in figure 5.1 at $Re = 204$, $We = 26$, with $\theta_A = 75°$ and $\theta_R = 1°$. The plots show variation with scratch width and depth, and the coloured symbols indicate the type of morphology following the same labelling as in figure 5.3.

both corresponding to the edge-pinned morphology. The results are visualised in figure 6.5. In the first simulation, ($\bar{d} = 0.3$ and $w = 0.4$), although the first droplet forms a sharp edge as expected, subsequent droplets spill over as seen in figure 6.5(c) and (d). This occurs because the precursor droplet inside the groove is in the spreading path of the subsequent droplet; this causes it to spill over. Increasing the depth to 0.45, however, allows more volume for droplet spreading inside the groove, so overspill does not occur and a sharp line is formed along the outer edges of the side ridges, as seen in figure 6.5(h). These two simulations demonstrate how challenging printing a sharp line can be.

The simulations of printing along and across a scratch show that topographical features of commensurate size to droplets have a significant effect not only on a single droplet but also a series of droplets.

Possible implications of the morphologies identified in this work are discussed in table 6.1.

Table 6.1: Implications of the various morphologies.

Morphology	**Implications**
Capillary	This morphology produces the largest D_{Along} due to capillary action. This result in unwanted connections between printed liquid bodies. Due to the relatively slow nature of capillary flow, this can be avoided using a fast–enough sintering mechanism. The capillary morphology can be exploited to transport liquid using micro–structuring of such scratches. It can also be used to intentionally connect two otherwise disconnected printed morphologies.
Quasi–spherical cap and inertial	The distinction between these two morphologies is subjective and application dependent. Here, we have considered a 10% deviation in spreading diameters to be the critical point, this criterion can be different for other applications. Beyond a certain level of shortening, a continuous line might break because the subsequent droplet will not coalesce with the previously printed one. This will occur when the shortening is greater than the overlap between printed droplets. Similarly, if the morphology is lengthened in one dimension to an extent greater than clearance (with an adjacent line, for instance) unwanted coalescence might occur. The quasi–spherical cap morphology can potentially be exploited for centring droplets without significant detriment to the morphology. The inertial morphology can also be exploited to print lemon–shaped morphologies.
(Split) Semi–imbibed	The characteristic feature of semi–imbibed morphologies is that they do not overspill onto the original substrate. When printing droplets across such a scratch, the droplet footprint will not only be shortened like inertial but also elevated on the side ridges above the substrate. This makes it more likely to prevent the coalescence of subsequent droplets and separation will occur along the outer edges of the side ridges in the semi–imbibed case. In the split semi–imbibed case, splitting will also occur along the inner edges of the side ridges such as seen in figure 6.3.

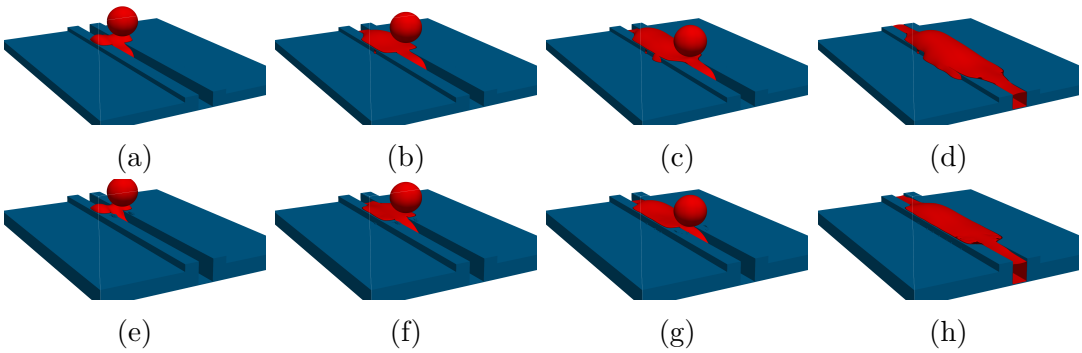

Figure 6.5: Simulations of printing five consecutive droplets along scratches with width $w = 0.4$ and depths $\bar{d} = 0.3$ (images a-d) and $\bar{d} = 0.45$ (images e-h).

Table 6.1 Continued: Implications of the various morphologies.

Morphology	**Implications**
Fully imbibed	Here the entirety of the droplet sinks into the scratch. This most problematic because contact with a subsequent droplet will not be possible. For scratches that are just as wide as the droplet in–flight diameter, the droplet will sink into the scratch but will have contact with the inner walls of the scratch.
Edge–pinned	The distinctive feature of this morphology is the sharp contact line of the morphology that form along the outer edges of the side ridges. Besides the implications of a semi–imbibed morphology discussed above, the edge–pinned morphology can also be exploited to print sharp morphologies as demonstrated in figure 6.5.

6.4 Summary

Printing a continuous lines is sensitive to spacing. A spacing can be chosen to form a continuous line in the flat substrate surface case, but the morphology differs. The interaction of droplets with a scratch of commensurate size can be harmful in different ways. When printing a line of droplets across a scratch, the line can shorten in the direction perpendicular to the scratch will result in droplets separating, resulting in line breaks, see chapter 6. For sufficiently deep and narrow scratches, capillary flow along the scratches could lead to unintentional connections between parallel tracks; in the case of printed electronics this can result in malfunctioning circuits. However, this can be an opportunity to make use of intentional features (such as those described by Nie and Kumacheva (2008), or Seemann et al. (2005)) to control spreading and maintain a uniform printed line. As printing resolutions improve, and droplet sizes decrease, the results show that the consideration of the substrate's topographical features becomes increasingly important in achieving desired printing outcomes.

Chapter 7 | Conclusions

With an estimated market size of $41 billion in 2020, printed electronics combines electronic manufacturing with text/graphics printing techniques to produces thin, flexible, light, cost-effective and/or environmentally–friendly products such as photovoltaics, displays, integrated smart systems and electronic components. Conventional text/graphics printing techniques used in printed electronics include gravure, flexo and screen printing. To move to roll–to–roll, high throughput, and flexible manufacturing, alternative technologies, particularly *inkjet printing*, have been receiving increasing attention.

A few key features qualify inkjet printing as a prime alternative. The method is digital which removes its need for a mask/frame and makes it easy to change the printed pattern on demand. Inkjet printing is non–contact, making it suitable for printing onto unconventional substrates such as flexible, fragile, liquid, and powder substrates. Inkjet printing also minimises waste conventionally lost to masks/frames. The method can also work at speed and in parallel on different parts of the product. Limitations of inkjet printing are the restriction of viscosity, typically $\mu < 20$ mPa s, and particle sizes which need to be small enough to avoid blockages. Substrates have requirements in transparency, *surface smoothness*, thinness and lightness. Small imperfections in the substrate surface, caused by small variations during manufacturing, or as a result of unintended damage such as *scratching* during transportation and/or handling, can affect the printing quality. Substrate surface topographical features can also be added and exploited to control the spreading of liquid. This thesis we studied the interaction of single and multiple droplets with a surface feature/defect of commensurate size to inkjet printing droplets across the relevant parameter space.

The lattice Boltzmann method was applied in this thesis on the basis of a

number of advantages. These include: it is well suited to multiphase simulations, with interface motion, break–up and coalescence readily captured in 3D, multiphase systems do not require a relation between θ_d and U, but just the static contact angle θ_s in the case without contact angle hysteresis (CAH), and the advancing θ_A and receding θ_R contact angles in cases with CAH. LBM is also localised and lends its self for parallel computing in GPUs (Krüger et al., 2016); we make use of this feature to run an extensive parametric study here. Shortcommings in the common LB approach were addressed by modifications suggested in the literature particularly thos by Shan and Chen (1993), Sbragaglia et al. (2007), and Li et al. (2012; 2013; 2019). A geometric model was applied to capture wetting rather than the commonly used fixed–density approach.

The simulation method was validated with literature–reported experimental data of droplet impact onto a surface. We also use analytical predictin of maximum and equilibrium spreading diameters for validation. The parallel nature of LBM to accelerate it using CUDA is exploited to accelerate the simullation by up to two orders of magnitude on a GPU compared to a CPU. This validated and accelerated methodology is then used to simulate micro–droplet impact onto a substrate surface with a scratch.

The scratch is idealised into a groove of rectangular cross–section, with rectangular side ridges representing material displaced from the groove. Seven distinct equilibrium morphologies are identified as a result of inertial spreading, contact line pinning on various features of the topography, imbibition of the droplet into the scratch and capillary flow along it. These morphologies arise for distinct ranges of scratch depth and width, relative to the droplet size, which define regions of a regime map. Using existing models for the maximum spreading diameter of a droplet on a flat surface, and accounting for liquid entering the scratch, theoretical estimates of the boundaries within the regime map have been obtained that show good agreement with the numerical predictions. These expressions illustrate how the boundaries can

be manipulated by varying the Reynolds number, Weber number, and advancing and receding contact angles, see chapter 5.

The scratch is idealised into a groove of rectangular cross–section, with rectangular side ridges representing material displaced from the groove. An extensive parametric study varying the depth and width of the surface feature revealed seven distinct equilibrium morphologies when a single droplet impacts centrally on the topography. These are identified in a regime map as: (i) a 'quasi–spherical cap' that forms when the scratch is too narrow and shallow to cause significant deviation from a spherical cap; (ii) 'inertial', where the droplet spills over the side ridges and also spreads along the scratch, driven by the droplet's inertia; (iii) 'capillary', where a long filament is formed along deep, narrow scratches due to capillary action but the droplet also spills over onto the original substrate; (iv) 'edge–pinned', where the droplet has sufficient energy to spread as far as the outer edge of the side ridges, but not to spill over, resulting in the contact line being pinned at the outer edges of the side ridges; (v) 'semi–imbibed', where most of the droplet rests in the scratch but some of it lies on the outer surface; (vi) 'split–semi–imbibed', where the droplet splits along the inner edges of the scratch to create separated liquid bodies; and (vii) 'fully–imbibed', where the scratch is sufficiently wide and deep that the entire droplet sinks into the scratch. In all these morphologies the droplet spreads due to the inertia of the impact. The contact line becomes pinned because of the low receding contact angle (typical of such printing applications) and the liquid body then relaxes to an equilibrium. In narrow and deep scratches, subsequent capillary flow occurs which forms the long filament. Therefore, there are two main mechanisms to deform the morphology from a spherical cap: a width–dominated mechanism of capillary flow and a cross–sectional area–dominated mechanism where the droplet imbibes into the scratch.

The advancing and receding contact angles, Weber number, and Reynolds number affect the boundaries within the regime map — i.e. the scratch dimensions

for which the different morphologies arise. Increasing the Reynolds number generally shifts the boundaries in the regime map towards larger scratch widths. For example, a droplet that becomes pinned on the side ridge edges at low Reynolds number will be able to spill over them at sufficiently higher Reynolds number; the edge–pinned morphology will then occur at larger widths. For narrow and shallow scratches, however, the greater spreading possible at larger Re does result in greater deviation from a spherical cap, and the quasi–spherical cap morphology, therefore, becomes more restricted to small scratch widths. Decreasing the Weber number has a similar effect to increasing the Reynolds number. Increasing the receding contact angle promotes contraction of the droplet in all directions, in most cases resulting in a less–spread equilibrium morphology. However, in the edge–pinned and capillary regimes, the contraction of the contact line on the upper surfaces of the substrate releases more liquid to penetrate into the scratch, resulting in greater spreading along the scratch. For sufficiently large receding contact angle, the entire droplet can be drawn into a narrow scratch by capillary action. Removing the side ridges reduces the number of different morphologies from seven to five, since the edge–pinned and inertial morphologies related to the ridges are no longer possible; they both become semi–imbibed.

From a practical perspective, the interaction of droplets with a scratch of similar size can be detrimental in different ways. When inkjet printing an electrical track across a scratch, for example, the shortening of the spreading in the direction perpendicular to the scratch can result in a disastrous break in the continuity of the track, as subsequent droplets may not be able to coalesce with the previously deposited liquid, or the liquid might split along an edge of the scratch. The simulations of sequential droplet deposition presented here show that, in some cases, it is possible to recover from a break along an edge if the next droplet can push separated liquid back sufficiently towards the printed track. Another problem might arise for sufficiently deep, narrow scratches, where capillary flow can lead to spreading along the scratch of more than three times the in–flight droplet diameter. If two paral-

lel tracks are being printed, this could lead to unintentional connections, i.e. short circuits between the two tracks.

On the other hand, scratch–like surface features could potentially be exploited to control spreading and maintain a uniform track, if droplets are printed along the feature. Multiple–droplet simulations illustrate how the feature dimensions can be tuned to prevent overspill and form a uniform printed track.

Bibliography

Al–Ghaithi, K.H.A., Harlen, O.G., Kapur, N., and Wilson, M.C.T., 2021. Morphologies and dynamics of micro-droplet impact onto an idealised scratch. *Journal of Fluid Mechanics Accepted*.

Bell, J.M. and Cameron, F.K., 1906. The flow of liquids through capillary spaces. *The Journal of Physical Chemistry*, **10**(8), pp.658–674.

Bennett, T. and Poulikakos, D., 1993. Splat-quench solidification: estimating the maximum spreading of a droplet impacting a solid surface. *Journal of Materials Science*, **28**, pp.963–970.

Bhatnagar, P.L., Gross, E.P., and Krook, M., 1954. A model for collision processes in gases. I. Small amplitude processes in charged and neutral one-component systems. *Physical Review*, **94**(3), pp.511–525.

Brostow, W., Deborde, J.-L., Jaklewicz, M., and Olszynski, P., 2004. Tribology with emphasis on polymers: friction, scratch and wear resistance. *Journal of Materials Education*, **24**(4-6), pp.119–132.

Bussmann, M., Mostaghimi, J., and Chandra, S., 1999. On a three-dimensional volume tracking model of droplet impact. *Physics of Fluids*, **11**(6), pp.1406–1417.

Castrejón-Pita, J.R., Betton, E.S., Kubiak, K.J., Wilson, M.C.T., and Hutchings, I.M., 2011. The dynamics of the impact and coalescence of droplets on a solid surface. *Biomicrofluidics*, **5**(1), p.014112.

Castrejón-Pita, J.R., Kubiak, K.J., Castrejón-Pita, A.A., Wilson, M.C.T., and Hutchings, I.M., 2013. Mixing and internal dynamics of droplets impacting and coalescing on a solid surface. *Physical Review E*, **88**(2), p.023023.

Chandra, S. and Avedisian, C.T., 1991. On the collision of a droplet with a solid surface. *Proceedings of the Royal Society A: Mathematical, Physical and Engineering Sciences*, **432**(1884), pp.13–41.

Chang, J., Ge, T., and Sanchez-Sinencio, E., 1965. Challenges of printed electronics on flexible substrates. In: J.M.A. Lenihan and S.J. Thompson, eds. *2012 IEEE 55th International Midwest Symposium on Circuits and Systems (MWSCAS)* [Online], August 5–8, 2012, Boise. Idaho: IEEE, pp.582–585. Available from: https://ieeexplore.ieee.org/document/6292087 [Accessed October 12, 2019].

Chapman, S. and Cowling, T.G., 1952. *The mathematical theory of non-uniform gases. an account of the kinetic theory of viscosity, thermal conduction, and diffusion in gases*. 2nd ed. Cambridge: Cambridge University Press.

Chen, Z., Wu, L.Y., Chwa, E., and Tham, O., 2008. Scratch resistance of brittle thin films on compliant substrates. *Materials Science and Engineering A*, **493**(1-2), pp.292–298.

Chilton, N., 2012. Printed circuit board fabrication. In: I.M. Hutchings and G.D. Martin, eds. *Inkjet technology for digital fabrication*. Chichester, UK: John Wiley & Sons, Ltd, pp.183–206.

Clanet, C., Beguin, C., Richard, D., and Quere, D., 2004. Maximal deformation of an impacting drop. *Journal of Fluid Mechanics*, **517**, pp.199–208.

Connington, K. and Lee, T., 2013. Lattice Boltzmann simulations of forced wetting transitions of drops on superhydrophobic surfaces. *Journal of Computational Physics*, **250**, pp.601–615.

D'Humières, D., Ginzburg, I., Krafczyk, M., Lallemand, P., and Luo, L.S., 2002. Multiple-relaxation-time lattice Boltzmann models in three dimensions. *Philosophical Transactions of the Royal Society A: Mathematical, Physical and Engineering Sciences*, **360**(1792), pp.437–451.

Dalili, A., Chandra, S., Mostaghimi, J., Fan, H.C., and Simmer, J., 2014. Formation of liquid sheets by deposition of droplets on a surface. *Journal of Colloid and Interface Science*, **418**, pp.292–299.

Das, R., He, X., and Ghaffarzadeh, K., 2019. *Flexible, printed and organic electronics 2020-2030: forecasts, players & opportunities*. (PGI-93/WS/22). Paris: IDTechEx Research.

Dasari, A., Yu, Z.Z., and Mai, Y.W., 2009. Fundamental aspects and recent progress on wear/scratch damage in polymer nanocomposites. *Materials Science and Engineering: R: Reports*, **63**(2), pp.31–80.

Davis, S.H., 1980. Moving contact lines and rivulet instabilities. part 1: the static rivulet. *Journal of Fluid Mechanics*, **98**(2), pp.225–242.

De Jong, R., Enriquez, O.R., and Van der Meer, D., 2015. Exploring droplet impact near a millimetre-sized hole: compared a closed pit with an open-ended pore. *Journal of Fluid Mechanics*, **772**, pp.427–444.

Di Ilio, G., Chiappini, D., Ubertini, S., Bella, G., and Succi, S., 2017. Hybrid lattice Boltzmann method on overlapping grids. *Physical Review E*, **95**(1), p.013309.

Ding, H. and Spelt, P.D.M., 2007. Wetting condition in diffuse interface simulations of contact line motion. *Physical Review E*, **75**(4), p.046708.

Dong, H., Carr, W.W., Bucknall, D.G., and Morris, J.F., 2007. Temporally-resolved inkjet drop impaction on surfaces. *AIChE Journal*, **53**(10), pp.2606–2617.

Duineveld, P.C., 2003. The stability of ink-jet printed lines of liquid with zero receding contact angle on a homogeneous substrat. *Journal of Fluid Mechanics*, **477**, pp.175–200.

Eggers, J., Fontelos, M.A., Josserand, C., and Zaleski, S., 2010. Drop dynamics after impact on a solid wall: theory and simulations. *Physics of Fluids*, **22**(6), p.062101.

Feng, J.Q., 2015. Sessile drop deformations under an impinging jet. *Theoretical and computational fluid dynamics*, **29**(4), pp.277–290.

Furlani, E.P., 2015. Fluid mechanics for inkjet printing. In: S.D. Hoath, ed. *Fundamentals of inkjet printing*. Weinheim, Germany: Wiley-VCH Verlag GmbH & Co. KGaA. Chap. 2, pp.13–56.

Gau, H., Herminghaus, S., Lenz, P., and Lipowsky, R., 1999. Liquid morphologies on structured surfaces: from microchannels to microchips. *Science*, **283**(5398), pp.46–49.

Geier, M. and Schönherr, M., 2017. Esoteric twist: an efficient in-place streaming algorithms for the lattice Boltzmann method on massively parallel hardware. *Computation*, **5**(2), p.19.

Gong, S. and Cheng, P., 2012. Numerical investigation of droplet motion and coalescence by an improved lattice Boltzmann model for phase transitions and multiphase flows. *Computers and Fluids*, **53**(1), pp.93–104.

Guo, W., Jin, C., and Li, J., 2008. High performance lattice Boltzmann algorithms for fluid flows. *2008 International Symposium on Information Science and Engineering, ISISE 2008* [Online], December 20–22, 2008, Shanghai. Vol. 1. New York: IEEE, pp.33–37. Available from: http://ieeexplore.ieee.org/document/4732164/ [Accessed October 19, 2018].

Guo, Z., Zheng, C., and Shi, B., 2002. Discrete lattice effects on the forcing term in the lattice Boltzmann method. *Physical Review E*, **65**(4), p.046308.

He, X., Chen, S., and Zhang, R., 1999. A lattice Boltzmann scheme for incompressible multiphase flow and its application in simulation of rayleigh–taylor instability. *Journal of Computational Physics*, **152**(2), pp.642–663.

He, X. and Doolen, G.D., 2002. Thermodynamic foundations of kinetic theory and lattice Boltzmann models for multiphase flows. *Journal of Statistical Physics*, **107**, pp.309–328.

Hu, J., Jia, R., Wan, K.-t., and Xiong, X., 2014. Simulation of droplet impingement on a solid surface by the level set method. *Proceedings of the 2014 COMSOL Conference in Boston* [Online], October 8–10, 2014, Boston. Cambridge: Comsol, pp.8–10. Available from: https://uk.comsol.com/paper/simulation-of-droplet-impingement-on-a-solid-surface-by-the-level-set-method-18697 [Accessed March 10, 2017].

Huang, H., Sukop, M., and Lu, X., 2015. *Multiphase lattice Boltzmann methods: theory and application*. Chichester, UK: John Wiley & Sons.

Huang, H., Krafczyk, M., and Lu, X., 2011. Forcing term in single-phase and shan-chen-type multiphase lattice Boltzmann models. *Physical Review E*, **84**(4), p.046710.

Huchings, I.M., Martin, G.D., and Hoath, S.D., 2016. Introductory remarks. In: S.D. Hoath, ed. *Fundamentals of inkjet printing*. Weinheim, Germany: Wiley-VCH, pp.1–12.

Hutchings, I.M. and Martin, G.D., 2012. *Inkjet technology for digital fabrication*. Chichester, UK: John Wiley & Sons, Ltd.

Jackson, F.F., Kubiak, K.J., Wilson, M.C.T., Molinari, M., and Stetsyuk, V., 2019. Droplet misalignment limit for inkjet printing into cavities on textured surfaces. *Langmuir*, **35** (29), pp.9564–9571.

Josserand, C. and Thoroddsen, S., 2016. Drop impact on a solid surface. *Annual Review of Fluid Mechanics*, **48**(1), pp.365–391.

Kant, P., Hazel, A.L., Dowling, M., Thompson, A.B., and Juel, A., 2017. Controlling droplet spreading with topography. *Physical Review Fluids*, **2** (9), p.094002.

Khatir, Z., Kubiak, K.J., Jimack, P.K., and Mathia, T.G., 2016. Dropwise condensation heat transfer process optimisation on superhydrophobic surfaces using a multi-disciplinary approach. *Applied Thermal Engineering*, **106**, pp.1337–1344.

Khojasteh, D., Kazerooni, M., Salarian, S., and Kamali, R., 2016. Droplet impact on superhydrophobic surfaces: a review of recent developments. *Journal of Industrial and Engineering Chemistry*, **42**, pp.1–14.

Krüger, T., Kuzmin, A., Kusumaatmaja, H., Shardt, O., Silva, G., and Viggen, E.M., 2016. *The Lattice Boltzmann Method: principles and practice*. AG Switzerland: Springer International Publishing.

Kupershtokh, A.L., Medvedev, D.A., and Karpov, D.I., 2009. On equations of state in a lattice Boltzmann method. *Computers and Mathematics with Applications*, **58**(5), pp.965–974.

Kwon, J.-S., Lee, D.J., and Oh, J.H., 2018. Formation and characterization of inkjet-printed nanosilver lines on plasma-treated glass substrates. *Applied Sciences*, **8**(2), p.280.

Laan, N., De Bruin, K.G., Bartolo, D., Josserand, C., and Bonn, D., 2014. Maximum diameter of impacting liquid droplets. *Physical Review Applied*, **2**(4), p.044018.

Lee, J.B., Laan, N., De Bruin, K.G., Skantzaris, G., Shahidzadeh, N., Derome, D., Carmeliet, J., and Bonn, D., 2016. Universal rescaling of drop impact on smooth and rough surfaces. *Journal of Fluid Mechanics*, **786**, R4.

Li, Q., Du, D.H., Fei, L.L., and Luo, K.H., 2019. Three-dimensional non-orthogonal MRT pseudopotential lattice Boltzmann model for multiphase flows. *Computers & Fluids*, **186**, pp.128–140.

Li, Q., Luo, K.H., Kang, Q.J., He, Y.L., Chen, Q., and Liu, Q., 2016. Lattice Boltzmann methods for multiphase flow and phase-change heat transfer. *Progress in Energy and Combustion Science*, **52**, pp.62–105.

Li, Q., Luo, K.H., Kang, Q.J., and Chen, Q., 2014. Contact angles in the pseudopotential lattice Boltzmann modeling of wetting. *Physical Review E*, **90**(5), p.53301.

Li, Q., Luo, K.H., and Li, X.J., 2012. Forcing scheme in pseudopotential lattice Boltzmann model for multiphase flows. *Physical Review E*, **86**(1), pp.1–9.

Li, Q., Luo, K.H., and Li, X.J., 2013. Lattice Boltzmann modeling of multiphase flows at large density ratio with an improved pseudopotential model. *Physical Review E*, **87**(5), p.053301.

Lim, T., Han, S., Chung, J., Chung, J.T., Ko, S., and Grigoropoulos, C.P., 2009. Experimental study on spreading and evaporation of inkjet printed pico-liter droplet on a heated substrate. *International Journal of Heat and Mass Transfer*, **52**(1-2), pp.431–441.

Lucas, R., 1918. Ueber das zeitgesetz des kapillaren aufstiegs von flüssigkeiten. *Colloid & Polymer Science*, **23**(1), pp.15–22.

Lupo, D., Clemens, W., Breitung, S., and Hecker, K., 2013. Oe-a roadmap for organic and printed electronics. In: E. Cantatore, ed. *Applications of organic and printed electronics*. New York: Springer Science & Business Media, pp.1–26.

Madejski, J., 1976. Solidification of droplets on a cold surface. *International Journal of Heat and Mass Transfer*, **19**(9), pp.1009–1013.

Mirjalili, B.S., Jain, S.S., and Dodd, M.S., 2017. Interface-capturing methods for two-phase flows : an overview and recent developments. *Center for Turbulence Research: Annual Research Briefs*, **2017**(1), pp.117–135.

Mohamad, A.A., 2019. *Lattice Boltzmann method*. 2nd ed. London: Springer-Verlag London Ltd.

Nie, Z. and Kumacheva, E., 2008. Patterning surfaces with functional polymers. *Nature Materials*, **7**(4), pp.277–290.

Pasandideh-Fard, M., Qiao, Y.M., Chandra, S., and Mostaghimi, J., 1996. Capillary effects during droplet impact on a solid surface. *Physics of Fluids*, **8**(3), pp.650–659.

Phelan, F.R., Dunkers, J.P., Zimba, C.G., Flynn, K.M., Parnas, R.S., Peterson, R.C., Li, X., and Fujimoto, J.G., 1999. Numerical prediction of permeability using a lattice Boltzmann method and optical coherence tomography. *International conference on automated composites* [Online], July 5–9, 1999, Paris. Maryland: National Institute of Standards and Technology. Available from: https://tsapps.nist.gov/publication/get_pdf.cfm?pub_id=851633 [Accessed February 19, 2019].

Rashidian, H., Sellier, M., and Mandin, P., 2019. Dynamic wetting of an occlusion after droplet impact. *International Journal of Multiphase Flow*, **111**, pp.264–271.

Rayleigh, L., 1879. On the capillary phenomena of jets. *Proceedings of the Royal Society of London*, **29**(196-199), pp.71–97.

Rioboo, R., Marengo, M., and Tropea, C., 2002. Time evolution of liquid drop impact onto solid, dry surfaces. *Experiments in Fluids*, **33**(1), pp.112–124.

Roisman, I.V., 2009. Inertia dominated drop collisions II: an analytical solution of the Navier–Stokes equations for a spreading viscous film. *Physics of Fluids*, **21**(5), p.052104.

Rothman, D.H. and Keller, J.M., 1988. Immiscible cellular-automaton fluids. *Journal of Statistical Physics*, **52**(3), pp.1119–1127.

Sbragaglia, M., Benzi, R., Biferale, L., Succi, S., Sugiyama, K., and Toschi, F., 2007. Generalized lattice Boltzmann method with multirange pseudopotential. *Physical Review E*, **75**(2), p.026702.

Scheller, B.L. and Bousfield, D.W., 1995. Newtonian drop impact with a solid surface. *AIChE Journal*, **41**(6), pp.1357–1367.

Schiaffino, S. and Sonin, A.A., 1997. Molten droplet deposition and solidification at low weber numbers. *Physics of Fluids*, **9**(11), pp.3172–3187.

Seemann, R., Brinkmann, M., Kramer, E.J., Lange, F.F., and Lipowsky, R., 2005. Wetting morphologies at microstructured surfaces. *Proceedings of the National Academy of Sciences*, **102**(6), pp.1848–1852.

Shan, X. and Chen, H., 1993. Lattice Boltzmann model for simulating flows with multiphases and components. *Physical Review E*, **47**(3), pp.1815–1819.

Shan, X. and Chen, H., 1994. Simulation of nonideal gases and liquid-gas phase transitions by the lattice Boltzmann equation. *Physical Review E*, **49**(4), pp.2941–2948.

Shikhmurzaev, Y.D., 2007. *Capillary flows with forming interfaces*. New York, NY: Taylor & Francis Group, LLC, pp.1–478.

Soltman, D.B., 2011. *Understanding inkjet printed pattern generation*. PhD thesis. University of California at Berkeley, pp.1–97.

Soltman, D.B. and Subramanian, V., 2008. Inkjet-printed line morphologies and temperature control of the coffee ring effect. *Langmuir*, **24**(5), pp.2224–2231.

Spaid, M.A.A. and Phelan, F.R., 1997. Lattice Boltzmann methods for modeling microscale flow in fibrous porous media. *Physics of Fluids*, **9**, pp.2468–2474.

Stringer, J. and Derby, B., 2010. Formation and stability of lines produced by inkjet printing. *Langmuir*, **26**(12), pp.10365–10372.

Stringer, J. and Derby, B., 2012. When the drop hits the substrate. In: I.M. Hutchings and G.D. Martin, eds. *Inkjet technology for digital fabrication*. Chichester, UK: John Wiley & Sons, Ltd. Chap. 5, pp.113–139.

Succi, S., Foti, E., and Higuera, F., 1989. Three-dimensional flows in complex geometries with the lattice Boltzmann method. *Europhysics Letters (EPL)*, **10**(5), pp.433–438.

Succi, S., 2018. *The lattice Boltzmann equation: for complex states of flowing matter*. Oxford: Oxford University Press, pp.1–762.

Suganuma, K., 2014. *Introduction to printed electronics*. New York: Springer Science & Business Media.

Sukop, M.C. and Thorne, D.T., 2006. *Lattice Boltzmann modeling*. Verlag Berlin Heidelberg: Springer.

Swift, M.R., Osborn, W.R., and Yeomans, J.M., 1995. Lattice Boltzmann simulation of nonideal fluids. *Physical Review Letters*, **75**(5), pp.830–833.

Sykes, T.C., Harbottle, D., Khatir, Z., Thompson, H.M., and Wilson, M.C., 2020. Substrate wettability influences internal jet formation and mixing during droplet coalescence. *Langmuir*, **36**(32), pp.9596–9607.

Thompson, A.B., Tipton, C.R., Juel, A., Hazel, A.L., and Dowling, M., 2014. Sequential deposition of overlapping droplets to form a liquid line. *Journal of Fluid Mechanics*, **761**, pp.261–281.

Van Dam, D.B. and Le Clerc, C., 2004. Experimental study of the impact of an ink-jet printed droplet on a solid substrate. *Physics of Fluids*, **16**(9), pp.3403–3414.

Visser, C.W., Tagawa, Y., Sun, C., and Lohse, D., 2012. Microdroplet impact at very high velocity. *Soft matter*, **8** (41), pp.10732–10737.

Vrancken, R.J., Kusumaatmaja, H., Hermans, K., Prenen, A.M., Pierre-Louis, O., Bastiaansen, C.W., and Broer, D.J., 2010. Fully reversible transition from Wenzel to Cassie–Baxter states on corrugated superhydrophobic surfaces. *Langmuir*, **26**(5), pp.3335–3341.

Wang, Y. and Bourouiba, L., 2018. Non-isolated drop impact on surfaces. *Journal of Fluid Mechanics*, **835**, pp.24–44.

Washburn, E.W., 1921. The dynamics of capillary flow. *Physical Review*, **17**(3), pp.273–283.

Welander, P., 1954. On the temperature jump in a rarefied gas. *Arkiv for Fysik*, **7**, p.507.

Wildeman, S., Visser, C.W., Sun, C., and Lohse, D., 2016. On the spreading of impacting drops. *Journal of Fluid Mechanics*, **805**, pp.636–655.

Wilson, M.C.T. and Kubiak, K.J., 2016. Simulation of drops on surfaces. In: S.D. Hoath, ed. *Fundamentals of inkjet printing*. Weinheim, Germany: Wiley-VCH. Chap. 11, pp.281–312.

Yang, D., Krasowska, M., Priest, C., Popescu, M.N., and Ralston, J., 2011. Dynamics of capillary-driven flow in open microchannels. *The Journal of Physical Chemistry C*, **115**(38), pp.18761–18769.

Yang, J., Zheng, F., and Derby, B., 2021. Stability of lines with zero receding contact angle produced by inkjet printing at small drop volume. *Langmuir*, **37**(1), pp.26–34.

Yarin, A., 2006. Drop impact dynamics: splashing, spreading, receding, bouncing ... *Annual Review of Fluid Mechanics*, **38**(1), pp.159–192.

Yokoi, K., Vadillo, D., Hinch, J., and Hutchings, I., 2009. Numerical studies of the influence of the dynamic contact angle on a droplet impacting on a dry surface. *Physics of Fluids*, **21**(7), p.072102.

Yuan, P. and Schaefer, L., 2006. Equations of state in a lattice Boltzmann model. *Physics of Fluids*, **18**(4), p.042101.

Yuan, W.Z. and Zhang, L.Z., 2017. Lattice Boltzmann simulation of droplets impacting on superhydrophobic surfaces with randomly distributed rough structures. *Langmuir*, **33**(3), pp.820–829.

Zhang, L., Cheng, X., Ku, T., Song, Y., and Zhang, D., 2018. Lattice Boltzmann study of successive droplets impingement on the non-ideal recessed microchannel for high-resolution features. *International Journal of Heat and Mass Transfer*, **120**, pp.1085–1100.

Zheng, F., Derby, B., and Wong, J., 2021. Fabrication of microvascular constructs using high resolution electrohydrodynamic inkjet printing. *Biofabrication*, **13**(3), p.035006.